Development of cubesat thrusters

Dimitrios Tsifakis

A thesis submitted for the degree of
Doctor of Philosophy
at the Australian National University

May 2022

Declaration

This thesis is an account of research undertaken between February 2018 and July 2021 at the Research School of Physics, The Australian National University, Canberra, Australia.

Except where acknowledged in the customary manner, the material presented in this thesis is, to the best of my knowledge, original and has not been submitted in whole or part for a degree at any other university.

Dimitrios Tsifakis
May 2022

Acknowledgements

Completing a doctorate degree in optimal conditions is generally accepted as a difficult task. It doesn't get easier when it is done by a mature age student with an interdisciplinary background, during a pandemic, and through a rather dramatic school restructure. Despite all that, this seemingly impossible task appears to have reached completion.

I would love to claim all the credit for this incredible result but it would have been impossible to reach the finishing line without the assistance received by multiple individuals during the past four years. Staff from the electronics unit, the mechanical workshop, the school store, the computer unit and, of course, the admin group, have been very helpful with all my sensible and not so sensible requests. I am very grateful for the peer support in the form of acceptance and friendship offered by the fellow students especially Alex, Mahdi, Jia and JB. I am also grateful for the support received from the now defunct CPF team, especially Peter and Horst. The role of the supervisors has been crucial. I couldn't have asked for a better team than Christine and Rod. They not only provided top notch supervision but accepted me as a member of the SP3 team, entertained my occasionally silly ideas and embraced my sometimes pathological enthusiasm for RF and amateur radio. My family in Greece always seemed to be more confident in me finishing this than I was. We may have not been in the same continent these past few years but their positive influence has always been well received. Finally, such an achievement would have been absolutely impossible without the support and encouragement of my partner, Kat.

To all mentioned above and the ones I forgot, I offer my sincere gratitude. Your generosity overwhelms me.

Publications

The following is a list of peer reviewed publications that have been produced as part of the work related to this thesis. Some of the results presented in the following chapters have been adapted from the material in these publications.

- Tsifakis D, Charles C and Boswell R (2021)

  Comparison of Sub-millinewton Thrust Measurements Between a Laser Interferometer and a Load Cell on a Pendulum Balance.

  Front. Space Technol. 2:632358. doi: 10.3389/frspt.2021.632358

- Tsifakis D, Charles C and Boswell R (2020)

  Naphthalene as a Cubesat Cold Gas Thruster Propellant.

  Front. Phys. 8:389. doi: 10.3389/fphy.2020.00389

- Tsifakis D, Charles C and Boswell R (2020)

  An Inductively-Coupled Plasma Electrothermal Radiofrequency Thruster.

  Front. Phys. 8:34. doi: 10.3389/fphy.2020.00034

- Doyle SJ, Bennet A, Tsifakis D, Dedrick JP, Boswell RW and Charles C (2020)

  Characterization and Control of an Ion-Acoustic Plasma Instability Downstream of a Diverging Magnetic Nozzle.

  Front. Phys. 8:24. doi: 10.3389/fphy.2020.00024

- Cairns IH, Charles C, Dempster AG, Tsifakis D et al. (2020)

  The INSPIRE-2 CubeSat for the QB50 Project.

  Space Sci Rev 216, 40. https://doi.org/10.1007/s11214-020-00659-w

Abstract

The popularity of the cubesat form factor has increased dramatically in the last few years. This has resulted in unprecedented access to space by smaller or medium sized organisations, universities and even smaller countries that could not afford such access in the past. However, the vast majority of the cubesats currently in orbit do not have a propulsion system. Such a system is invaluable as it can extend the satellite's time in space, assist with space debris avoidance manoeuvres, coordinate constellation orbits and facilitate a timely and controlled re-entry at the end of the mission. Various satellite propulsion methods have been developed and tested successfully in space over the past 50 years but it is not always possible to scale down a thruster to match the strict requirements of cost, power, size and so on, set by the cubesat platform specification. The objective of this thesis is to explore a number of options that, directly or indirectly, can help with the development of cubesat thrusters.

The presented work includes a cost effective method of measuring the performance of a cubesat thruster in the lab, using a load cell on a hanging pendulum thrust balance. The method shows good performance in comparison with the most expensive displacement measurement method, normally achieved by a laser interferometer.

The thesis continues with the enhancement of the Pocket Rocket, an existing cubesat electrothermal RF plasma thruster. The changes introduced are centred around a change from a capacitively coupled plasma system to an inductively coupled one. These changes result in a more compact and efficient RF matching system which improves the overall efficiency of the thruster system, which is an important improvement for power-constrained cubesats. The new Inductive Pocket Rocket is placed in the Wombat space simulation chamber and a set of direct thrust measurements are made, showing the increase in thrust of up to 50 %, then the plasma is ignited.

Continuing on that theme, the thesis presents a very efficient RF source produced in collaboration with the Stanford SUPER-Lab. It is based on the Class-E amplifier topology, which operates the power semiconductor at the two extremes - fully conducting to fully cut off, spending as little time as possible in the linear, lossy region of the transfer curve. This RF source, matched with a suitable DC power supply, exhibits electrical efficiency of over 91 % resulting not only in better use of the limited power resources on-board the cubesat, but also less waste heat.

The thesis continues with exploring an alternative propellant, naphthalene. Naphthalene sublimates at relatively low temperatures, producing enough vapour pressure to sustain the operation of a cold gas thruster. Cold gas thrusters generally have lower performance compared to other types of thruster systems for satellites but have the engineering advantage of simplicity. To that, naphthalene adds the advantage of having a propellant that is stored in solid state, resulting in negligible propellant storage pressure and higher propellant storage density, compared to the more common gas propellants such as krypton and xenon. Naphthalene also has excellent compatibility with the materials commonly used in the construction of satellites, eliminating the materials compatibility problems (corrosion), that increase the engineering challenge of other, more reactive solid propellants such as iodine. A functional proof of concept thruster is built and its performance is tested in the space simulation chamber, showing the reliable production of up to 0.6 mN of thrust.

Contents

Chapter 1

Introduction

1.1 Motivation

Since the proposal of artificial Earth orbiting satellites by Sir Isaac Newton in 1687, mankind has produced tens of thousands of satellites to serve a multitude of purposes. These purposes include observation of our planet from space for weather prediction [1], natural disaster [2] or ecological monitoring [2, 3], navigation [4, 5], observation of the cosmos for the expansion of our astronomical knowledge [6, 7], provision of various communication services [8, 9], and finally, collection of military intelligence and other defence related applications [10]. The satellites produced and launched in the early days of the satellite era were expensive to build, expensive to launch and therefore accessible only by a limited number of states blessed with the necessary resources. This, together with the limited understanding of the space physics and engineering, made progress relatively slow. Over time, mankind's dependence on the services provided by the various satellites increased dramatically. The combination of technological and scientific progress resulted in a continuous development in the methods and techniques in all aspects of satellite engineering and, as a consequence, is continually making satellite ownership and operation more accessible by those with the need but with limited resources.

Satellite propulsion is the field of satellite engineering that deals with systems designed to modify the orbit of a satellite. This is particularly important for many reasons including major orbit modification, orbital station keeping and attitude control. Major orbit changes need to be made if the satellite orbit achieved by the launch vehicle is not the one needed by the satellite operator. Examples of this include the placing of a low altitude orbiting satellite into a geostationary orbit. Station keeping is the process that ensures the satellite propulsion system is used to compensate for orbit decline due to the interaction with the Earth's atmosphere (drag). Attitude control involves the ability to remove angular momentum to stop the satellite from tumbling, or, perform a full rotation per orbit to ensure antennas or cameras are continuously pointing to the Earth.

The work in this thesis is a contribution to this continuous development in the field of satellite propulsion. The first chapter is concerned with the basic physics of propulsion which is brought into context for a popular category of small and accessible satellites known as cubesats [11]. A set of metrics is introduced which is commonly used for performance comparison. The chapter concludes with a statement on the scope of the thesis and the contribution to this scope given by each chapter.

1.2 Satellite propulsion physics

The motion of objects in space is described adequately, at first approximation, by classical physics and more specifically Newton's laws of motion. When an object is drifting in space, far away from fields that can exert a force F on it, such as the gravitational field, it will continue to travel at a constant velocity u, as predicted by Newton's first law:

$$\sum F = 0 \Leftrightarrow \frac{du}{dt} = 0 \tag{1.1}$$

Ignoring the effect of atmospheric drag, the only force applied to a satellite orbiting the Earth is the gravitational force. This force is perpendicular to its velocity vector and this results in the satellite being in a circular or elliptical orbit around the planet.

In order to change the satellite velocity and therefore the orbiting parameters, a force needs to be applied to the satellite. This force could be produced by the interaction of a device on the satellite with an existing field such as the Earth's magnetic field. This concept is used by magnetorquers and was introduced as early as 1961 [12] for removing angular momentum to control the satellite tumbling. Practical autonomous designs were then suggested and implemented in the following years, as the necessary computing power became available [13, 14].

The most common approach to apply a force to a satellite for orbit manipulation purposes is to use the principle of conservation of momentum by expelling a quantity of propellant. In its simplest form, the force F in this context is called *thrust*, F_T, and is equal to the rate of change of momentum p:

$$F_T = \frac{dp}{dt} = \frac{d(mu)}{dt} \tag{1.2}$$

The change in momentum Δp achieved by the propulsion system in a single actuation of duration Δt (commonly called a *burn*) is known as impulse J:

$$J = F_T \Delta t \tag{1.3}$$

A more useful expression known as the Tsiolkovsky rocket equation, links the satellite's Δu which is the resulting velocity change of the thruster actuation, to the propellant exhaust velocity u_{ex} and the initial m_i and final mass m_f of the satellite.

$$\Delta u = u_{ex} \ln \frac{m_i}{m_f} \tag{1.4}$$

In this case, the mass of the propellant expelled is $m_p = m_i - m_f$. From equation 1.4 it is clear that the only parameter at a fundamental level that can be targeted to optimise the performance of a thruster is the exhaust velocity.

1.2.1 Propulsion system performance metrics

In order to quantify the performance of a propulsion system, a set of metrics is necessary. This set of performance indicators allows meaningful comparison between the various concepts, designs and implementations. The relative weighting of these performance indicators is then decided by the mission designer and depends heavily on the specific mission requirements.

Thrust

Thrust, F_T, is the force that is applied to the satellite as a result of the actuation of its propulsion system. Large changes in orbit will require large thrust and conversely, high precision orbit changes in a satellite member of a constellation may require a much smaller thrust to be applied but in a very controlled fashion. The many proposed and built thruster systems for satellites offer thrust from nano-newtons to newtons.

Total impulse and Delta-v

Delta-v, Δu, is the most common requirement on the propulsion system of a spacecraft given to the propulsion engineers by the mission designer. It is the velocity change needed for a specific manoeuvre, for a example an orbit raising (Hohmann transfer) or the complete mission. This is the output of the Tsiolkovsky equation (equation 1.4), presented earlier and it depends not only on the propulsion system properties but also the mass of the spacecraft. It is therefore not possible to include that performance request to the specifications of a thruster if the details of the spacecraft it will be installed on are not known.

A more common 'overall effect' metric that can be used for a propulsion system is total impulse. It is defined as:

$$J_{tot} = \int F_T dt \tag{1.5}$$

and it refers to the complete life of the thruster, from the beginning to running out of propellant. The total impulse can be increased simply by having more propellant on board, or by improving the thruster's performance.

Specific impulse

As a performance metric, specific impulse I_{sp} indicates how efficiently the propellant is used. It is commonly measured in seconds, as defined by the following formula

$$I_{sp} = \frac{F_T}{g_0 \dot{m}} \tag{1.6}$$

where g_0 is the standard gravity of Earth ($9.81\,\mathrm{m\,s^{-2}}$) and $\dot{m}$ is the propellant mass flow rate. If the average exhaust speed u_{ex} is known, specific impulse can be calculated from the formula

$$I_{sp} = \frac{u_{ex}}{g_0} \tag{1.7}$$

Simple cold gas thrusters achieve a specific impulse of tens of seconds to a couple of hundred seconds. At the other end of the performance spectrum scale, electric propulsion systems commonly achieve a specific impulse in the thousands of seconds.

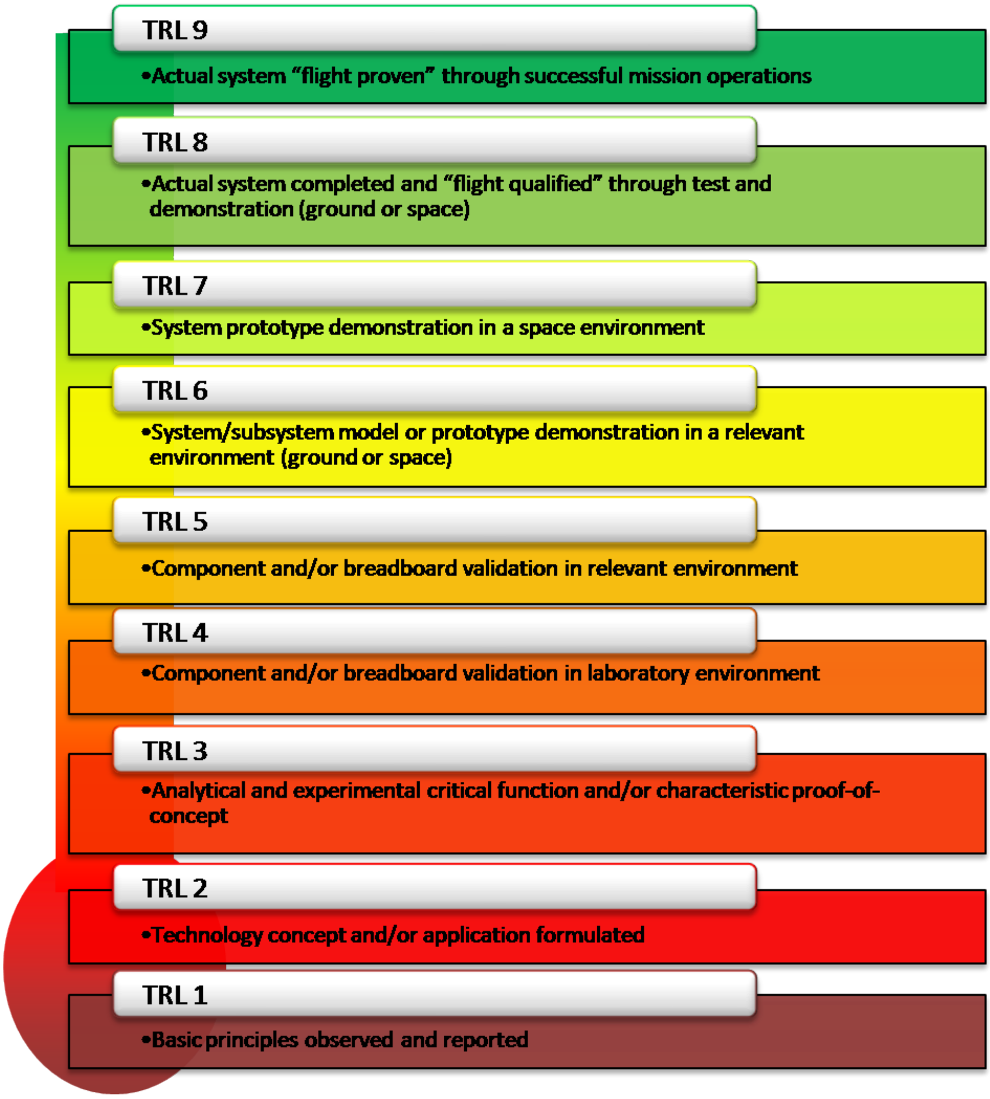

Figure 1.1: Table of the nine Technology Readiness Levels as defined by NASA. Taken from NASA's web site (`https://www.nasa.gov/directorates/heo/scan/engineering/technology/txt_accordion1.html`).

Efficiency

This metric relates to how the available stored energy is converted to kinetic energy increase of the spacecraft during the operation of the thrust system. The stored energy can be chemical energy in the case of chemical propulsion or electric energy stored in batteries and provided to create and accelerate ions in the case of electric propulsion.

Technology Readiness Level

For the satellite mission designer in need of a propulsion system, the medium performance thruster which is available and already tested in orbit is always more valuable than the theoretical design that has better performance but has not yet made it past the proof-of-concept stage. In the 1970's, NASA devised a *Technology Readiness Level* (TRL) scale [15] to allow the comparison of systems at different stages of development. The 9-level scale, seen in figure 1.1, begins with theoretical concepts (TRL1) and finishes with systems that have been successfully used in-orbit (TRL9).

1.3 The cubesat form factor

The cubesat standard [11] was created in 1999 by the California Polytechnic state university (San Luis Obispo) and Stanford university (Space Systems Development lab). The purpose of this standard was to facilitate access to space for academic research and education which, up to that point, had been the privilege of national space administrations and large multinational corporations. Since then, the standard became widely adopted by both the original intended audience but also smaller private and commercial operators. Currently, the number of small satellites including cubesats that are placed in orbit has skyrocketed with the online Nanosate Database [16] listing over 1300 of them. Another effect of this technological disruption is that many countries that had no prior involvement in space and satellites, have now launched cubesats. Examples of such satellites include the original BIRDS mission [17] consisting of satellites from Ghana, Mongolia, Nigeria, Bangladesh and Thailand, the follow up BIRDS-2 mission [18] including satellites from Bhutan, Philippines and Malaysia. At the time of writing, the most recent such mission is MIR-SAT1 from Mauritius [19] which was placed successfully in orbit on the 23rd of June 2021.

Figure 1.2 shows a typical, 2-U cubesat. This particular satellite is I-Inspire-2 and was part of the QB50 mission and was a collaboration between the University of Sydney (USyd), University of New South Wales (UNSW) and the Australian National University (ANU). It was tracked in part by the cubesat ground station built at the ANU and described in detail in appendix A.

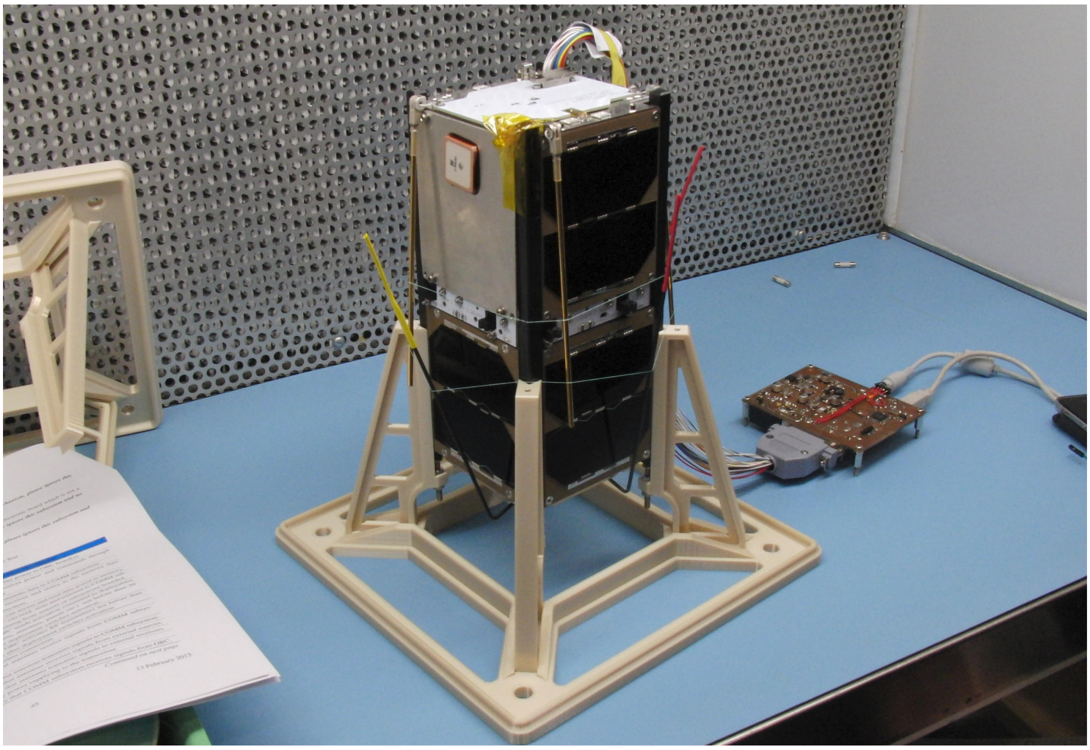

Figure 1.2: Photo of I-Inspire-2 on a stand taken during the space qualification testing that took place at the Advanced Instrumentation Technology Centre (AITC) at Mt. Stromlo. I-Inspire-2 is a typical 2-U cubesat.

1.3.1 Benefits of propulsion for cubesats

The benefits of having a propulsion on-board a cubesat are very similar to those of have one on a larger satellite. Constellations of multiple, smaller satellites are commonly proposed as cost effective replacements of geostationary satellites. Precise orbit control of the cubesats participating in the constellation cannot be achieved without a propulsion system [20–23]. Without a propulsion system, cubesats in low earth orbits (LEO) are at the mercy of atmospheric drag and solar activity and have a limited lifespan in space [24]. Even a modest propulsion system such as the ones described in this thesis, have the ability to extend the life in space of cubesats. A frequent problem encountered by satellite mission specialists is that of the increased probability of a collision of the satellite with space debris [25]. Having a thruster allows the cubesat operator to intervene when an alert is issued for a probable collision [26, 27]. A thruster also allows the cubesat operator to speed-up the re-entry of the satellite, once its mission objective is achieved [28]. A controlled re-entry is a key requirement to reduce the ever increasing number space debris currently circulating the earth. Finally, cubesat thrusters that can provide precise impulse bits can be used as an alternative attitude control system to reaction wheels and magnetorques [29]. Using a thruster system as both a general purpose thruster and an attitude control system is certainly a good strategy in a platform that has severe space and mass limitations, as identified in the following section.

1.3.2 Cubesat propulsion limitations

The cubesat standard imposes various limitations [11] and the main ones are listed below.

Size and mass

A major challenge in producing a propulsion system for a cubesat is the limited space available on-board the spacecraft. The standard [11] defines the building block size (called *one unit* or 1-U) to be 10 cm x 10 cm x 10 cm of volume and a mass no more than 1.33 kg. Larger cubesats can be constructed by combining these units together, for example a 2-U cubesat dimensions are 20 cm x 10 cm x 10 cm and a 6-U 30 cm x 20 cm x 10 cm. Clearly the larger the cubesat, the more space can be allocated to the propulsion system. On a 1-U satellite, the available space realistically cannot be more than one third of a unit once all the necessary subsystems such as power (batteries), on-board computer, radio communications and, of course, payload are accounted for. Larger cubesats can dedicate more space, for example one or two units in a 6-U spacecraft is not unreasonable.

Power requirements

One of the biggest challenges in designing a propulsion system for a very small spacecraft is the restricted power availability from the small photo-voltaic panels and the limited battery capacity. To put things in perspective, the Bulgarian cubesat manufacturer Endurosat[1] advertises an average available payload power of 0.7 W for a 1-U satellite increasing to 0.9 W for a 1.5-U one, both using only the non field-deployable solar panels which are installed on the panels of the spacecraft. In larger cubesats, it is possible to use field-deployable solar panels which results in a vastly increased sunlight collecting area. Consequently, the average available payload power is higher, reaching up to 10 W for 3-U, up to 30 W for 6-U and up to 45 W for 12-U satellites as seen in the Endurosat product catalogue.

---

[1] `https://www.endurosat.com/`

Electromagnetic compatibility

Electromagnetic compatibility problems which are introduced by propulsion systems using high power radiofrequency (RF) or arcs can be exaggerated when the thruster is physically installed very close to systems that are sensitive to such interference, such as the on-board computer and the communications system. Propulsion systems such as cold gas thrusters and resistojets have an advantage as they are not likely to produce potentially disruptive electromagnetic interference while they operate.

1.4 Propulsion options for cubesats

This section briefly describes a number of propulsion systems that have been specifically designed to be able to be used in a cubesat. Not all of the mentioned systems are compatible with the smaller cubesats due to the limited space and power availability as discussed previously. The performance figures mentioned below are taken from the manufacturer's web pages and the addresses are provided in the text.

In general, much of the thruster technology developed for cubesats has happened recently, and it is of high commercial value. This results in relatively limited published material in peer-reviewed journals and conference proceedings, and only general claims published as media releases by the manufacturers. The high interest in cubesat development system is confirmed by the large number of specialised companies focusing specifically on that class of satellites. As a result of this, references in this section are a mixture of peer review material, included in the Reference section, and internet links, included as footnotes.

1.4.1 Cold gas thrusters

In its simplest form, a thruster consists of a reservoir of compressed gas, a valve and a nozzle. When the valve is opened, the gas escapes and thrust is produced. The propellant does not need to be stored in gaseous form but it is advantageous to expel it as gas. The advantage of this approach is simplicity and very low power requirements. The disadvantage is the low performance. Cold gas thrusters have been proposed for constellation control [23] of cubesats.

An interesting example of a cold gas thruster designed for cubesats is the I2T5 built by ThrustMe[2]. Instead of the more conventional compressed gas, it uses iodine as the propellant. The propellant is stored in the solid phase, removing the requirements for a high pressure reservoir and appropriate pressure regulators and valves. The system produces iodine vapour when it is required by the process of sublimation. This is achieved by heating of the reservoir and transfer lines, prior to the utilisation of the thruster. The company claims it achieves 0.2 mN of thrust at an unspecified specific impulse. The power requirement is up to 10 W which is compatible with small cubesats. This specific design does not include a valve in the path of the propellant, instead it relies on the reservoir temperature to control the flow. This approach may limit the usability of this thruster for precision manoeuvres. This technology has been demonstrated in orbit and has therefore achieved a high TRL status.

1.4.2 Chemical thrusters

Chemical thrusters rely in a chemical reaction between one or more propellants which results in the rapid production of hot gas. The elevated temperature of the exhausted gas results in increased performance over the cold gas thruster, however at the expense of increased complexity. Chemical propulsion system are the norm in rocket launching but they are also less frequently used in satellite thrusters. The advantages of chemical propulsion include quick actuation (no warming up required) and much higher thrust compared to other types of thrusters. The trade-off is lower specific impulse.

A common propellant that is used in chemical thrusters is hydrazine (N_2H_2), a highly toxic, inorganic compound. Alternative propellants with lower toxicity (green propellants) have been explored. Valliant Space[3] is an Australian company that is developing a chemical thruster aimed at larger (6-U) cubesats using green, unnamed propellants. The company claims a 20 N thrust and 290 s specific impulse obtained in tests performed in a vacuum chamber, implying a TRL of no higher than 6.

1.4.3 Electric thrusters

A very common technique used by propulsion engineers is to use the energy collected by the solar panels on board to increase the propellant's exhaust velocity. This is a

---

[2] `https://www.thrustme.fr`

[3] `https://www.valiantspace.com/`

very desirable approach as the supply of energy can be considered as unlimited and can be stored in the spacecraft's battery system for use when needed. There are two main approaches in using electricity for propulsion. In the simplest case, the energy is used to heat up the gas in order to simply benefit from the increased exhaust velocity. These thrusters expel neutrals and are relatively simple designs however the performance is not very high. Thrusters falling in this category are commonly called *electrothermal* thrusters.

On the other hand, some electric propulsion systems ionise the propellant, then use the combination of electric and magnetic fields to accelerate and control the ions before they are expelled. Because they expel charged particles, the thruster needs to be used in conjunction with a neutraliser to ensure the spacecraft doesn't charge up. At the same time, there is a corrosive effect of energetic particles interacting with the thruster assembly before being expelled. For these reasons, the implementation of such thruster is a rather challenging task but it has the reward of the highest performance compared to any other thruster technology.

Resistojets

Resistojets make use of electric heating elements (resistors) in the path of the propellant to directly convert the stored electric energy to heat [30]. The propellant is heated up as it crosses the resistor heated section. As shown earlier, the performance increases due to the increased propellant temperature, and the increase is proportional to the square root of the temperature increase. In practice, the temperature is limited by the properties of the materials involved to a factor of no more than three times the performance of the cold gas thruster counterpart. An example of a resistojet thruster designed for small satellites is the 'Comet' thruster, built by Bradford space[4]. It uses water as the propellant. The manufacturer claims a 175 s to 185 s specific impulse and a thrust of 17 mN. It's power requirements are up to 55 W for continuous operation, which restricts its applicability only to larger cubesats.

Arcjet

Similar to the resistojet, the propellant is heated up as it crosses an electric arc, resulting in increased exhaust velocity. Plasma effects as a result of the arc formation are rather insignificant due to low ionisation percentage [31], and it is therefore operating in a similar

---

[4] `https://www.bradford-space.com`

manner to a resistojet. Arcjets, in general, provide better performance than resistojets but that comes at the expense of higher power requirements (generally a kilowatt or higher [30]) making them only suitable for larger cubesats. Aerojet rocketdyne[5] produces MR-512, which is an example of a small, hydrazine fuelled arcjet. It produces over 200 mN at a specific impulse of 502 s, it does however require 1760 W input power which makes it realistically impractical for all small satellites and cubesats. As expected, the published arcjet performance indicates a higher specific impulse but lower thrust compared to using hydrazine in a chemical thruster, as discussed earlier.

Plasma thruster

In the simplest case, the formation of plasma can be used instead of a resistor to increase the temperature of the propellant as in the case of resistojet. In this case, the thruster is called an electrothermal plasma thruster and the expected performance can be similar to that of a resistojet or arcjet. If ions are extracted from the plasma by the use of appropriately biased grids, they can be further accelerated to much higher velocities by the use of an electric field. This technique forms the basis of the gridded ion thruster and it results in high efficiency and specific impulse. ThrustMe[6] produces NPT30-I2, a gridded ion thruster using iodine. Its performance is vastly increased compared to the cold gas predecessor reaching up to 1.1 mN of thrust and up to 2400 s of specific impulse while the power requirement is up to 65 W which is within the capabilities of larger cubesats.

The expulsion of charged particles implies that, over time, the spacecraft will charge up. To avoid that, a neutraliser is utilised to expel electrons at a current of the same magnitude as that of the ion beam. The neutraliser adds to the complexity of the ion thruster but is necessary for the smooth operation of the system. Hollow cathode neutralisers were used successfuly in the early days [32]. Attempts have been made to apply a periodically changing RF voltage on the grid to allow electrons to be extracted during part of the cycle [33].

Hall effect thrusters exploit a cross-field (electric-magnetic) discharge to generate a dense plasma. The electric field orientation is perpendicular to the magnetic field and it is used to accelerate ions produced by the plasma. Hall effect thrusters have been

---

[5] `https://www.aerojetrocketdyne.com/`

[6] `https://www.thrustme.fr`

extensively used in satellites for a long time and their properties are well studied and understood [31]. The majority of them require much higher power (>1 kW) which is not compatible with cubesats. Busek[7] lists BHT-200, a small Hall effect thruster in its products catalogue. This thruster produces 13 mN at a specific impulse of 1390 s, requiring a nominal 200 W of power. It uses xenon, krypton or iodine as the propellant. A similar thruster is produced by Exotrail[8] producing 1.8 mN of thrust with a specific impulse of 800 second, from a system power of 60 W.

Pulsed plasma thruster

Unlike ion and hall effect thrusters, the pulsed plasma thrusters use magnetic fields and a fast pulsed discharge (plasma arc) to mobilise, ionise and accelerate the propellant. Vacuum arc thrusters (VAT) belong to this category. An example of this type of thruster is the micro-cathode arc thruster (μCAT). This thruster uses a metal propellant (titanium), can be operated at a pulse repetition rate of 1 Hz to 50 Hz and can produce thrust in the range of 1 µN to 50 µN with a specific impulse of 3000 s [34]. The very fine control of thrust exhibited by the μCAT thruster has made it a good candidate for attitude control [29]. The electrical power required to operate it is a fraction of a watt which is compatible with the cubesat concept. While the efficiency is high, the achievable thrust is low making this type of thruster suitable for small orbital changes on small spacecraft. A similar pulsed plasma thruster has been proposed for general propulsion work and controlled de-orbiting of the host satellite at the end of the mission [28]. This thruster can produce an impulse bit of 96 µN s (at 3 W) to 360 µN s at 9 W) at a rate of 0.5 Hz, which implies an equivalent continuous thrust of 48 µN to 180 µN which is relatively low for quick manoeuvres on large cubesats.

Field emission electric propulsion thruster

It is possible to produce a thruster system based on the extraction of particles (ions or droplets) from a solid or liquid propellant by an applied high gradient electric field. This is the principle of operation of the Field Emission Electric Propulsion (FEEP). One such thruster system developed for small satellite is the NANO from the company Enpulsion[9].

---

[7] `http://www.busek.com/`

[8] `https://exotrail.com`

[9] `https://www.enpulsion.com/order/enpulsion-nano/`

This thruster uses indium as the propellant, requires about 40 W of power to operate, achieving nominal thrust of 350 µN at a specific impulse greater than 5000 s [35, 36]. This FEEP thruster is a good match to medium or large sized cubesats that can supply the required power. A small FEEP thruster was demonstrated in orbit on a 1-U cubesat, UWE-4 [37]. This gallium propellant thruster was configured to operate at very low power level of about one watt, producing a few micronewtons of thrust at a very high specific impulse, over 1000 s. This is a very good match to the requirements of small cubesats but the relatively low thrust prevents this thruster to be used for quick manoeuvres. A quick thruster action may be needed for example for debris avoidance on short notice, or orbit rising when the satellite is placed in a very low altitude orbit and is severely affected by drag.

1.5 Thesis Outline

The main objective of this thesis is to provide a range of improvements in the existing arsenal of cubesat-compatible thrusters and techniques associated with their operation and evaluation.

A critical part in the development of a propulsion system is that of accurate measurement of its performance in realistic space conditions. Chapter 2 introduces the equipment and techniques used by the SP3 lab that achieve this. The chapter also examines the technique of using RF to produce plasma. This is a practical description of the challenges in matching a plasma generator to the typical RF sources commonly used for the task. It also provides a review of the RF source technologies with a focus on those that are more applicable to a cubesat RF based propulsion system.

Chapter 3 describes a number of technical improvements performed on the thrust balance system to improve the quality of the measurement. This includes the introduction of a magnetic damper system to reduce the effect of the oscillating pendulum every time the thruster being measured is actuated. The chapter introduced a new thrust measurement technique which is based on a load cell. The performance of the load cell is compared to the existing laser interferometer. It is shown that while the interferometer is a slightly better performer, the concept of thrust measurement using an inexpensive load cell has the potential of becoming a valuable verification tool of their propulsion system for those cubesat operators that do not have access to sophisticated thrust measurement equipment.

In chapter 4, the thesis focuses on improvements of the previously described Pocket Rocket electrothermal RF plasma thruster. The original Pocket Rocket is a capacitively coupled plasma system which requires a large and inefficient matching network. An inductively coupled plasma Pocket Rocket is introduced to tackle that problem. The matching network design details is discussed and the prototype thruster is measured in the Wombat space simulation chamber. It is shown that the Inductive Pocket Rocket (IPR) is achieving comparable performance to the original design and the compactness of the matching network makes it a suitable candidate for a plasma thruster to be installed on a cubesat.

Chapter 5 presents the development of an efficient RF generation system which is combined with the IPR in order to produce a complete electrothermal plasma thruster system. This is measured in the Wombat space simulation chamber, using xenon as the propellant.

So far, the propellant used by the discussed thrusters is argon and other, heavier noble gases such as krypton and xenon. While these are commonly used in many thruster designs, they have the disadvantage of requiring very high pressure (thousands of PSI) in the storage tanks. To avoid this difficulty, chapter 6 introduces an alternative propellant which is stored in the solid state, eliminating completely the storage pressure problem. This is naphthalene, commonly called 'moth balls', a polycyclic aromatic hydrocarbon which is relatively inert and compatible with the various materials commonly used in the making of cubesats. The properties of naphthalene are discussed and a proof of concept cold gas thruster is put to the balance for a detailed performance measurement. The chapter discusses the various advantages and disadvantages of this approach with respect to other similar propulsion systems, in the context of a cubesat.

The thesis conclusions are presented in the final chapter. Areas of further research are identified and discussed.

Chapter 2

Apparatus and Technique

2.1 Motivation

This chapter introduces the various apparatus and techniques used to carry out the experiments described in this thesis. The chapter begins with a description of the three vacuum chambers used to evaluate the main aspects of the thruster design. These chambers offer the opportunity to immerse the thruster in space-like vacuum which is necessary during the successive stages of development. The chambers are equipped with pressure gauges to monitor the vacuum conditions and feed through connectors to allow connection of equipment to the outside world. They also contain specific instrumentation such as the pendulum style thrust balance used for direct thrust measurements.

The second half of this chapter focuses on radiofrequency (RF) and the associated techniques used to generate plasma efficiently. RF is a frequently used method for generating plasma in electric propulsion systems. RF power, supplied by RF amplifiers, provides the necessary energy to ionise the neutral gas and transition to the plasma state. The techniques of generating RF and efficiently injecting it into the gas, are described. These techniques are used in the development of the Inductive Pocket Rocket (IPR) thruster, described in chapter 4.

2.2 Vacuum chambers

This section contains the description of the vacuum chambers used for the various experiments described in the following chapters.

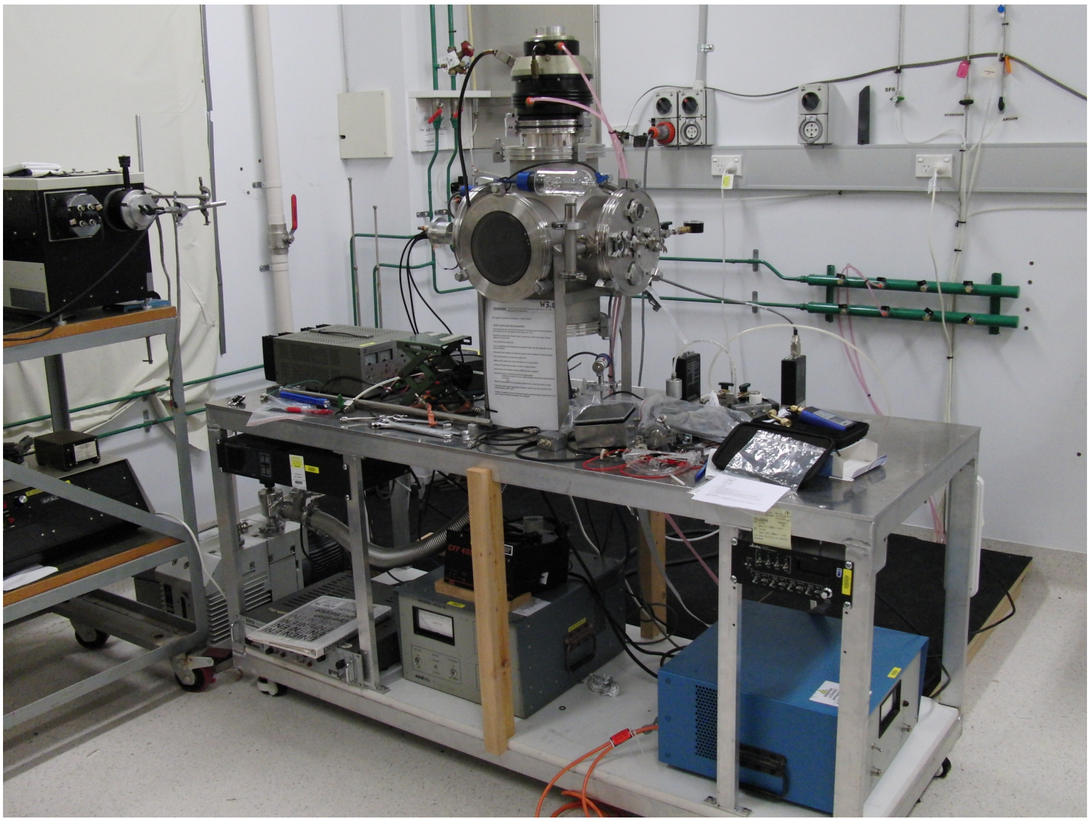

Figure 2.1: Photo of the Lamwich chamber. In the top centre of the photo is the heart of the chamber which is a ISO200 6-way cross. The turbo pump is mounted at the top port. The ENI RF source used to power the plasma thrusters tested in this chamber can be seen directly below the vacuum chamber.

2.2.1 The Lamwich vacuum chamber

The Lamwich vacuum chamber, shown in figure 2.1, is based on a large vacuum 6-way cross with ISO200 ports made by MDC Precision. The chamber has an approximate volume of 50 L. An Alcatel 5402 turbo pump is connected to the top port which in turn is connected to a large Dynavac primary pump. Vacuum readout is achieved by a Granville-Philips Convectron gauge covering from 760 Torr to 10^{-2} Torr, an MKS Baratron with a top range of 20 Torr and an ion gauge which covers the high vacuum range below 10^{-4} Torr.

Argon gas can be supplied for the production of argon plasma. This is done via a supply line connected to the group's compressed gas cage located outside the laboratory. It can be precisely controlled via an MKS model 247C flow controller able to provide a mass flow rate of up to 150 SCCM (Standard Cubic Centimetres per Minute).

There is a dedicated ENI ACG-10 1200 W, 13.56 MHz RF source for the production

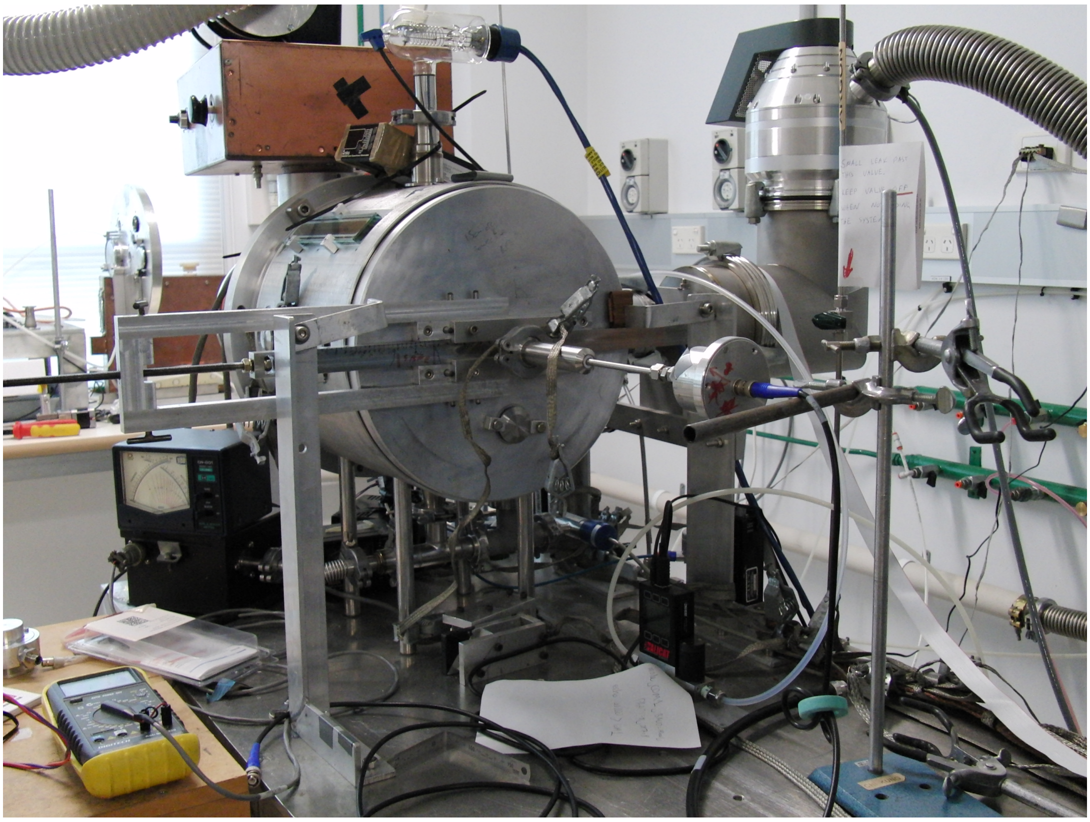

Figure 2.2: Photo of the Chi-Kung chamber. In the top right corner the Adixen turbo pump can be seen. The copper box at the top of the chamber contains the RF matchbox used in prior experiments (not used in the experiments related to this thesis).

of plasma. Alternative RF sources that are available in the lab can be used as needed.

The Lamwich chamber is a general purpose chamber used for quick plasma experiments or evaluation of vacuum compatibility of components. In the context of this thesis, the Lamwich chamber was used for the development of the electrothermal plasma thruster and associated RF matching network, described in chapter 4. It was also used for early experiments of sublimation of naphthalene, as presented in chapter 6.

2.2.2 The Chi-Kung vacuum chamber

Chi Kung, seen in figure 2.2, is a cylindrical plasma reactor (15 cm diameter, 30 cm long) contiguously attached to a 28 cm diameter, 30 cm long diffusion chamber. It was the chamber used in which a current-free, double layer was first observed in an expanding magnetic field [38]. It is equipped with an MVP60 Woosung Vacuum CO, LTD primary pump with a nominal pumping rate of $50\,\mathrm{m^3\,h^{-1}}$. The primary pump is complemented by an Adixen ATP400 turbo pump which is controlled by an Alcatel ACT600 turbo

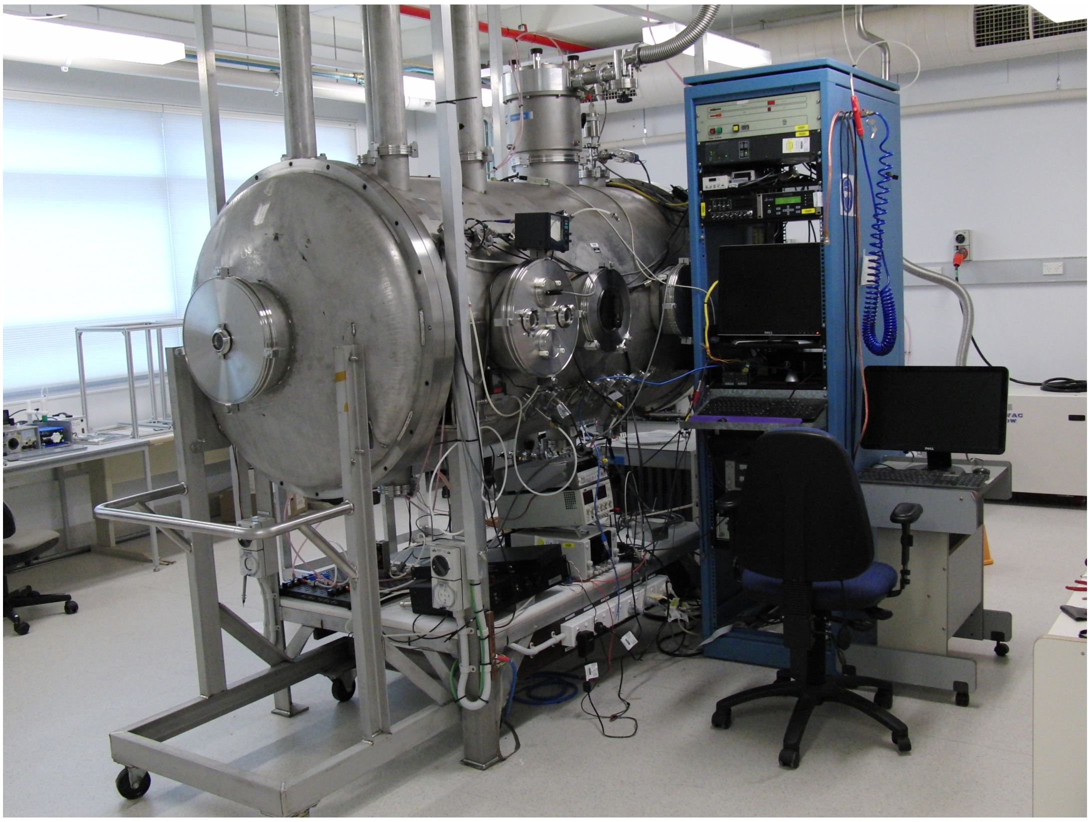

Figure 2.3: Photo of the Wombat chamber. The turbo pump is located at the top of the chamber. The blue rack to the right of the chamber contains part of the instrumentation used for the experiments conducted in it. Access to the chamber is provided by a lid (seen on the left of the photo) which is mounted on a frame with wheels, to allow easy movement of the heavy structure.

controller. The pressure in the chamber is measured by a combination of a Granville-Philips convectron, a baratron and an ion gauge. Similarly to Lamwich, gas is supplied to the Chi-Kung lab from the centrally located argon gas storage cage and the flow rate is controlled by an MKS model 247C flow controller system.

A KF40 connector on the side of the chamber has been used to mount the prototype of the inductive pocket-rocket for development of its RF matching network. This work is described in chapter 4.

Chi-Kung is also equipped with a built in plasma antenna, associated RF impedance matchbox and RF source for generating plasma but this facility was not used for the work conducted for this thesis.

2.2.3 The Wombat space simulation chamber and thrust balance

Figure 2.3 shows the Wombat chamber is a cylindrical chamber (1 m diameter, 2 m long) mainly used for direct thrust measurements of satellite propulsion systems in conditions that as much as possible resemble the conditions of space. The main parameter that is of concern is the establishment of high vacuum which remains good even when the thruster is operating. To achieve this, Wombat is equipped with a large, screw type, dry, Neovac SS120W primary pump. This pump has a nominal pumping speed ot $100\,\mathrm{m}^3\,\mathrm{h}^{-1}$ and can achieve 10^{-2} Torr vacuum. To further enhance the vacuum, a Varian V-1800A turbomolecular pump is installed between the primary pump and the chamber. This turbo has a N_2 pumping speed of $1600\,\mathrm{l\,s}^{-1}$ and can bring the vacuum in the chamber further down to 10^{-7} Torr when there is no operating thruster in it. With the thruster operating, the vacuum in the chamber varies and is a function of the propellant flow rate, $\dot{m}$, and the thruster operating duty cycle. For further improvement of the vacuum, Wombat is equipped with a cryo-pump. The vacuum is measured with a set of vacuum gauges which combined have a large dynamic range. A Granville-Philips convector gauge is used to measure pressure from 760 Torr to 10^{-2} Torr. For pressures below 10^{-2} Torr, an ion gauge is used. Both the convectron and the ion gauge are connected to a Granville-Philips 307 vacuum gauge controller. There is also an MKS Baratron capacitive manometer with a top range of 50 mTorr which is connected to an MKS PR4000B controller to provide accurate vacuum reading in the expected vacuum range resulting from an operating thruster.

The chamber is also equipped with a number of KF40 and KF50 ports which are connected to a variety of feedthrough connectors. These connectors are used to allow an electrical or RF connection of the thruster to the outside world for control and measurement purposes.

The chamber houses the pendulum thrust balance, seen in figure 2.4. A more detailed description of the thrust balance is provided in chapter 3.

2.3 Using RF for the production of plasma

In order to generate a plasma from a gas, energy needs to be provided to induce plasma breakdown and sustain it in a steady state. This energy could be produced by an exothermal chemical reaction, for example in fire, or an energetic particle beam. However, the most common plasma production methods use electric field and exploit the seed charge

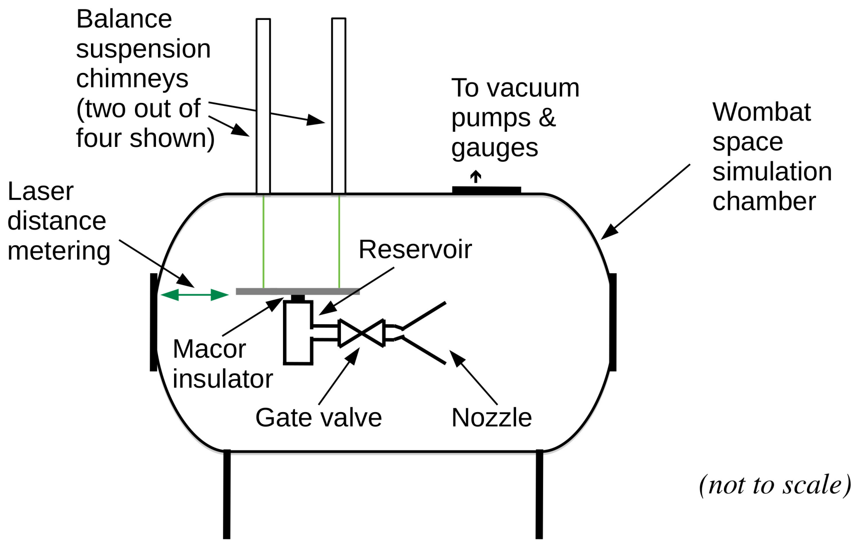

Figure 2.4: Diagram of a cold gas thruster mounted in the Wombat space simulation chamber thrust balance [39–41]. Not seen in the diagram are the feed through connections to valve control, heating elements and other sensors and actuators that are part of the thruster system.

that is already present in the gas (free electrons, charge induced by cosmic rays, etc) to initiate the ionisation process, generate an electron avalanche and reach the plasma steady state [42]. The plasma generation methods include the usage of DC, RF (using frequency of kilohertz to hundreds of megahertz) and microwaves (using frequency typically over a gigahertz). Out of these methods, the usage of RF and microwaves has some advantages including the fact that the electrodes needed to establish the electric field do not need to be in the plasma and are therefore protected from the detrimental erosion effect of plasma exposure [43]. This section will briefly describe the techniques used for generating RF power and effectively transferring this power to a plasma source such as the plasma thruster described in chapter 4.

The block diagram of a typical RF plasma generator is shown in fig 2.5. In this figure, a typical RF source is depicted, consisting of an oscillator (OSC) coupled to a chain of power amplifiers (PA1 and PA2) with enough gain to produce the desired RF power. The oscillator can be a fixed crystal oscillator such as in the ENI 13.56 MHz RF sources used in the laboratory, an example of which is mentioned in section 2.2.1. Alternatively, the oscillator can be based on a direct digital synthesizer (DDS), a voltage controlled oscillator (VCO) or any other frequency synthesis technique. This has the advantage of being able to vary the frequency in order to *hunt* for a better RF match for the plasma load, as described in [39]. The output of the power amplifier chain has most

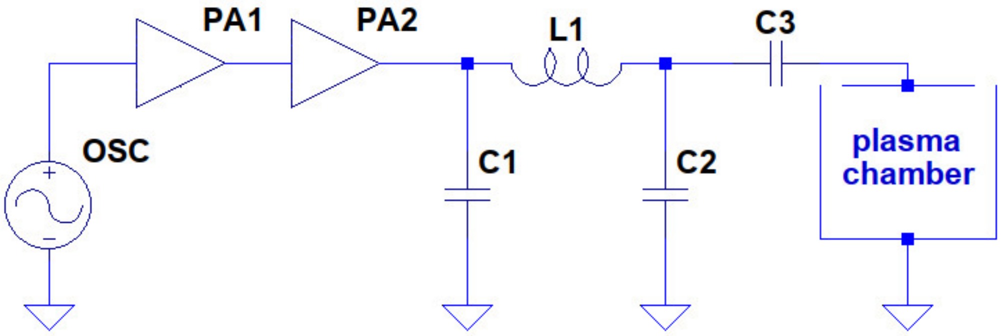

Figure 2.5: A typical capacitively-coupled plasma setup.

commonly a source impedance Z_S equal to the industry standard of $50\,\Omega$. This is done to allow the use of industry standard coaxial cables, directional couplers, standing-wave meters etc, that are commonly designed for that impedance. Past the power amplifiers, an impedance matching network can be seen in figure 2.5, consisting of C1, C2 and L1 forming a Π network. Matching networks such as this one are needed in order to match the load impedance Z_L to that of the source Z_S, as discussed in section 2.3.2 below. The Π network is one of the many possible used to match the impedance of the plasma antenna. The plasma system in figure 2.5 is a capacitive plasma, depicted as a grounded container with one side being an isolated electrode onto which the RF power is applied. Capacitor C3 is needed when the electrode is in contact with the plasma. This is done in order to AC couple the plasma chamber to the RF source, to allow the active electrode to float to the potential that is determined by the ignited plasma in the chamber.

2.3.1 RF amplifier topologies

RF generators for plasma production can be built using many technologies such as vacuum valves (tubes), bipolar transistors and field effect transistors (solid state), and various topologies such as single ended (a single device amplifies continuously or partially through the RF cycle), push pull (one device does half the cycle and another the other half), with single or multiple devices in parallel to allow the production of the desired power. The amplifiers are usually classified on the bias setting (conduction angle) of the amplifying device and the impact it has in the amplification effect throughout the RF cycle.

The suitability of an RF system for a specific application is determined based on its properties. These properties include the maximum RF power delivered to the load, the efficiency of converting input power to RF power, the frequency range (bandwidth) it operates on, the production of spurious RF energy not in the specified operating frequency range, and the ability to tolerate a mismatched load. For stand-alone amplifiers, the properties also include the power gain and linearity.

In the very specific case of RF systems for the production of plasma for satellite propulsion systems, the most important parameters include the power output required to ignite and sustain the desired plasma, the frequency of operation (critical for electron cyclotron resonance (ECR) plasma sources but also influences the matching circuit design) and the power efficiency.

Electrical power is typically provided by solar panels on board a spacecraft. On cubesats, there are physical limitations on size of solar panels which are proportional to the size of the satellite. It is therefore highly desirable to have an RF system of very high efficiency η. Efficiency is defined as

$$\eta = \frac{P_{out}}{P_{in}} \tag{2.1}$$

where P_{in} is the input (DC) power and P_{out} is the RF power as measured at the load. To a large degree, the efficiency of a power amplifier is determined by the class of operation.

Class-A

In Class-A amplifiers, the amplifying device is operated in the middle of the linear part of the transfer curve. This curve is usually given by the manufacturer of the amplifying device and shows the change in the output (for example, drain current on a FET used in common source configuration) as a function of the input (for example the gate voltage of a FET amplifier). The conduction angle, defined as the angle that is part of one sine wave cycle during which the amplifier is actively amplifying the input signal, is 360°. The input signal must not exceed the voltage range of that linear section of the transfer curve. This results in an output waveform with the lowest distortion (best linearity) and has very large bandwidth compared to other classes of amplifiers. Typical Class-A amplifiers have a bandwidth of one or more orders of magnitude.

The main disadvantage of Class-A amplification is the resulting low efficiency which makes it undesirable for RF plasma propulsion systems.

Class-B

Class-B amplifiers have the bias set such that exactly half of the RF cycle is amplified, resulting in a conduction angle of 180°. The produced waveform resembles a half rectified sine wave. This type of amplifier relies on tuned networks at the output to produce a clean sine wave and as such, it has limited bandwidth, determined by the quality factor, Q, of that network. The efficiency is higher than Class-A and can reach up to $\sim 80\%$ on amplifiers using modern semiconductors [1].

Class-C

The conduction angle in Class-C amplifiers is such that only a small fraction of the RF cycle is amplified, therefore the conduction angle is $<180°$. Like Class-B, the amplifier relies on a tuned output network to produce a spurious free sine wave. These amplifiers have low linearity but offer improved efficiency compared to Class-A and Class-B and could be good candidates for the production of RF for a satellite propulsion system.

Class-D and Class-E

Class-D and Class-E amplifiers follow a different approach in order to achieve even better efficiency. In both cases, the amplifying device is switched from fully off (cut off state) to fully on, as fast as possible, avoiding spending time in the *linear* part of the transfer curve. This is done to reduce the losses associated with spending time in this part of the curve. To achieve that, they are typically driven by a square wave. The resulting output of the amplifier is not clean and substantial filtering is required in the form of a low pass filter (LPF) in Class-D. This concept is further refined in Class-E where a specially designed output network enforces that no current is flowing through the device when the voltage across it is high and no voltage is present when the device is passing large current, resulting in minimising ohmic losses [44]. A a result, the efficiency is the highest achievable, approaching 100 % in carefully designed circuits such as those described in [45–48].

---

[1] The most common class used by the high performance modern amplifiers is Class-AB (conduction angle between 180° and 360°). The biasing of Class-AB amplifiers is generally much closer to Class-B than Class-A.

Amplifier class	Efficiency	Linearity
Class-A	Low	High
Class-B	Medium	Medium
Class-C	High	Low
Class-D/E	Highest	Low

Table 2.1: Summary of efficiency and linearity expected for the various classes of RF amplifier.

A 40.68 MHz Class-E amplifier is described in chapter 5. This amplifier was designed around an MRF-101 field effect transistor as an efficient RF source for a plasma thruster for a cubesat-class satellite, as a collaboration between Stanford University and the ANU. It was awarded third place in an RF design competition organised by the transistor's manufacturer NXP[2].

A summary of the typical expected efficiency and linearity characteristics of the various classes of RF amplifiers is given in table 2.1.

2.3.2 RF impedance matching

RF amplifiers are designed to produce the specified RF power on a specific load. The standard output impedance is 50 Ω and it matches the characteristic impedance Z_0 of the coaxial cables commonly used to transfer power from the RF source to the load. Any deviation from that impedance will result in reduced power transfer to the load and, in extreme cases, can cause the failure of the RF amplifier due to large voltages or currents induced by the mismatch [49].

Evaluating the quality of the match

As discussed above, the maximum power transfer from an RF amplifier to a load takes place when $Z_S = Z_0 = Z_L$. In reality, unless a matching network has been implemented, it is likely that $Z_L \neq Z_S$. In this case, part of the power produced by the amplifier (forward power P_F) will be absorbed by the load (P_L) and the remaining power will be reflected back (reflected power P_R), as described by the equation below

$$P_F = P_L + P_R \tag{2.2}$$

---

[2] `https://www.nxp.com/company/blog/homebrew-rf-design-challenge-winners:BL-HOMEBREW-RF-DESIGN-CHALLENGE-WINNERS`

This is captured by the reflection coefficient (reflectance) Γ which is defined as

$$\Gamma = \frac{V_R}{V_F} = \frac{Z_L - Z_0}{Z_L + Z_0} \tag{2.3}$$

where V_R and V_F are the forward and reflected wave voltages. If there is no other source of power connected to the load then the magnitude of the reflection coefficient, $|\Gamma|$, varies from 0 to 1. $|\Gamma|^2$ represents the part of the power that is reflected back therefore $P_R = P_F \times |\Gamma|^2$ and conversely from equation 2.2, $P_L = P_F \times (1 - |\Gamma|^2)$.

There are two ways to express the quality of the match. The first one is the return loss (RL) which is the ratio of the reflected power to the forward power. This is typically expressed in dB according to the following equation

$$RL = 10 \times \log_{10} |\Gamma|^2 = 10 \times \log_{10} \frac{P_R}{P_F} \tag{2.4}$$

The second way to express the magnitude of a mismatch is the standing wave ratio (SWR) more commonly given as the voltage standing wave ratio (VSWR)

$$VSWR = \frac{1 + |\Gamma|}{1 - |\Gamma|} \tag{2.5}$$

If the forward and reflected power is known, the SWR can be calculated by the equation below

$$SWR = \frac{1 + \sqrt{\frac{P_R}{P_F}}}{1 - \sqrt{\frac{P_R}{P_F}}} \tag{2.6}$$

The measurement of SWR is the most common method used to quantify the quality of matching as it can be achieved with an inexpensive SWR bridge. This type of instrument has very low insertion loss and is usually left permanently connected between the RF source and the load, just before the matching circuit. An example of an SWR meter is shown on figure 2.6.

A perfect $50\,\Omega$ load results in a SWR of $1:1$. The loss occurring due to an impedance mismatch is called a mismatch loss (ML) and can be calculated in dB by the formula

$$ML = 10 \times \log_{10}(1 - |\Gamma|^2) = 10 \times \log_{10} \frac{P_F}{P_L} \tag{2.7}$$

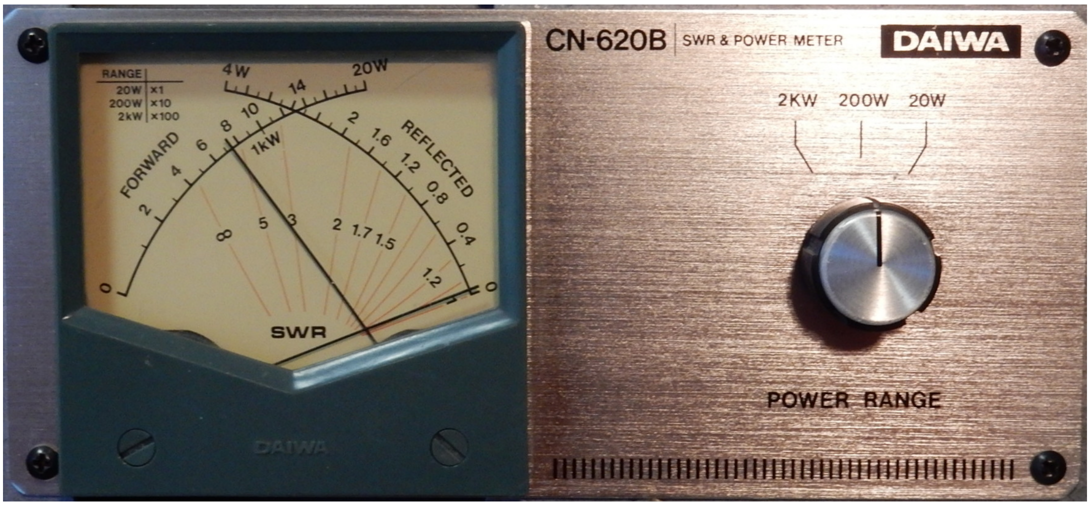

Figure 2.6: A typical cross-needle SWR meter showing 75 W forward and 0 W reflected power. The readout of the SWR is done by observing the red line under the crossing of the two needles. In this case, the SWR is 1 : 1 implying a load of 50 Ω.

In practical terms, a match is considered good if the SWR remains below 1.5 : 1 in which case only $\sim 4\%$ of the power is reflected, a value that is generally within the tolerance of the measuring equipment. If the SWR climbs to 2 : 1, the reflected power is $\sim 11\%$ and it needs to be accounted for when it is important to know the power deposited in the plasma.

To avoid the problems of a mismatch mentioned above, an impedance matching network can be used to transform the load impedance to the desired 50 Ω. This consists of a networks of inductors, capacitors and transmission lines which, when connected together, perform this transformation. Because these passive components are exposed to the voltages and currents associated with the power produced by the RF source, it is desirable that they have limited losses. The loss of inductors and capacitors is expressed by their quality factor Q and is given by the formula

$$Q = \frac{X}{R} \tag{2.8}$$

where X is the reactance which can be inductive (X_L) or capacitive (X_C), and R is the respective loss. Both the reactance and loss are functions of the frequency. The loss in inductors is typically dominated by the ohmic resistance of the winding resulting from the skin effect and the loss of the core, if one is used. In capacitors, the loss is typically related to the dielectric used and their typical Q values are higher than those of inductors used in matching networks.

The Smith chart is a graphical tool used to represent impedances and graphically calculate impedance transformations to solve any given impedance matching problem [50].

The role of the transmission line

An RF power transmission line is typically used to transfer power from the RF source to the load (plasma). The most common transmission line used is the $50\,\Omega$ coaxial cable. Another type of transmission line used is the balanced line consisting of two parallel conductors. It is commonly placed between the RF source and the impedance matchbox and sometimes between the matchbox and the plasma antenna.

The section between the RF source a tuned matchbox will exhibit loss according to the manufacturer's specification for matched conditions. This loss, usually given in $\mathrm{dB\,m^{-1}}$ for a given frequency, depends on the type of coaxial cable used and is generally low for the typical 13.56 MHz systems, increasing with frequency. When a section of transmission line is used between the impedance matching box and the plasma antenna, the losses are generally higher and depend on the SWR. In this case the transmission line must be kept as short length as practical and the impedance transformation it provides to the impedance of the antenna needs to be taken into account when calculating the components of the matching network.

2.3.3 RF to plasma coupling techniques

There are two main techniques used to employ an RF source in order to generate plasma. These are the capacitively coupled plasma (CCP) and inductively coupled plasma (ICP) methods, and they are discussed below.

Capacitively coupled plasma

The capacitively coupled plasma is a technique which relies directly in the electric field between two electrodes, produced by connecting them to an RF source. This was briefly discussed in section 2.3 and a typical system can be seen in figure 2.5. The resulting impedance of a CCP system as seen at the point to the right of capacitor C3 in figure 2.5 is going to be some resistance in series with some capacitance. A typical value of the

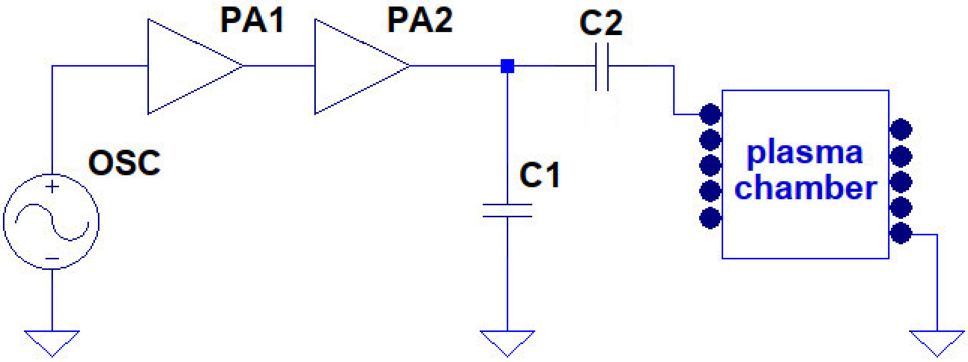

Figure 2.7: A typical inductively coupled plasma setup. The RF source consists of the oscillator (OSC) and a chain of two power amplifiers (PA1 and PA2). C1 and C2 form the matching network which connects to a coil that surrounds the plasma chamber.

load impedance Z_L for a CCP system such as the original Pocket Rocket electrothermal thruster, is $(2 - 300\mathrm{i})\,\Omega$. The resistive part of this impedance is affected by the gas pressure in the plasma chamber, with the value increasing as the pressure increases. The capacitive reactance is mainly affected by the physical dimensions of the discharge volume and electrode configuration.

Inductively coupled plasma

Similarly to the capacively coupled plasma system, the inductively couple plasma (ICP) system, seen diagrammatically in figure 2.7, initially relies in the electric field produced by the RF current flowing in an inductor. Once ignited, however, the magnetic field produced by the inductor (antenna) induces a current in the plasma which in turn results in the generation of plasma by the collisional transfer of energy from the ions in the induced current to the neutrals in the gas. The energy transfer mechanism between the winding of the antenna and the induced current in the plasma is similar to that of a common electrical power transformer. Z_L in this case has an inductive reactance. For the typical ICP system such as the one described in chapter 4 it is $(3.2 + 56\mathrm{i})\,\Omega$. Such impedance can be matched to $50\,\Omega$ by using capacitors only, as seen in figure 2.7 (capacitors C1 and C2).

2.4 Summary

This chapter provided a description of the equipment that is used for the experiments introduced in the following chapters. It begun with an introduction to the vacuum chambers that are part of the SP3 laboratory and highlighted the use of this equipment for the experiments conducted for the purpose of this thesis, as presented in the following chapters. The chapter continued to discuss the use of RF for the generation of plasma, focusing on techniques of RF generation, impedance matching and the use of RF in the production of plasma.

The following chapters will examine in detail the experimental work conducted as a part of this thesis. Chapter 3 revisits the Wombat space simulation chamber described in section 2.2 of this chapter and more specifically, the direct thrust measurement facility. An alternative method of thrust measurement suitable for cubesat-class thruster systems is proposed, implemented and evaluated. Chapter 4 makes use of the RF techniques described in section 2.3 to improve the Pocket Rocket design. To match the improved thruster described in that chapter, the development and evaluation of a Class-E amplifier is presented in chapter 5. Finally, in chapter 6 the design and implementation of a proof of concept cold gas thruster using naphthalene as the propellant, is presented. This thruster was extensively tested in the Wombat chamber described earlier in this chapter.

Chapter 3

Thrust balance improvements

3.1 Motivation

The performance of a thruster can be calculated or measured using many different techniques. At the early stages of development, thrust could be calculated via complex simulations that are based on the Navier-Stokes equations which describe the movement of fluids, or direct simulations using Monte Carlo techniques. Such simulations are usually performed using sophisticated computational fluid dynamics software such as that described in [51] and [52]. If the thruster uses plasma, the simulation increases in complexity as the reactions occuring in the plasma need to be taken into account [53, 54].

While the simulation approach to the measurement of thrust maintains advantages such as ease of evaluation of the effect of changes and the ability to test novel designs in conditions that are difficult or impossible to replicate in the lab, it has an inherent disadvantage: the performance evaluation of a thruster using a computational approach is going to be as good as the assumptions made and fed to the software.

In order to overcome this limitation, a direct thrust measurement is highly desirable. Data collected from the direct measurement can guide the simulation and, in more practical terms, confirm or disprove the performance claims of the thruster manufacturer. The latter is an important verification step of a cubesat user that has purchased an off-the-shelf thruster system and needs to confirm the claimed performance. Given the relatively low budget of most cubesat missions, there is a need for a simple thrust measurement system that can be easily implemented by cubesat operators with limited budget, such as universities and smaller, space related businesses taking their first steps in launching satellites.

This chapter provides a brief review of the most common direct thrust measurement techniques and proposes a new technique for thrust measurement that is applicable to

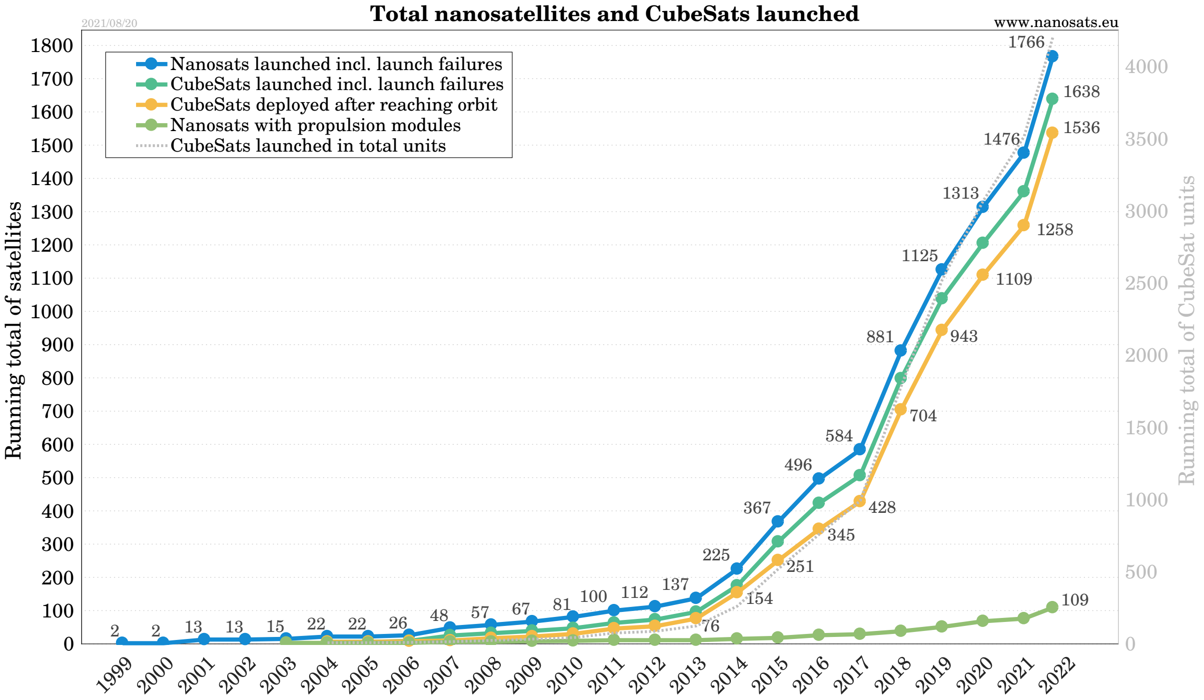

Figure 3.1: Plot of cubesat number over time taken from [16]. The dataset was obtained in August 2021. It shows that only 109 nanosats out of the 1766 nanosats launched (6.17 %) had a propulsion system. It is not shown how many of these propulsion equipped satellites were successful in demonstrating the propulsion capabilities of their thrusters.

cubesats. It compares direct thrust measurements of a cold gas thruster using a pendulum thrust balance equipped with a sensitive laser interferometer, to using a load cell (force sensor) to measure the thrust directly with the thruster installed on the same pendulum balance. The combination of a pendulum and load cell results in a cost effective system for direct thrust measurement compared to the alternative existing methods. This offers a direct thrust measurement of interest to entry level cubesat operators that wish to evaluate their thrusters first hand.

3.2 Challenges of Cubesat thruster measurements

As hinted in the introduction, small satellites having unit dimensions of $10\ cm \times 10\ cm \times 10\ cm$ and mass up to $1.33\ kg$ [11] or multiples of this, have become increasingly popular of late since they can be constructed from simple Commercial Off The Shelf (COTS) components and systems. It is noted that while propulsion systems are available as COTS components, there is no availability of COTS thrust measurement systems, presumably due to complexity and cost reasons.

The introduction of the various nanosat platforms (the most common of which is the cubesat) has allowed small research groups in universities, small to medium enterprises and hobbyists to engage in a variety of areas of space research and engineering. As of August 2021, over 1,700 nanosats the vast majority of which are cubesats have already been placed in orbit. The evolution of the cubesat numbers over time can be seen in figure 3.1, taken from the Nanosat database [16]. According to this source, only about 6 % have propulsion modules and of these, very little information on the actual testing procedures, laboratory performance and whether the thruster was successful in flight is publicly available.

Examples of publications that demonstrate successful use of a thruster system on nano-satellites include the formation flying of CanX-4 and CanX-5 [55] and more recently the NanoFEEP propulsion system on UWE-4 [37]. Of primary interest to the further development of nano-satellites is the propulsion module and in particular, the direct thrust measurement under space conditions. A common technique used for thrust measurement is mounting the thruster on a pendulum and measuring the pendulum displacement when the thruster is activated. Usually, the displacement is measured directly, using a laser interferometer.

3.3 Direct thrust measurement methods

3.3.1 Pendulum displacement method

One of the most typical techniques used for thrust measurement is the concept of the pendulum balance. In its simplest form, a pendulum thrust balance can be based on a hanging pendulum [40, 56], an inverted pendulum [57–59] or be a torsional balance [60–65]. Figure 3.2 shows the three configurations of the pendulum principle for thrust measurements.

There are also more complicated implementations of this, such as the stand for vertically oriented thrust measurements system described in [67]. Mechanical systems to amplify the horizontal movement can be implemented resulting in increase sensitivity in a compact package at the expense of even higher complexity [68]. A technique that has been successful in measuring low thrust in the micronewtons range is the nulled-pendulum

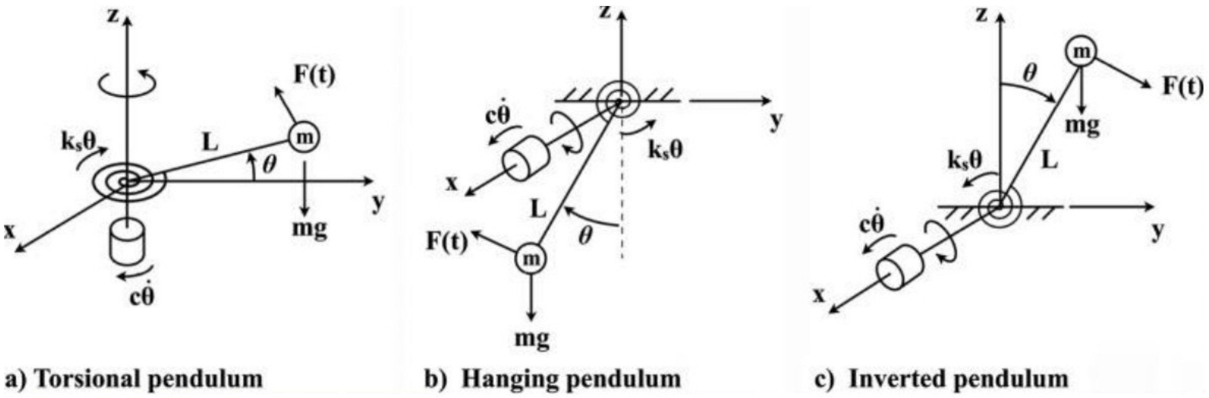

Figure 3.2: The principle of the three common configurations of a pendulum for thrust measurements, taken from [66]. In this diagram, $F(t)$ represents the thrust, mg is the gravitational force, θ is the angular deflection caused by the thrust, L is the length of the arm of the pendulum and c is the damping constant.

principle [69]. In this case, the pendulum is not allowed to move by applying a force equal in magnitude to the thrust but with an opposite sign.

In all cases, the application of thrust results in a displacement which is a function of the thrust. The displacement is commonly measured with a laser interferometer or a linear differential voltage transformer (LDVT).

The theory of operation of all of these methods is described in detail in [66]. In order to keep the test platform stable and horizontal, it is common to attach rigid arms with metallic flexures at both ends, to each corner of a rectangular plate; the other end of the arms being fixed some distance vertically above. The metallic flexures are oriented such that the movement by the action of the thruster is allowed. Together with gravity, the flexures contribute to the restoring force of the pendulum. When the thruster is activated, the distance away from the normal can be determined with a laser interferometer and when correctly calibrated yields a thrust proportional to displacement. The sensitivity of the system is proportional to the suspended mass which includes the mass of the thruster under test.

An elementary characteristic of a pendulum is that it will oscillate and given there is no air friction in vacuum, it may take a very long time for the system to come to a rest. These oscillations can be damped actively using solenoids or simply with a magnet generating eddy currents in a metal tube. An alternative to using the displacement of a pendulum for thrust measurement is placing a solenoid and magnet in a feedback loop which supplies the current required to prevent all motion. In this case, the force of the thruster will be proportional to the current through the solenoid necessary to prevent movement. A benefit of this method is that the natural frequency of the pendulum does not affect the measured values, however the measurement bandwidth will be limited by frequency of the feedback loop.

3.3.2 Momentum flux measurement method

An indirect method of measuring thrust is that of measuring the momentum flux of the exhausted material impinging on a target placed near the exhaust of the thruster. The force measured on the target, together with modelling of the exhaust plume of the thruster can then be used to infer the thrust produced by the thruster under test. In this method, care needs to be taken to ensure the target does not interfere with the normal operation of the thruster. Typical measurements of momentum thrust include [70–72], the latter containing a comparison between direct and indirect thrust measurements, concluding in this case the two methods produce very similar results.

3.3.3 Load cell in a standard weight scale configuration method

Load cells are force-to-electrical signal converters, also known as force transducers or force sensors. They are frequently found in electronic scales measuring weight and they have a range varying from micrograms to tons. They are commonly used to measure thrust from conventional chemical rockets. They can also be used to measure thrust from microthrusters producing thrust less than a millinewton. One way to achieve thrust measurement using a load cell is to construct a standard weight scale and place the thruster on it with the nozzle facing up (gravitational force is parallel to the thrust force and has the same sign). Since the thruster exhaust faces up, the scale will record an increase in the measured value when the thruster is switched on, which is equal to the thrust. Examples of such thrust stand are given by Conde et al [73] and Karadag et al [74]. The disadvantage of this method is that the measurement system must be able to measure the weight of the thruster F_w which is typically many orders of magnitude larger than the thrust F_T. The selected load cell must be capable of supporting and measuring F_w which results in decreased resolution when measuring thrust in the sub-millinewton range.

3.3.4 Load cell on a pendulum method

A strain gauge or a load cell can be also used to measure the thrust directly in a pendulum stand. Examples of such application have been published for torsional pendulum [75] and inverted pendulum [76]. This present study describes the direct thrust measurement by using a load cell in a conventional hanging pendulum, where the thruster is placed in the hanging pendulum thrust stand and a load cell is placed between the pendulum and a rigid point, along the axis of expected pendulum movement when the thrust force is applied. Measuring the thrust directly instead of measuring the displacement has the advantage that the sensitivity of the metering system is not as strongly dependent on the mass of the thruster that is suspended on the hanging pendulum. This is due to the fact that the movement of the pendulum when configured with the load cell is much less than when it is configured with the laser system When measuring displacement, the deflection angle θ (and therefore the displacement) caused by a thrust F_T from a pendulum with a combined suspended mass m causing a gravity force $F_G = mg_0$ is given by the formula $sin\ \theta = F_T/F_G = F_T/mg_0$ which implies smaller angles for increased pendulum suspended mass. In the case of the direct thrust measurement using the load cell, $\theta \approx 0$ removing the link of the thrust measurement to the suspended mass.

The hanging pendulum with the load cell configuration can be seen diagrammatically in figure 3.3. The load cell is equipped with an adjustment screw which is rotated until contact is made with the pendulum. The pendulum is pushed away from its rest position and it applies a force to the load cell. The screw then is further adjusted until the measured force is about half of the maximum force allowed on the load cell, allowing enough head room for the expected thrust. This allows the use of a very sensitive load cell with a low maximum force which is more suitable for sub-millinewton measurements. In the present study, thrust is generated and controlled using a well studied cold gas thruster using argon as the propellant [52].

3.4 Wombat Space Simulation Chamber with cold gas thruster

The thrust measurements were conducted in the Wombat space simulation chamber [39, 40] shown in figure 3.4, comprising a 1 m diameter, 2 m long vacuum chamber fitted with

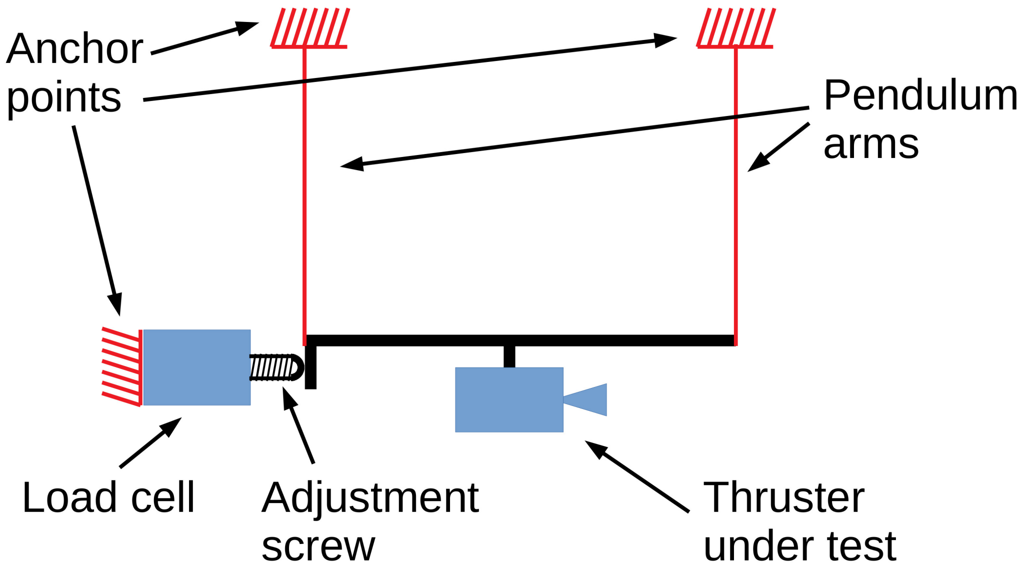

Figure 3.3: Diagram of thrust balance configured for measurements using the load cell. Only two out of the four pendulum arms are shown. The adjustment screw is firmly attached to the load cell and it is extended until contact is made with the pendulum frame. It then is extended a second time until the indication on the load cell shows approximately half of its rated full force.

a dry vacuum pumping system (scroll, turbomolecular and cryogenic pumps) along with a suite of access and viewing ports for space qualification testing. The vessel is pumped down to a base pressure of about 10^{-6} Torr using the $70\,\mathrm{m^3\,h^{-1}}$ scroll and $1800\,\mathrm{L\,s^{-1}}$ turbomolecular pumps but not the cryogenic pump. Wombat is routinely used for the experimental testing of various types of thrusters and their propellant and electric subsystems [41] and is equipped with a thrust balance validated in-house [39, 40] as well as in a number of laboratories [77, 78].

An electrically grounded chassis can be suspended from the top of four *chimneys* and act as either a thrust balance or be locked onto the vacuum vessel. The thrust balance consists of a four arm pendulum suspended frame with the thruster being mounted on the frame. In operation, the thruster produces a displacement from the rest position which is proportional to the thrust force, which can be measured by an ILD7100 laser triangulation displacement sensor with a resolution of $0.1\,\mu\mathrm{m}$, installed on the chamber and pointing to a target on the pendulum. The balance has been designed with a built-in calibration system comprising a set of accurately measured weights which are placed on the balance via a pulley and controlled by a stepper motor. This calibration system is used in each measurement to confirm the conversion constant from displacement to

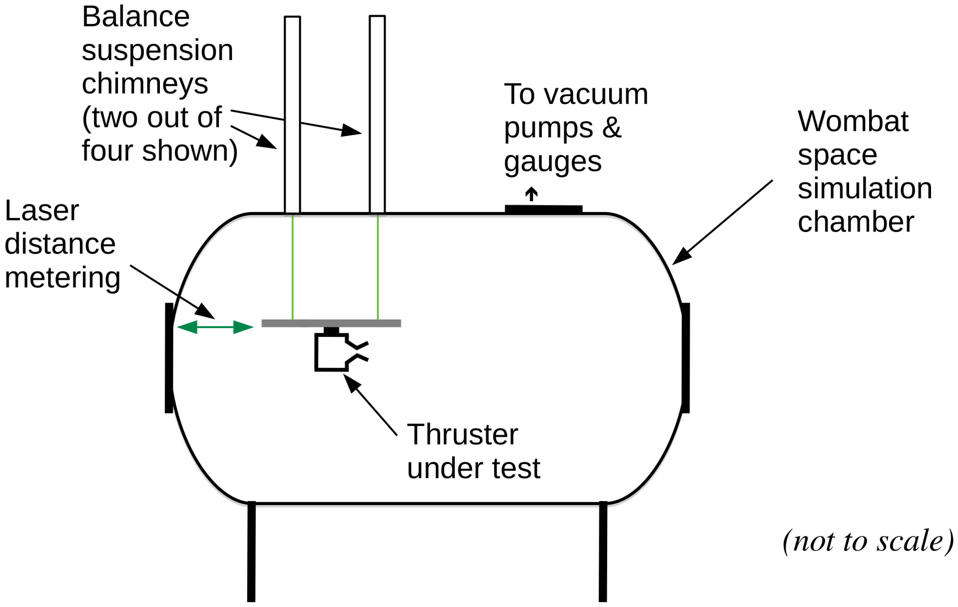

Figure 3.4: Diagram of the laser distance metering (interferometer) thrust balance in the Wombat space simulation chamber. The cold gas thruster is shown suspended on the balance.

force. The calibration process involves installing the thruster to be measured on the balance, then placing the weights on the balance by operating the stepper motor and recording the balance reaction. From this, a calibration factor is produced which takes into account the mass of the thruster. A set of vacuum feedthrough connections on the vacuum chamber was used to enable electrical connections and thruster control signals transfer from equipment that is located outside the chamber. A diagram of the Wombat thrust balance showing a thruster on the balance frame and the positioning of the laser distance metering system is seen in figure 3.4.

The argon cold gas thruster used for the tests consists of a 4 mm inner diameter ceramic tube which is fed with a user selectable argon flow rate. The argon is stored in a pressure cylinder located outside the vacuum chamber and the flow is controlled by an Alicat Scientific mass flow controller. The mass flow rates used in this experiment range from 25 SCCM to 200 SCCM and result in choked flow conditions, as described in [41, 52]. A calibration measurement is done at the beginning and end of each measurement campaign to ensure that the correct translation is performed from displacement to thrust, taking into account the exact mass of the thruster as installed for the measurement.

When a constant force is applied to the frame by the thruster, the pendulum moves from its rest position and starts oscillating with a period of about one second which can be damped over a few seconds using a magnet attached to the balance moving in a

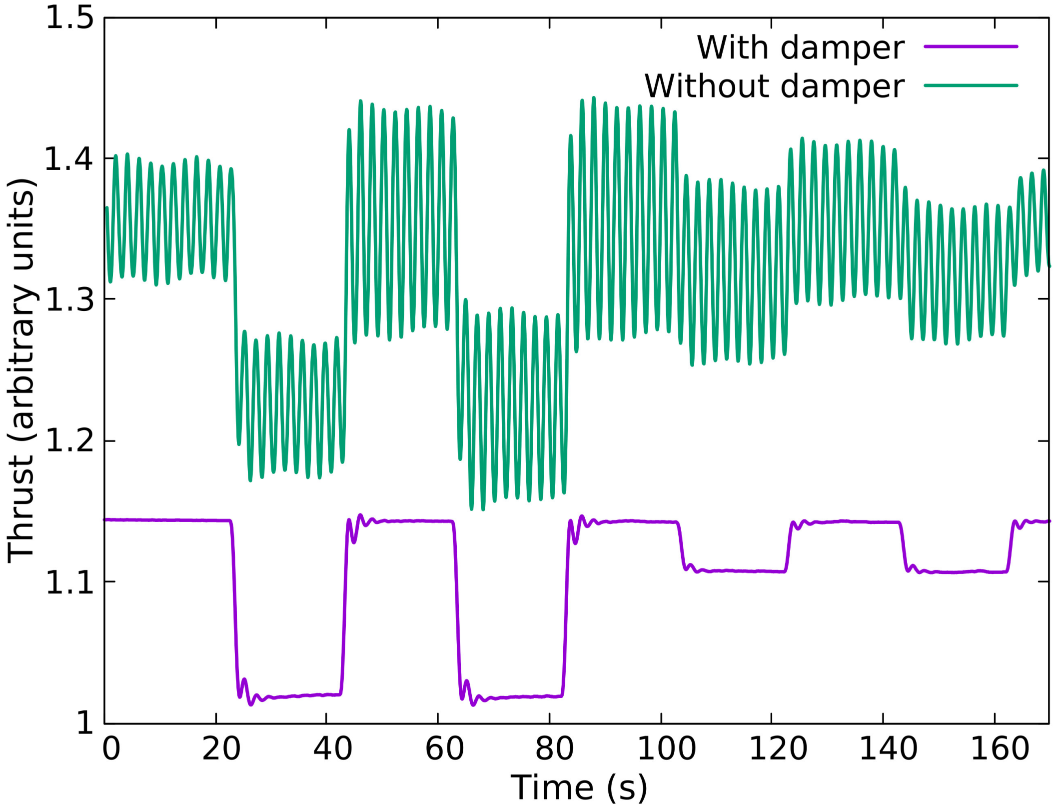

Figure 3.5: The effect of the magnetic damper when used in the laser interferometer pendulum. The top trace (purple) was recorded without the damper and the bottom trace (green) was recorded with the damper configuration. In both cases, the cold gas thruster on the stand was set up to do two 20 s burns at 500 SCCM followed by two 20 s burns at 200 SCCM. In both cases, the sampling is set to 312.5 Hz with a moving average depth of 256.

copper tube. The typical effect of the magnetic damper (also discussed in chapter 4 and shown in figure 4.6) can be seen in figure 3.5, where the cold gas thruster was set up to perform two 20 s burns at 500 SCCM followed by two burns at 200 SCCM. The top trace (green) shows the interferometer output with the damper removed from the balance, exhibiting a constant oscillation at the pendulum's resonant frequency which is about 1 Hz. The bottom trace (purple) shows the same thruster sequence with the damper installed. In this case, the oscillation is mostly dampened quickly with a damping factor $\zeta < 1$ (underdamping) resulting in a clear trace. There was no change observed to the zero drift as a result of the addition of the damper.

3.5 Load cell setup in Wombat

To evaluate the direct thrust measurement performance of a load cell, the Wombat thrust balance was modified as follows. A load cell was removed from a Diamond Pocket Scale which is a low cost jeweller's scale (tens of dollars), purchased online. There were no identifying marks on the load cell making it impossible to get further information from the manufacturer however an assessment of the range and resolution can be made from the scale advertised properties. The scale has an advertised maximum allowed weight of 20 g and a resolution of 1 µg. The force F_w resulting from the mass m placed on the scale due to gravity can be calculated by the formula $F_w = mg_0$ where g_0 is the standard gravity[1]. This results in a maximum force of $\sim$ 196.2 mN and a resolution of $\sim$ 9.81 µN. These operating parameters are compatible with thrust measurement in the sub-millinewton range. The load cell is a Wheatstone bridge which is provided with an appropriate excitation voltage and, when a force is applied on it, becomes unbalanced and produces a small voltage which is proportional to the applied force. This load cell does not have any temperature compensation mechanism which was confirmed by blowing hot air at with no load, resulting in dramatic changes in the readout. However, this is not a significant drawback in a cold gas thruster evaluation as the load cell will be in vacuum during the measurements, protected from room temperature changes. An Avia Semiconductor HX-711 load cell amplifier/digitiser was used to provide the excitation voltage to the load cell and digitise the resulting force induced voltage. The digitiser has an advertised 24 *bit* resolution but it was discovered in practice that the effective resolution is less than that, with the lower few bits being noise. Even if the effective resolution is 16 *bit* and assuming the maximum expected thrust force occupies the complete voltage measurement range of the digitiser, the obtainable theoretical resolution is $\sim$ 3 µN which is acceptable. The noise amplitude measured with the load cell to the ADC was found to be around 80 µN peak-to-peak, which is a factor of 4 worse than the noise present on the interferometer (around 20 µN) during the measurement campaign.

The amplifier/digitiser is installed inside the Wombat vacuum chamber, very close to the load cell, in order to minimise electrical noise pickup. Although the cold gas thruster does not produce any direct electrical interference, in the lab environment there are many sources of conducted and radiated noise including large electic motors, switched

---

[1] The deviation in the gravity constant at the measurement site from the standard gravity are negligible compared to other sources of error, so the standard gravity is used in all calculations in this thesis.

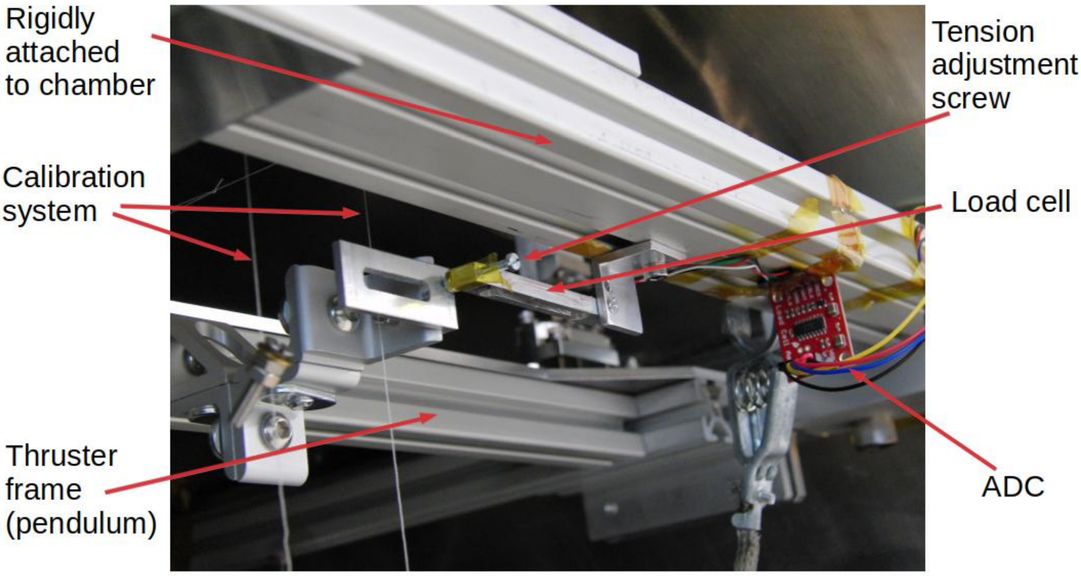

Figure 3.6: Photo of the load cell installed on the thrust balance. In this photo, the load cell can be seen in the centre. The right side of the load cell is rigidly connected to the chamber via an L-bracket and the left end touches the hanging pendulum via an adjustable screw. The load cell amplifier/digitiser red printed circuit board can be seen in the middle-right of the photo. Part of the calibration mechanism can be seen in the middle left of the photo.

mode power supplies, apparatus using radio frequency (RF). A photo of the load cell installation can be seen in figure 3.6, where the load cell can be seen (centre of photo), rigidly attached to the chamber via an L-bracket on its right side. On the left side of the load cell the screw that allows precise contact with the pendulum frame is seen. The purpose of the screw is to allow a high level of control of the pre-loading of the load cell by pushing against the pendulum. In the photo the amplifier/digitiser can also be seen on the right side. The digital signals are routed outside the chamber via appropriate feedthrough connectors and are read by an external microcontroller. The microcontroller is programmed to read the load cell values at a constant rate limited to 10 samples per second by the digitiser, and make them available via a serial port to a computer. The existing calibration system used for the interferometer calibration and described earlier, was also used to perform the calibration for the load cell.

3.6 Experimental results and comparative analysis

Before beginning the comparison of the two systems (load cell and laser interferometer) with an operating thruster, measurements of noise were conducted with the thruster

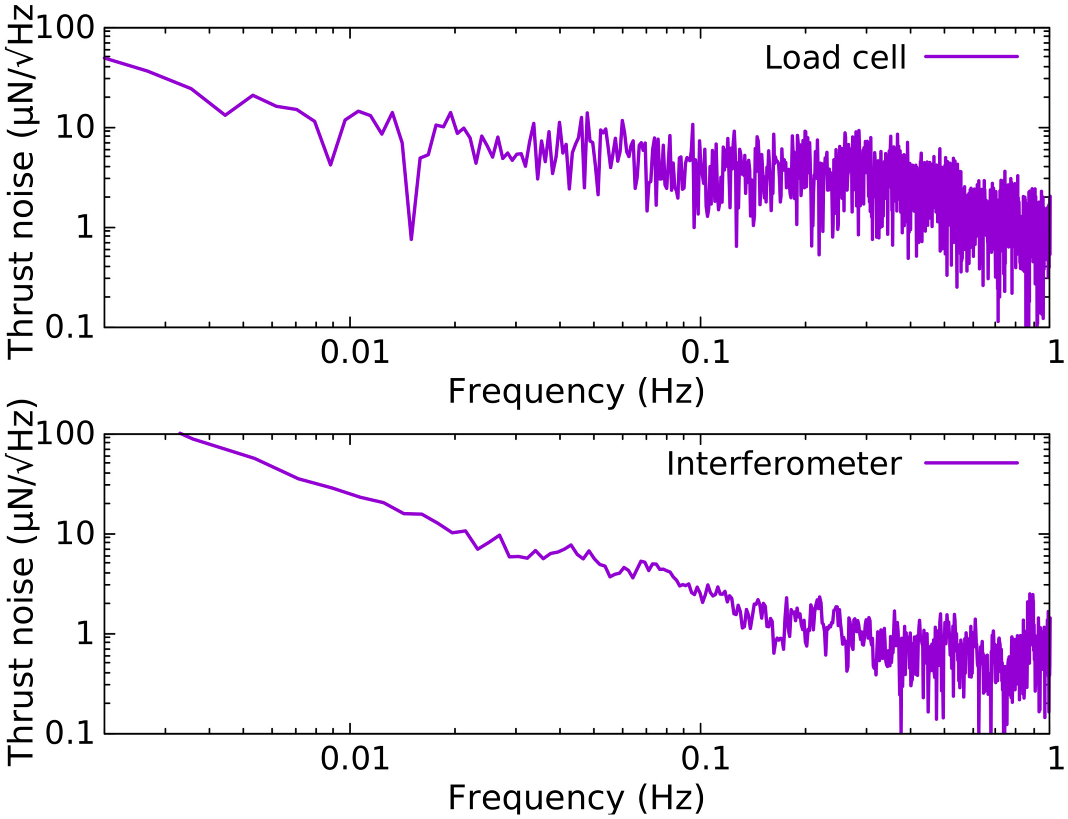

Figure 3.7: Comparison between the noise spectrum of the load cell (top plot) and the laser interferometer (bottom plot). It can be seen that the thrust noise of the load cell is generally higher than that of the interferometer except for frequencies below $\sim 0.05\,\mathrm{Hz}$, where it is comparable.

installed but with no gas flowing. In both cases, a $\sim 10\,\mathrm{min}$ period of noise was recorded, calibrated to thrust via the built in calibration mechanism and the resulting data was put through a discrete Fourier transform to obtain the thrust noise spectrum shown in figure 3.7. In this figure, the load cell spectrum (top trace) appears to be noisier than the laser interferometer obtained spectrum (bottom trace). The natural frequency of the pendulum is captured by the laser interferometer, however the magnetic damper was installed during this measurement resulting in a peak at $\sim 0.9\,\mathrm{Hz}$ that is relatively small. The natural frequency of the pendulum is not seen in the load cell spectrum as expected due to the fact that the pendulum is pressed against the load cell and is not allowed to oscillate at such a low frequency.

A $\sim 3\,\mathrm{h}$ ($\sim 10\,000\,\mathrm{s}$) thrust measuring experiment was then conducted in both systems. Each recording consisted of a calibration run (three weights of $1.17\,\mathrm{mN}$ on and off the balance) at the beginning and at the end. Between the calibration runs, the system was

Argon flow rate (SCCM)	**25**	**50**	**100**	**200**
Calculated thrust (µN)	210	415	836	1670
Interferometer thrust (µN)	205 ± 30	398 ± 30	730 ± 30	1378 ± 30
Load cell thrust (µN)	210 ± 50	402 ± 50	741 ± 50	1388 ± 50

Table 3.1: Resulting thrust from argon flow rates used in this experiment. The thrust is obtained by repeated measurements for each flow rate and the error is estimated based on the calibration, noise and repeatability of each measurement within the same campaign.

configured to automatically operate the cold gas argon thruster described earlier with a pattern of 0 SCCM, 25 SCCM, 50 SCCM, 100 SCCM, 200 SCCM and back to 0 SCCM, each step with a duration of 30 s. The resulting thrust for each flow rate is presented in table 3.1. In this table, the thrust shown is obtained by multiple measurements at each flow rate and is measured by the interferometer and the load cell. The theoretical calculated thrust of the cold gas thruster $F_{cg_{calc}}$ for an isentropic flow cold gas thruster is also presented, given by the formula$F_{cg_{calc}} = \dot{m}c_{cs}$ where $\dot{m}$ is the argon mass flow rate and $c_s = \sqrt{\frac{\gamma_{Ar} R T_s}{m_{Ar}}}$ is the argon gas sound speed (T_s is the static temperature at the exit of the tube, R=8.314 J.mol^{-1}K^{-1} is the universal gas constant, γ_{Ar} is the specific heat capacity ratio for argon and m_{Ar} is the argon molar mass). This method is also described in [41]. The agreement between the two measurement methods is very good and the overestimation of the theoretical calculation can be attributed to the boundary layer friction force described in detail in [52] which is not taken into account in the calculation.

The 30 s step duration was selected to allow the pendulum to settle for an accurate measurement of the thrust. This sequence was repeated for approximately 3 h and the resulting data is shown in figure 3.8. In this figure, the interferometer data (top green trace) appears to be drifting slowly during the measurement. This effect, known as zero drift, is likely due to temperature changes throughout the measurement. The load cell data (bottom purple trace) exhibits limited zero drift, despite not being temperature compensated. This behaviour is typical of the observations of using both systems for an extended period in the laboratory.

Figure 3.9 focuses on a few periods of the repeated measurement cycle. As expected, the laser interferometer (top green trace) exhibits less noise compared to the load cell (bottom purple trace) by roughly a factor of two. The noise behaviour is consistent in the laser interferometer and in part can be reliably traced to changes in the vicinity of the chamber, such as people walking around the laboratory (floor deformation) or

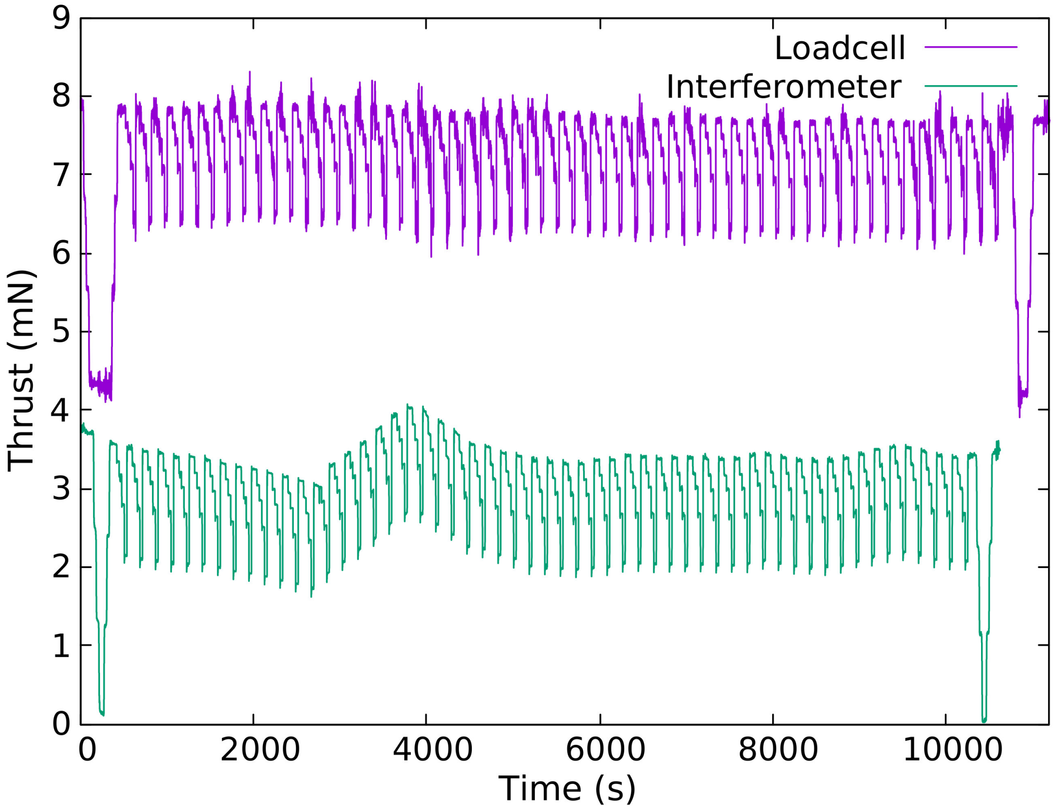

Figure 3.8: Zero drift comparison between the load cell and laser interferometer thrust measurements. In this figure a $\sim 3\,\mathrm{h}$ thruster run is shown, using the laser interferometer (bottom trace, green) and the load cell (top trace, purple). The zero thrust is in both cases at the top of each trace and the thrust for each step is the magnitude of the change from the zero value. Each measurement begins and ends with a calibration run, consisting of three 1.17 mN weights. In both cases, the thruster performs a 0-25-50-100-200-0 SCCM cycle for approximately 3 h. It can be seen that the zero drift of the load cell measurement is much less than that of the laser interferometer. The depicted behaviour is typical of the observed behaviour of both systems.

laboratory door being opened. These actions also have a measurable effect on the load cell measurement, however there are additional noise events which cannot be linked to known external factors and appear at seemingly random points throughout the recording. Such an event can be seen in figure 3.9, around t =8000 s. For a long recording, the appearance of these events does not have a detrimental effect in the accuracy of the measurement as the affected parts of the data can be easily identified and excluded from the rest of the measurement.

Figure 3.10 shows a single episode of this sudden noise. This example is typical of this type of noise and happens at a time when there is no change in the applied force on the balance. The working hypothesis on the origin of this noise is that it is the result of a *micro-slip* at the contact boundary between the load cell adjustment screw and the

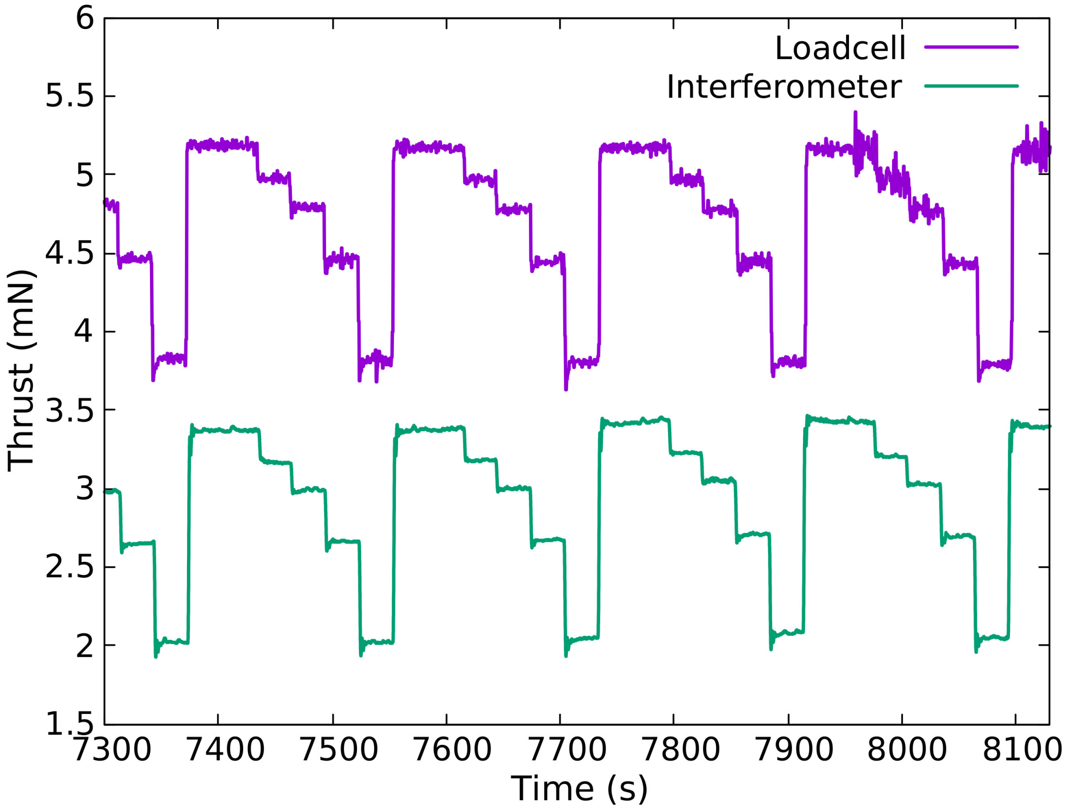

Figure 3.9: Comparison between the load cell and laser interferometer thrust measurements. This figure focuses on the data shown in figure 3.8, showing four cycles of the 0-25-50-100-200-0 SCCM cold gas argon thruster sequence. The zero thrust is in both cases at the top of each trace and the thrust for each step is the magnitude of the change from the zero value. It can be seen that the noise in the load cell measurement (top trace, purple) is higher roughly by a factor of 2 compared to the laser system (bottom trace, green). It can also be seen that the load cell can suddenly suffer increased noise (as seen in the plot around 8000 s), however this has little effect in a repeated measurement.

pendulum scale (figure 3.3). This process resembles that of an earthquake produced when the two sides of a geological fault suddenly slip laterally, commonly called a *strike-slip*.

The experiment presented in this chapter involves a cold gas thruster. In order to use this technique with other types of thrusters, the thrust balance designer needs to consider thermal and electromagnetic compatibility of the thruster and the load cell. In particular, thrusters such as plasma thrusters may produce excessive heat during operation which will affect the measurements of a non temperature compensated load cell. Any RF plasma thruster or other pulsed thruster can cause electromagnetic interference (EMI) which, if picked up by the load cell amplifier, can result in increased measurement noise. Plasma thrusters tested in a vacuum chamber can create a low-density plasma which may result in corrosion of the load cell and associated electronics. In all these cases, the thrust balance

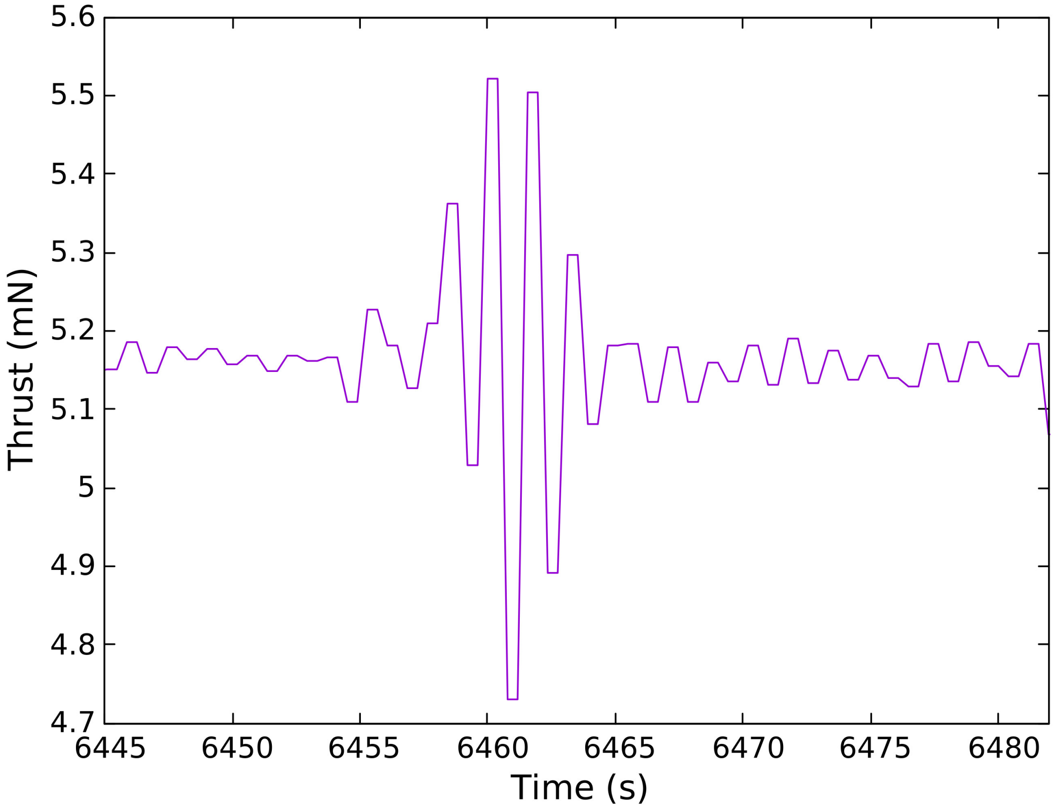

Figure 3.10: Focus on a *microslip*. This figure shows a typical sudden noise observation which happens at a time when there is no change in the forces applied to the load cell from the thruster. It is believed to be a microslip, occurring when the forces at the load cell - pendulum contact boundary are unbalanced and the net force suddenly overcomes the friction at the contact point between the load cell and the pendulum. This is a process that resembles an earthquake induced along a fault line.

designer will have to supply appropriate shielding to minimise the heat and electrical noise pickup as well as the plasma induced damage. In part, better load cell protection can be achieved by the installation of the load cell and associated electronics as far away as practical from the thruster being tested.

3.7 Summary

This chapter has presented an alternative thrust measurement system for a hanging pendulum thrust stand based on a low cost (tens of dollars) load cell. Its performance is directly compared to the more typical system of measuring the induced displacement of the pendulum by the thruster using a considerably more expensive (thousands of dollars) laser interferometer system.

While the laser system still has the advantage of lower noise by roughly a factor of two, the load cell was found to exhibit less zero drift despite not having temperature compensation. It also has a considerably lower cost compared to the interferometer, making it a viable alternative, especially for thrust measurements in the range of hundreds of micro-newtons. Another advantage is that the load cell based stand sensitivity is not as dependent on the suspended mass (weight), unlike the displacement measuring system. Alternative load cells can be utilised to modify the measurement range, if that is required. The load cell system was found to suffer from seemingly random breakouts of noise, however this is not affecting the result of a repeated measurement.

Given the encouraging results obtained from the low cost load cell, further investigation and development of this method is justified in the future. A better quality, temperature compensated load cell could yield improved resolution and less drift related to the heating resulting from the operation of the thruster. A faster ADC could provide better temporal resolution which would enable the testing of fast pulsed thrusters. Better electrical shielding could allow measurements of high power RF or other electrical discharge based thrusters.

The following chapters introduce two novel, cubesat-compatible, thruster systems and present direct thrust measurements.

Chapter 4

The inductive Pocket Rocket electrothermal plasma thruster

4.1 Motivation

This chapter presents the work associated with the development of the Inductive Pocket Rocket (IPR) electrothermal RF plasma thruster. The IPR development was based on its predecessor, the capacitively-coupled Pocket Rocket (CPR) thruster, described in detail in section 4.2. The development of the IPR is driven by the cubesat thruster designer principles described in chapter 1. More specifically, the IPR is aiming to carry out first investigation of an inductive plasma discharge, hopefully produce improved performance compared to its predecessor, and finally, solve specific engineering challenges such as the impedance matching network, both resulting in a better fit for purpose.

4.2 The capacitively-coupled Pocket Rocket

Electric propulsion has been used by satellite operators for station keeping and orbit modification since the 1960's [31]. There are many thruster designs that use plasma, such as gridded ion thrusters and Hall effect thrusters, both with a proven track record and now routinely used on commercial satellites. These systems are complex and are generally designed for larger satellites with the ability to carry a large thruster and propellant mass and use high power in the order of kilowatts to achieve their orbit modification goals. In the recent years, there has been a disruption in satellite design by the creation of the cubesat form factor unit with $10\,\mathrm{cm}\times10\,\mathrm{cm}\times10\,\mathrm{cm}$ dimensions and up to $1.33\,\mathrm{kg}$ of mass [11]. At the time of writing, the online Nanosat database [16] reports over 1,300 nanosats and cubesats that have already been placed in orbit. The majority do not

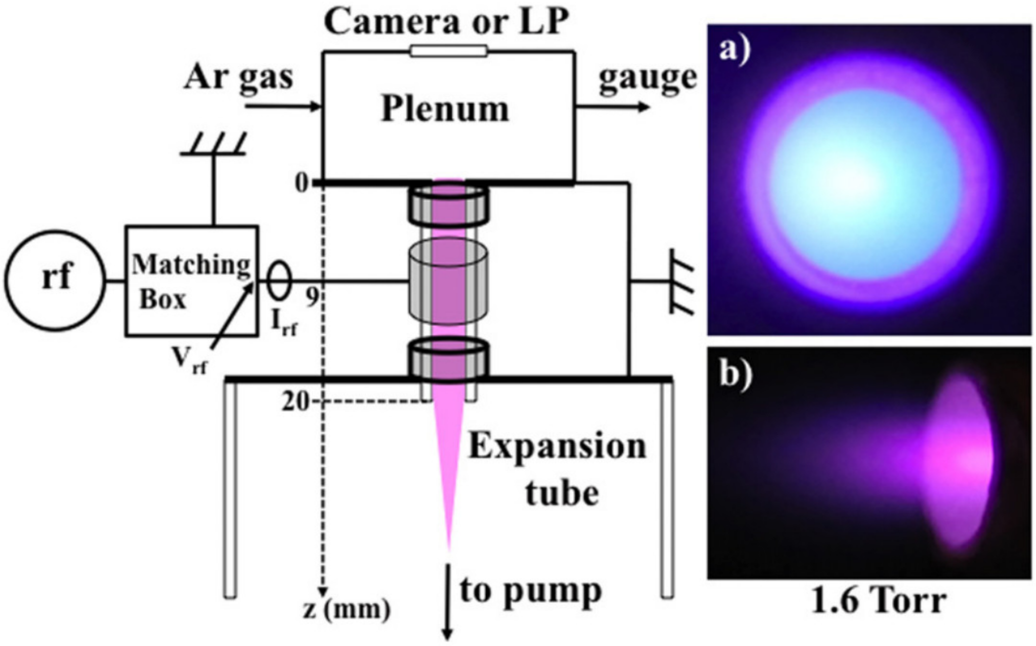

Figure 4.1: A simplified sketch of the capacitive PR taken from [79]. The CPR is shown connected to a vacuum chamber (bottom of the schematic). The RF plasma is generated in area in the middle of the discharge cylindrical cavity by applying the RF voltage on the center ring electrode. The top shows the plenum cavity which is where the propellant is introduced. The plenum has an optical window to allow observation of the plasma, seen in inset **a**. Inset **b** shows the exhaust in the expansion tube in the vacuum chamber with the CPR operating at a plenum pressure of 1.6 Torr.

have a propulsion system. There have been many proposed propulsion system designs for this type of satellite [34, 80–86] but most are laboratory designs and very little has been demonstrated or reported in *real* space missions. One reason for this is the many restrictions imposed on the thruster designer by the small satellite form factor with the most important ones being size (∼ 1/3 of the satellite volume and mass) and average power available to the payload (∼1 W).

The original Pocket Rocket was proposed in 2012 [79, 87] as a thruster candidate that suits the requirements of a propulsion system of a small satellite. It is an asymmetric, capacitively-coupled, collisional (∼ 1 Torr), 13.56 MHz RF plasma device and falls under the electrothermal thruster category, together with resistojets and arcjets [88]. It can be seen in figure 4.1, taken from original paper that described it in 2012 [79]. In this figure a schematic of the main components of the CPR can be seen. These are the plenum (top) where the propellant is introduced, the RF plasma chamber (middle), consisting of a ring electrode on which the RF voltage is applied, and the expansion chamber (bottom) which is attached to a vacuum chamber equipped with suitable vacuum pumps to ensure a realistic space environment for the experiment. The two inset photos show the plasma generated by the CPR. Inset **a** (cross-sectional view) is taken from the optical window at the back of the plenum and inset **b** is taken through the glass expansion chamber, at the exhaust end of the thruster (axial view). The thruster was operating with argon gas and the plenum pressure was about 1 Torr.

The CPR has been studied extensively to understand its properties and suitability as a small satellite thruster system. An initial description of the plume was performed by high resolution digital photography [89]. In this study, it was confirmed that the expansion plume features are consistent with previous experiments on electron density profiles within the discharge. The study was conducted using argon and nitrogen as the propellant, in low and high pressure environments. To understand better the mechanism of heating of the gas responsible for the increase of the performance when the plasma is ignited, a rovibrational band matching study was conducted [90] using spectroscopy of the nitrogen second positive system ($C^3\Pi_u \rightarrow B^3\Pi_g$) on nitrogen and nitrogen/argon mixture propellant. In this study, three mechanisms with different time constants were identified, including a fast volumetric heating process driven by ion-neutral collisions and a slower process linked to ion neutralisation and vibrational de-excitation on the walls creating wall heating. A number of computational fluid dynamic (CFD) simulations were also conducted, driven by experimentally obtained data [54, 91–93]. These studies have estimated some of the plasma parameters such as electron density, which are difficult to measure experimentally using Langmuir probes due to the small dimensions of the plasma cavity. Finally, a direct measurement of the performance of a miniaturised version of the CPR has been conducted in the Wombat space simulation chamber [40]. This study used xenon as the propellant and it confirmed the increase in thrust when the plasma is ignited compared to the cold gas operation at the same flow rate.

4.3 The inductively-coupled Pocket Rocket

The 40.68 MHz inductive Pocket Rocket (PR) described in this chapter is derived from the original capacitive design, in an attempt to improve its performance and gain further insight into the gas heating and thrust mechanism. In a capacitively coupled plasma system, energy is transferred to the electrons by the electric component of the RF field while in an inductively coupled plasma system it is the magnetic component that serves this role. The switch from a capacitive to an inductive system has potential advantages in both performance by producing an increased ion density [94] and consequently increased propellant heating, and engineering by allowing a simpler, capacitor-only, RF matching network [39].

In order to accommodate the low average power available for the generation of RF, a thruster of this type is envisaged to be operated in a low duty cycle . An example of this type of operation is a Hohmann transfer consisting of two, 1 min burns per orbit. In the typical LEO 90 min period orbit, this allows enough time to recharge the batteries between thruster operations. Using this operation scheme and the performance obtained by the inductive PR proof of concept presented in this thesis, a 2 kg cubesat in a circular 400 km orbit will gain roughly 100 m of altitude per orbit using the thruster at 100 SCCM and 50 W of RF. This is calculated in two steps by first calculating the velocity for circular orbits at the initial and final altitudes, followed by calculating the Δu of each of the two burns required, as described in [95]. The process can be repeated over a number of orbits in order to achieve the desirable altitude. In terms of power requirement to operate the thruster, two 1 min burns at 50 W RF power need 1.67 W h of energy. This energy needs to be collected from the solar panels in a period of 90 min (400 km orbit), implying a requirement of approximately 1.11 W of average power, probably closer to 1.5 W if RF amplifier and charging efficiencies are taken into account. This is within the capabilities of a 2-U satellite with extendable solar panels or larger cubesat.

The plasma coupling mode best suited to thrust generation in the capacitive PR is the Gamma mode [96] and not the very low plasma density alpha mode [97, 98]. In the Gamma mode, the electron density increases linearly with RF power and is a result of ion-induced secondary electron emission from the plasma cavity walls surrounded by the RF annulus electrode; in such capacitively coupled thruster, a self-bias generates as a result of the asymmetry between the small area powered electrode and the large area grounded walls/electrodes. The plasma thrust gain results from two terms, a bulk plasma propellant heating thrust term (resulting from ion-neutral charge exchange collisions) which immediately takes place at turn on (first hundred microseconds) and a wall propellant heating thrust term (resistojet effect) which increases with burn time as a result of ion bombardment of the radial plasma cavity walls. These two thrust terms have never been directly demonstrated and quantified experimentally. They have been indirectly deduced via gas temperature measurements [90]. Due to the small aperture area and large neutral density compared to the ion density, any thrust term from ion acceleration would remain small.

In terms of power coupling to the plasma, the inductive PR resembles the well documented low pressure ($\sim mTorr$) Helicon/inductive plasma sources and thrusters [99] which exhibit a capacitive coupling mode at low RF power and an inductive mode at higher power. For the mm size (diameter) and cm size (length) inductive PR it is necessary to operate at pressures around a few Torr to couple the plasma and the capacitive-inductive transition occurs at about 20 W. The present study focuses on the inductive mode obtained in the 20 W to 50 W power range. In terms of thrust generation, the main source of thrust expected from the inductive PR should be similar to that of the capacitive PR due to the plasma source scaling, operating pressure range and input power range of a few tens of watts. Basic thrust measurements have been previously performed for a larger inductively coupled thruster (i.e. 5 cm diameter) operating with input power ranges of a few hundred watts [100, 101] and at operating pressures of a few mTorr. It was shown that a typical power input of 100 W would result in about 1 mN of thrust, the maximum electron pressure in the plasma cavity (experimentally measured and also the result of a basic global model including particle balance and power balance, as described in chapter 10 of [94]) is converted into ion momentum along the expanding plasma as predicted by Fruchtman [102]. Fruchtman [103] also discussed the complexity of thrust imparted by low pressure and high pressure expanding plasma sources. For capacitive PR, the basic understanding of the plasma-generated thrust increase at 13.56 MHz from the cold gas thrust has been validated using CFD Ace+ [52] and HEMP fluid-plasma transient simulations [100].

The present study demonstrates the direct thrust measurement of a millimetre sized inductively coupled plasma source using a vacuum compatible miniaturised impedance matching system at 40.68 MHz. Since this is simply a proof of concept, it is premature to directly compare with other technologies. Instead, additional reference cases are of a cold gas system and of a filament heated resistojet system are provided, as well as some comparative discussion with larger low pressure inductively coupled thruster.

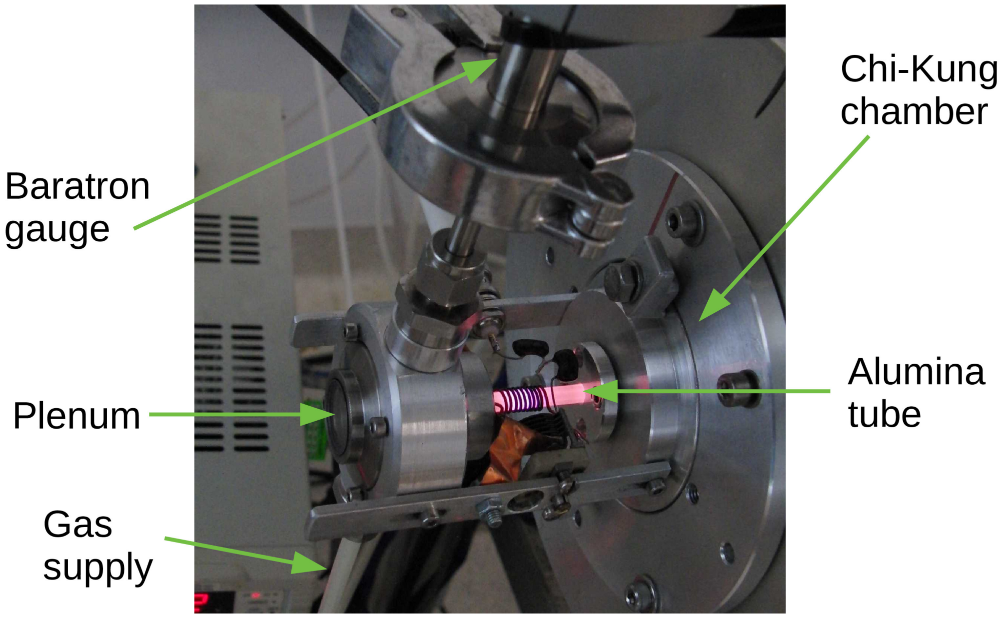

Figure 4.2: Photo of the inductive PR (center left) connected to the Chi-Kung vacuum chamber (right). The Baratron vacuum gauge is connected to the top of the plenum and the gas supply to the bottom. The inductive PR is operating with argon at 100 SCCM and 30 W of RF power at 40.68 MHz. Part of the RF matching network is also visible, in this instance consisting of silver mica capacitors and a variable capacitor which was used for fine tuning.

4.3.1 Physical description

Two experimental configurations are used to develop and characterise the IPR: a first configuration where the prototype is directly mounted onto a small size vacuum chamber (*Chi-Kung*) and a second configuration where the prototype is immersed in a much larger vacuum chamber (*Wombat*). Both chambers have been described in chapter 2.

First experimental configuration

A photo of the inductive PR mounted onto the previously described Chi-Kung vacuum chamber [104] is shown in figure 4.2 and a simplified schematic is shown in figure 4.3. The inductive PR consists of a plenum (a grounded cylindrical cavity into which gas is introduced) contiguously connected to a 5.5 mm outer diameter and 4.0 mm inner diameter ceramic (alumina) tube which forms the plasma cavity. The length of the alumina tube is approximately 6 cm. The ceramic tube is surrounded by a multiple turn RF loop antenna. The plenum (left exit of the plasma cavity on figure 4.2) is made with aluminium and has a cylindrical shape with 25 mm diameter and 15 mm depth resulting in $\sim$7 cm^3 of volume. Viton o-rings are used to ensure a good vacuum seal between the ceramic and the aluminium. The o-rings are compressed with aluminium clamps which are tightened in place with screws. The exhaust end of the ceramic tube is connected via an appropriate aluminium flange to the 30 cm long 15 cm diameter pyrex tube of the Chi-Kung vacuum system, simulating the vacuum conditions of space.

Gas is injected to the plenum via a quarter-inch flexible hose (figure 4.2). For the Chi-Kung testing configuration, an MKS 626B Baratron pressure sensor is connected to the plenum via a short, rigid quarter-inch pipe and KF25 vacuum fittings in order to provide pressure measurements with the plasma *off* or *on*, a parameter previously identified as a measure of neutral gas heating [96, 105]. The gas supply consists of a centrally located argon cylinder at high pressure, a ∼60 PSI regulator and an MKS Type 247 display and MKS Mass Flo gas flow controller which allows an accurate selection of gas flow up to 140 SCCM. The plenum pressure varies with the cold gas flow rate from a fraction of a Torr at a few SCCM of gas flow to ∼3 Torr, at 140 SCCM. The Chi-Kung expansion chamber is pumped by a rotary vacuum pump and a secondary turbomolecular pump. The vacuum base pressure in the chamber is typically $\sim 8 \times 10^{-4}$ Torr when the gas supply is off and rises up to $\sim 10^{-2}$ Torr with the gas supply at the maximum setting of 140 SCCM. The pressure in the plenum and plasma cavity is greater by a factor of 100 to that in the vacuum chamber, ensuring the system is operating in choked flow conditions [52, 54]. This is checked by confirming that the plenum pressure is not affected by the downstream pressure.

A 10-turn, 1 mm diameter, ∼15 mm long along the thruster main axis, copper wire inductor forming the RF antenna is wound on the ceramic tube as seen in figure 4.3. It is not in contact with the plasma making this system an electrodeless thruster. The plenum end of the inductor is grounded and the exhaust end is connected to the RF matching circuit (described in detail in the impedance matching section below). The matching circuit matches the inductive load formed by the antenna and the plasma system to 50 Ω to allow easy connection via any length 50 Ω coaxial cable to a laboratory grade wideband RF amplifier (Mini Circuits ZHL-100W-GAN+). The amplifier is driven by a 40.68 MHz sine wave signal from a Keysight 33600A arbitrary waveform generator which is used to control the output power and, when pulsed, the duty cycle of the RF supplied to the thruster (a feature not used in the present study). The RF circuit also includes a cross-needle Daiwa CN-801 SWR meter which is used to confirm power and matching quality. A high-flow cooling fan can be used to cool the inductor to ensure the Viton o-rings do not

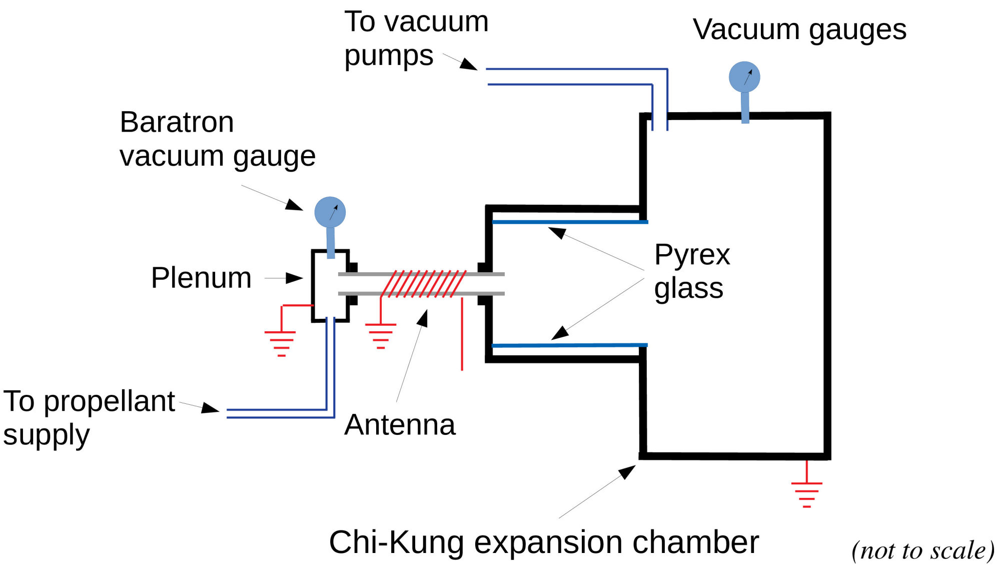

Figure 4.3: A simplified sketch of the inductive PR, shown here connected to the Chi-Kung expansion chamber at lower pressure (as seen in figure 4.2). The Pyrex glass inside the chamber is part of a different experiment also run on Chi-Kung and bears no significance in the experiments described in this chapter.

overheat when operated at high power and for long duration. With the cooling supplied from the external fan, the prototype can run continuously at 40 W reaching a maximum temperature near the centre of the coil not exceeding 200 °C. In these conditions, thermal equilibrium is achieved within a minute of RF being switched on. The inductive PR Chi-Kung setup can be used not only to test and optimise the RF circuitry but also the RF power transfer into the plasma by allowing plenum pressure measurements.

Second experimental configuration

The main aim of the IPR study is to demonstrate thrust gain from gas heating during plasma operation with the newly designed 40.68 MHz compact impedance matching system. To this effect a second configuration is used where the inductive PR with matching network is attached to a thrust balance and fully immersed within the previously described, larger Wombat vacuum chamber [39, 40]. Major components of this assembly are shown in figure 4.4; a photo of the prototype operating in the Wombat chamber is shown in figure 4.6. In this set up the RF antenna is located at a distance of $\sim$ 8 mm from the exhaust plane of the plasma cavity. The length of the ceramic tube is reduced to a length of $\sim$ 4 cm compared to the Chi-Kung setup. Similar measurements have

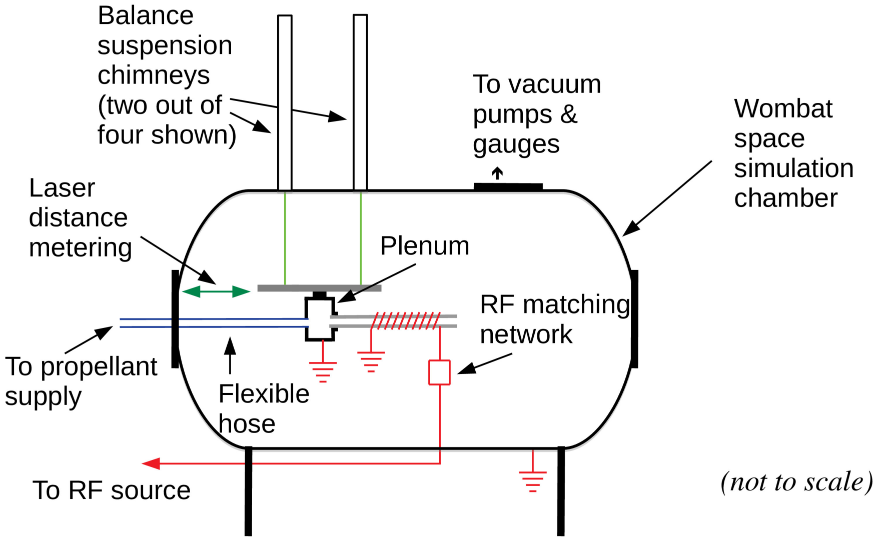

Figure 4.4: A simplified sketch of the inductive PR, shown here installed in the Wombat vacuum chamber equipped with a thrust balance.

been conducted in this chamber in the past for the capacitive PR mounted on the large, four-arm, thrust balance [40]. Here essential improvements to the thrust measurement procedure have been carried out as follows: the propellant is supplied via a flexible PTFE hose with an outer diameter of 1.5 mm and inner diameter of 0.8 mm, and RF power is supplied via a flexible RF cable (RG316). Both lines are attached to suitable vacuum feed through connectors to allow connection with the gas controller (Alicat scientific) and RF power supply (Oregon Physics VRG1000A), both located outside the chamber.

Care has been taken to ensure both gas line and RF cable are mounted in a way that is not influencing the measurements. The lack of influence in the displacement from the gas line and RF cable was confirmed by the repeatability of the results in a large number of cold gas operations and by the observation that there is no significant displacement change when RF was switched on with no gas. An extreme case of the latter can be seen in figure 4.5. In this figure, the RF amplifier is set up for 40 W output and is switched between t =0 s and t =10 s. A deviation of about 50 µN is observed in the thrust measurement. Because the gas is switched off, the load at the end of the coaxial cable is very far from 50 Ω resulting in a big mismatch. The effects of an impedance mismatch have been discussed in chapter 2. As a result of this mismatch, about 60 % of the power is absorbed mostly by the cable and the remaining 40 % is reported by the amplifier as reflected power. The deformation of the coaxial cable resulting from the deposited heat is responsible for the exaggerated thrust excursion. When making thrust

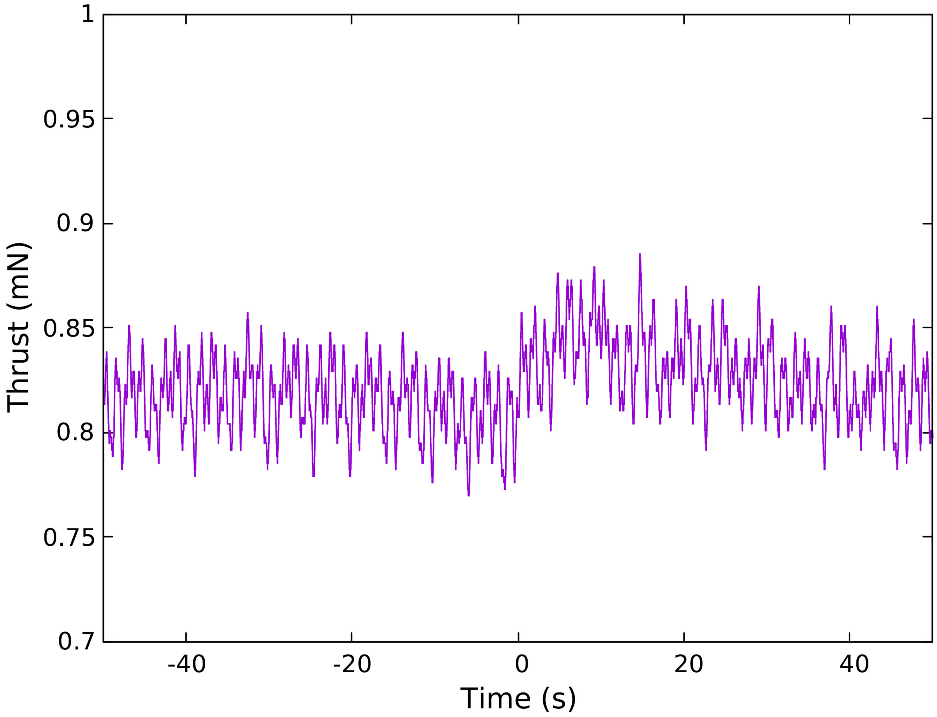

Figure 4.5: A plot of the effect of the heating of the cable in a thrust measurement. In this example, the RF amplifier is set for 40 W output and is switched between $t = 0$ s and $t = 10$ s. A deviation of about 50 µN is observed in the thrust measurement due to the heat deposited in the cable because of the impedance mismatch.

measurements, the gas is on and the impedance mismatch is very small, resulting very little heat dumped on the cable and an excursion of significantly smaller amplitude than 50 µN.

When the thruster operates, either in cold gas or plasma mode, the balance moves in reaction to the applied force and the displacement D is measured with a previously described laser-sensor system in chapter 3 and in [40]. This system is based on a laser triangulation displacement sensor (ILD1700) and has a resolution of 0.1 μm. The thrust to displacement calibration factor is 0.044 mN µm^{-1} and is obtained by using a calibration system consisting of a set of well known weights on a string connected via a pulley to the balance. The application of the weights is controlled by a stepper motor, installed in the chamber. Vacuum in the chamber is produced by three pumps: a Neovac SS120W roughing pump achieves $\sim 10^{-2}$ Torr with no gas flow and a large Varian V1800A turbomolecular pump with a pumping speed of 1600 L s^{-1} (N_2) improves the vacuum to $\sim 10^{-6}$ Torr. A cryopump is also available but was not used in these measurements.

To avoid putting the balance in an undamped oscillation every time there is a thrust

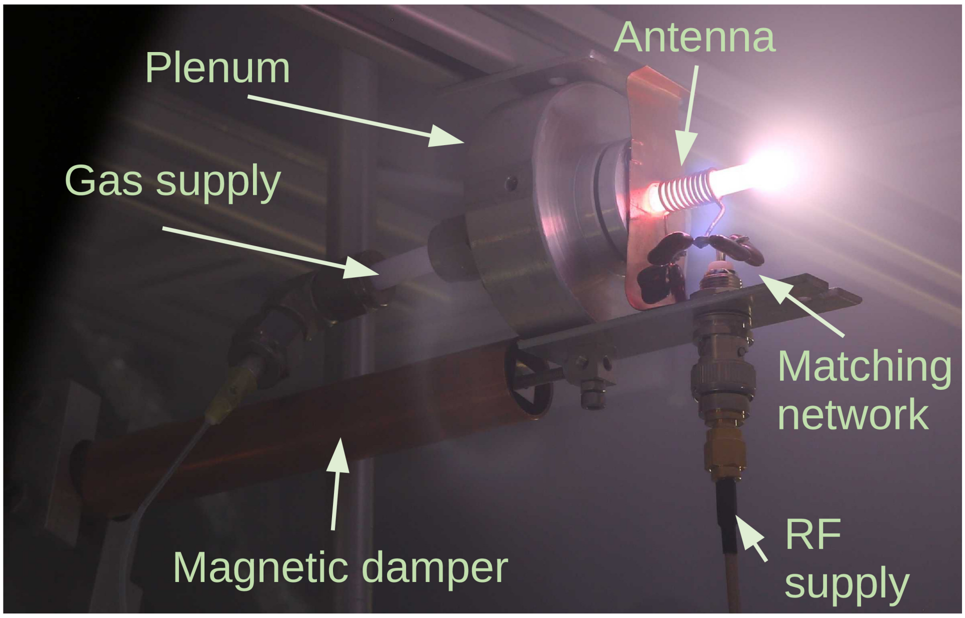

Figure 4.6: Photo of the inductive PR mounted on the thrust balance and shown operating inside the Wombat chamber. The magnetic damper consisting of a copper tube attached to the chamber and a set of permanent magnets attached to the thruster can be seen below the thruster, to the left hand side. The RF matching network can also be seen, in this instance consisting of fixed value silver mica capacitors only.

change or external stimulus (mechanical vibration) and to quickly return to a baseline position, a custom-made magnetic damper is installed. The damper, seen in figure 4.6, uses permanent magnets attached to the balance and inserted into a copper tube which is attached to the chamber. The eddy currents produced in the copper by the movement of the magnets result in a force opposing the movement and as a result have a damping effect. The time constant of this damping mechanism is in the order of a few seconds. This damping effect is further augmented by a moving average filtering done at the raw data level resulting in an improved sensitivity system. The collective effect of the magnetic damper and the moving average filtering can be seen in figure 3.5. The thrust measurement campaign aims at assessing the cold gas thrust and the thrust gain when the plasma is turned on for varying gas flow rate and varying RF power. There is presently no cooling system and plasma runs (burns) are kept to a minute or less to avoid overheating damage to the Viton o-ring. No thermal drift of the balance was observed due to the short plasma burns.

4.3.2 The IPR RF subsystem description

Frequency selection

The selection of frequency of operation for the inductive PR is based on two distinct requirements. The first one is the requirement to operate on a frequency that is not likely to cause interference to any other user of the radio spectrum. This requirement must be satisfied for all areas the satellite will be flying over, as determined by its orbit. The second one is to select a frequency which provides optimal performance of the thruster and is compatible with the cubesat architecture restrictions stated earlier in this chapter.

To facilitate the operation of RF systems of Industrial, Scientific and Medical (ISM) nature (such as the cubesat thruster), the International Telecommunications Union (ITU) has determined a number of bands which are agreed by all member states to be used for such applications in a global scale. These bands are listed in the 2016 edition of the ITU Radio Regulations document (footnote 5.150) and are 13.56 MHz, 27.12 MHz and 40.68 MHz in the HF/VHF part of the spectrum, followed by 2.4 GHz, 5.8 GHz and 24 GHz in the microwave part of the spectrum. There are other bands between VHF and microwaves allocated for similar applications by local administrations in many countries, however they do not enjoy the same global recognition as the ISM bands do. The technology to build suitable RF sources for the three lower ISM bands has been demonstrated and includes novel amplifier designs such as the Class-E [44]. Class-E amplifiers for the HF/VHF part of the spectrum have been constructed with 90% efficiency or better [45, 106]. A Class-E amplifier designed to match the IPR is described in chapter 5. While the inductive PR thruster could in theory be designed to be powered by a microwave source, the strict restrictions of the cubesat platform make this choice a more challenging one due to generally lower efficiency achievable on these frequencies. A typical efficiency value of high-efficiency RF sources for 2.4 GHz systems is $\sim 50\%$ which indicates not only a higher input power requirement for a given RF output power, but also an exacerbated semiconductor heat dissipation problem.

In order to select one of the three lower ISM bands, it is important to explore the impedance characteristics of an inductively coupled plasma device like the inductive PR. The impedance Z at the antenna with the plasma ignited can be represented as

$$Z = (R_p + R_l) + \omega L i$$

where R_p is the resistive component of the plasma impedance, R_l represents the loss, dominated by the ohmic loss from the RF current flowing on the antenna (also called *vacuum resistance*, R_{vac}) and ωL is the inductive reactance of the antenna. The angular frequency, ω, relates to the RF frequency, f, according to the formula $\omega = 2\pi f$. The inductance, L, is mostly dependent on the antenna length, diameter and number of turns. The R_p component of the impedance is due to the plasma absorbing energy and is not dependent on frequency. The power deposited in the plasma is $P_p = I^2 R_p$ where I is the antenna current. For a given current (or plasma deposited power), the voltage across the antenna V_{ant} is determined by the reactance and not the resistance as, for the typical inductive PR operating conditions, $R \ll \omega L$ and is $V_{ant} \approx \omega L I$. The higher voltage offered by the higher frequency is an important advantage to consider in the thruster design as it facilitates a quicker and more predictable striking of the plasma. R_l represents the loss component and is mostly due to the skin effect influenced AC resistance of the copper wire. In the case of the inductive PR, $R_l \ll R_p$ for all three ISM bands. Typical values at room temperature for the highest frequency of 40.68 MHz and copper conductors are $R_l =\sim 0.1\Omega$ and $R_p =\sim 3.1\Omega$. R_l increases with frequency but $R_l \ll R_p$ still holds at the expected operating frequencies of the prototype. The losses can be further improved by using silver plated conductors instead of copper. Based on the above the frequency of operation chosen for the present development of the prototype is the ISM band of 40.68 MHz, a change from the 13.56 MHz previously used for the capacitive PR [79].

Impedance matching network

The plasma producing inductor appears as an impedance of $\sim(3.2 + 56\mathrm{i})\,\Omega$ (at 40.68 MHz), obtained by direct voltage and current measurements and calculations based on the matching network component values. Small variations in this impedance may be observed and are due to parasitic impedances in the space immediately around the inductor as well as the gas flow rate and copper temperature, with the last two affecting the real part of the impedance. There are multiple circuits that will match the ignited plasma impedance to $50\,\Omega$ (the output impedance of commercial RF sources used in the laboratory) consisting of inductors and capacitors. In general, inductors introduce added losses due to ohmic heating, can be affected by objects in their surrounding and take more space. While innovative solutions for manufacturing inductors have been proposed [107], a capacitor-only matching network is preferred if possible [39]. The two simplest

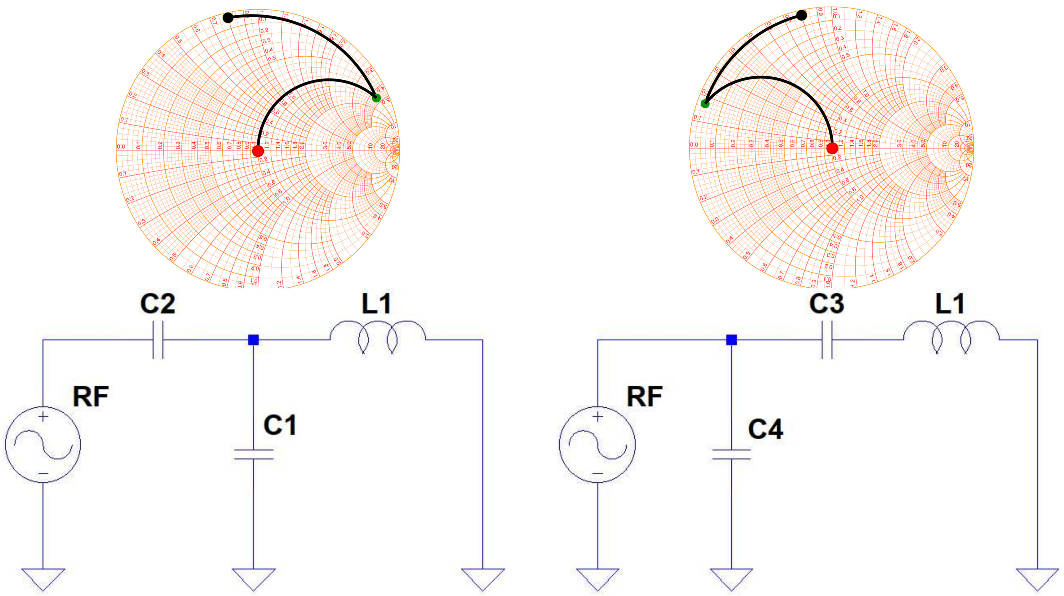

Figure 4.7: Two capacitor-only matching networks that are suitable for the inductive PR impedance matching system. L1 indicates the plasma antenna, shown in figure 4.2 and 4.3. The Smith charts on top of each circuit show the starting point (black point representing the impedance at the antenna), the intermediate step (green point, which is the impedance after C1/C3 is added to L1) and the final destination (red point, after the complete matching network) which is the desired 50 Ω.

capacitor-only impedance matching networks are shown in figure 4.7, together with the Smith chart solutions.

Out of these two matching circuits, the one using C1/C2 was selected because it results in lower value capacitors which are generally easier to obtain with very low or zero temperature coefficient (C0G/NP0 types). In the prototype C1 is implemented with a fixed capacitor network resulting in a total capacitance of ∼53 pF and C2 is a fixed ∼18 pF capacitor. Another advantage of the C1/C2 matching circuit over the C3/C4 one is avoiding the relatively high current that will flow on C4.

Before plasma ignition, the matching network does not provide a good match to 50 Ω due to the lack of the plasma resistance. In this case, circuit simulations show that there is a higher current I flowing on the inductor, which results in a higher voltage V across it. This is beneficial for the successful ignition of the plasma. If the RF power is decreased below the design range of 20 W to 50 W, the plasma switches to a capacitive mode. This is visually observed from the brightness of the plasma being asymmetric and much brighter at the 'hot' (not grounded) end of the inductor. If the power is increased to the design range, the discharge becomes inductively coupled and the brightest spot moves to the centre of the coil. The voltage across the inductor is ~250 V peak for 40 W RF power.

It is convenient to have a 50 Ω system in the laboratory. However, this is not a requirement for the final design that will operate on a cubesat. In this case, the amplifier can be designed with an output impedance of 3.2 Ω and the matching network can be reduced to a single capacitor with enough capacitive reactance to tune out the 56i Ω inductive reactance of the load for maximum power transfer. The impedance was found not to vary significantly when the thruster is operated within its design range of power (20 W to 50 W) and argon gas flow (20 SCCM to 100 SCCM). At 40.68 MHz, this results in a ~70 pF capacitor. Such direct impedance match has been successfully demonstrated for capacitive PR [106].

4.3.3 Direct thrust measurements: Cold gas thrust

In an electrothermal RF plasma thruster the total thrust (F_T) consists of two main components, the cold gas thrust (F_{cg}) and the additional plasma thrust (F_p):

$$F_T = F_{cg} + F_p$$

Figure 4.8 shows the raw displacement D (from the thrust balance laser-sensor system) over time in cold gas operation for increasing argon flow rate (0 SCCM to 200 SCCM in 20 SCCM incremental steps) and decreasing flow rate (200 SCCM to 0 SCCM in 50 SCCM incremental steps). Each step is ~20 s long. The data sampling rate is 312.5 Hz with a moving average of 256 applied. The data is then reduced by taking the mean every 16 measurements. The result is a measurement clear of frequencies >1 Hz which are most likely noise. This measurement was repeated 4 times to obtain the F_{cg} results shown by green crosses on figure 4.9.

Plenum pressure P_{plenum}, shown in the figure as blue stars, varies from 0 Torr to ~3 Torr when the argon flow rate increases from 0 SCCM to 200 SCCM.

On first approximation, neglecting the neutral gas pressure term, the axial thrust force generated by the cold gas can be approximated for an isentropic choked flow regime by the momentum term $F_{cg_{calc}}$ [105] given by:

$$F_{cg_{calc}} = \dot{m} c_{cs}$$

where $\dot{m}$ is the argon mass flow rate and $c_s = \sqrt{\frac{\gamma_{Ar} R T_s}{m_{Ar}}}$ is the argon gas sound speed (T_s is the static temperature at the exit of the tube, R=8.314 J.mol^{-1}K^{-1} is the universal

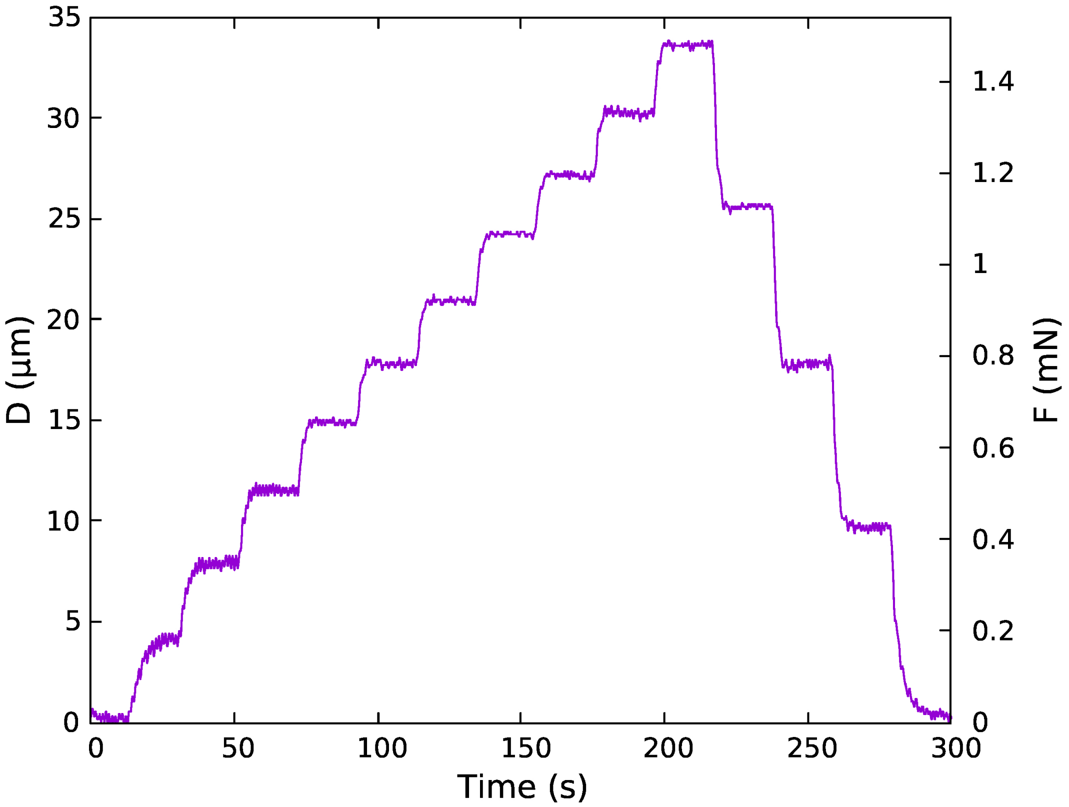

Figure 4.8: Raw data from thrust balance showing balance displacement D over time. In this sequence, the thruster was operated with cold gas starting at 0 SCCM to 200 SCCM in steps of 20 SCCM, then return back to 0 SCCM in steps of 50 SCCM. Each step lasts for 20 s. The data sampling rate is 312.5 Hz with a moving average of 256 applied. It is then reduced by taking the mean of every 16 measurements. The basic calibration is measured to be approximately 0.044 mN µm^{-1}.

gas constant, γ_{Ar} is the specific heat capacity ratio for argon and m_{Ar} is the argon molar mass). At T_{total} ∼300 K, T_s given by the formula $T_s = \frac{T_{total}}{1+\frac{\gamma-1}{2}M^2}$ is about 225 K, c_s is about 279.2 m s^{-1} and the calculated $F_{cg_{calc}}$ shown by the purple solid line on figure 4.9 increases up to ∼1.7 mN for 200 SCCM of argon. Agreement between $F_{cg_{calc}}$ and $F_{cg_{meas}}$ is very good at flow rates below ∼80 SCCM giving confidence that the experimental system is appropriate. The measured thrust $F_{cg_{meas}}$ is somewhat lower than the calculated thrust at high flow which indicates that some unaccounted loss is occurring in the system. This loss is likely due to the boundary layer friction force acting upon the inner wall of the ceramic tube, as described in detail by Ho [52].

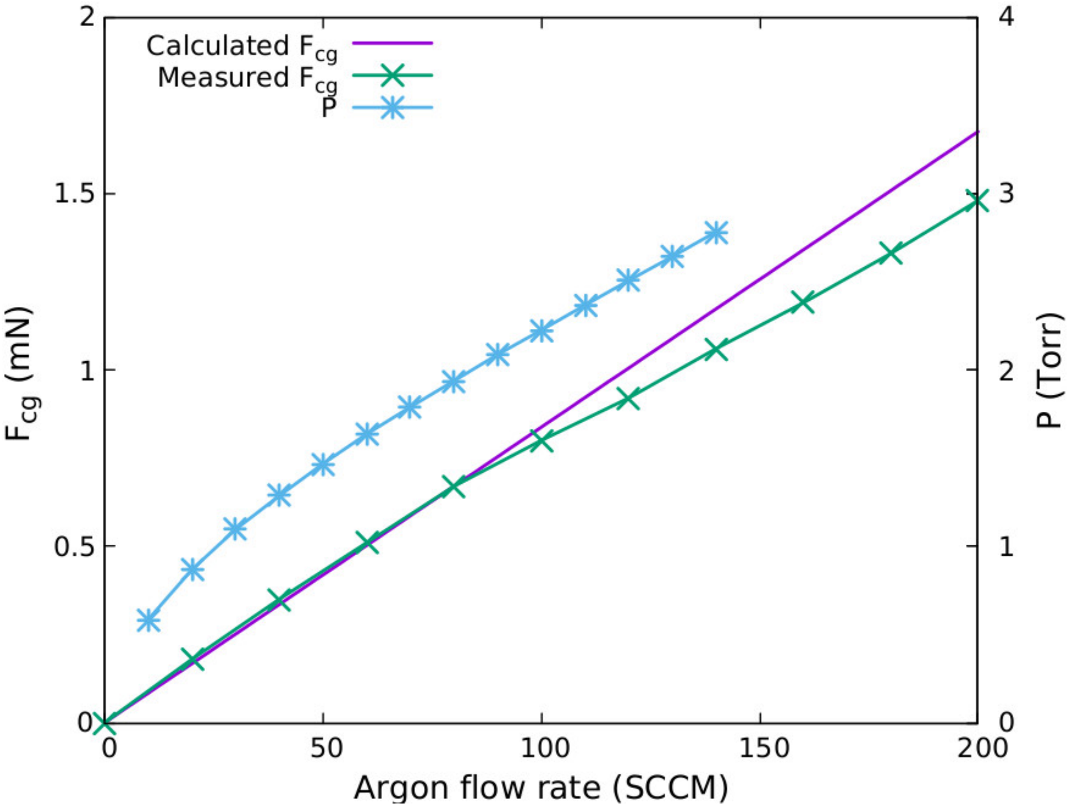

Figure 4.9: Calculated cold gas thrust F_{cg} (solid purple line), measured thrust F_{cg} (green crosses) in the Wombat chamber (figure 4.4) and plenum pressure P_{plenum} (blue stars) measured in the Chi-Kung chamber (figure 4.3), versus argon flow rate.

4.3.4 Direct thrust measurements: Plasma thrust

The next step in the characterisation of the inductive PR is the measurement of the thrust increase F_p when the plasma is ignited (as shown in figure 4.6). For the thrust measurement procedure, the prototype is fed with a constant gas flow rate, the balance is allowed a few seconds to settle and the RF is subsequently switched on. A typical measurement of the balance displacement D at plasma ignition and thereafter is shown by a solid purple line in figure 4.10. D exhibits a rapid increase due to the volumetric gas heating directly by the RF power, followed by a slower increase due to the ceramic wall heating up via ion bombardment and exchanging heat with the propellant as described in detail in [90]. In this figure the effect of the magnetic damper can be observed with the ~ 2 s period oscillations in the displacement being damped effectively within a few seconds.

A useful qualitative diagnostic indicative of thrust from the plasma is the plenum pressure P_{plenum}, measured with the inductive PR mounted onto the Chi-Kung chamber

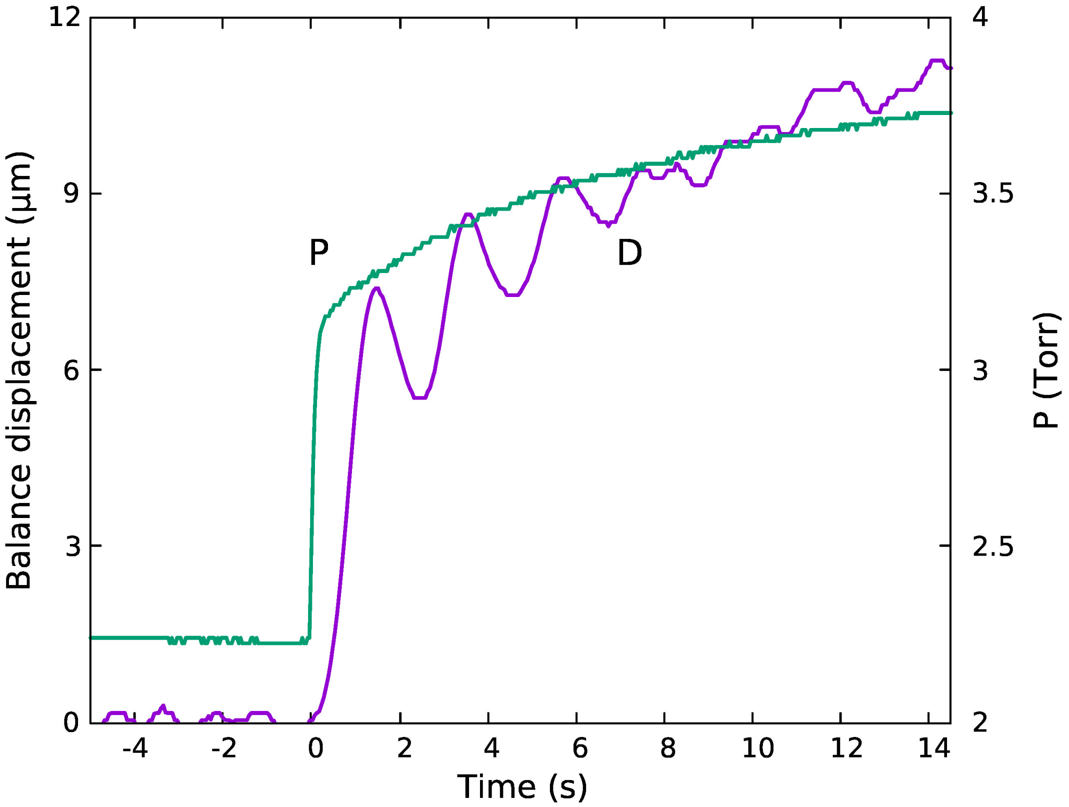

Figure 4.10: Balance displacement D (solid purple line) measured in the Wombat chamber and plenum pressure P_{plenum} (solid green line) measured in the Chi-Kung chamber, over time for 100 SCCM of argon and 50 W of RF. The RF is switched on at t =0 s. The RF current flowing on the antenna when the RF is switched on is ∼4 A RMS.

(first configuration), and shown by the solid green line on figure 4.10 for the same flow rate and RF power. The displacement and plenum pressure plots are synchronised to the time the RF is switched on ($t = 0$ s). The variation in P_{plenum} versus time strongly matches that of the balance displacement. The thrust increase due to the wall heating up can be compared to the resistojet thruster principle and it is found to be a function of gas flow rate, RF power and heat dissipation mechanism. For the present study we only focus on plasma thrust gain at plasma ignition versus the two main parameters, RF power and argon gas flow rate.

The effect of RF power in the plasma thrust (F_p) for a fixed 100 SCCM argon flow rate is presented in figure 4.11. The data points in this plot are the average of 8 measurements of 20 s burns for each power and the error bars reflect the distribution of these measurements. The reported thrust does not include the slow resistojet increase which can be seen in figure 4.10. F_p increases quasi-linearly from 0.14 mN at 20 W to 0.3 mN at 50 W. Since the pressure is of the order of one Torr in the plasma cavity (same as capacitive

PR), it is expected that the source of thrust will be mostly from heated neutrals [96]. Previous thrust measurements have been reported for inductive RF sources [100]: for a 6.5 cm diameter, 9.5 cm long plasma cavity in which the operating pressure was of the order of a mTorr (∼55 SCCM of argon), the source of thrust was shown to be mostly a result of the maximum electron pressure converted into ion momentum and about 0.5 mN at 100 W.

It is of interest to carry out a basic estimate of the thrust from ions for the millimetre scale IPR inductive RF source for comparison. This was done using a global plasma model (comprising a particle balance and power balance) described in detail by Lieberman and Lichtenberg [94] and previously applied to low pressure RF sources [99] to determine a maximum electron density subsequently used in a plasma thrust model described in detail by Fruchtman [102], and successfully applied to inductively coupled RF thrusters [78, 100]. In the latter, ion-neutral collisions are ignored and the thrust from accelerated ions is given by the maximum electron pressure within the plasma source region, $F_{ion} = qn_eAT_e$, where q is the electron charge magnitude, n_e is the maximum radially averaged density within the source region, A is the cross-sectional area of the source tube, and T_e is the electron temperature in eV units. A thrust reduction factor of 0.6 [100] to 0.82 [78] to account for the radial density profile in a cylindrical source is typically used.

A particle balance for a cylindrical plasma which consists in equating the total surface particle loss to the total ionisation [94, 99] was initially carried out to determine the electron temperature (assuming a Maxwellian distribution) and the ion Bohm velocity: ignoring the presence of the plenum cavity and using a plasma cavity radius of 2 mm and length of 15 mm, approximately corresponding to the antenna footprint shown in figure 4.6, and a mid-cavity pressure of 1.1 Torr corresponding to half the plenum pressure measured for 100 SCCM gas flow (figure 4.10), the electron temperature is about 2.0 eV and the Bohm velocity $u_B = 2.2 \times 10^3\,\mathrm{m\,s^{-1}}$. The input gas temperature was assumed to be 300 K in first approximation. Such procedure was also carried out in the capacitive PR as described in [79] yielding similar output due to the similar geometry and operating gas pressure. These capacitive PR results were later confirmed with direct electrostatic probe measurements and computer simulations[54, 108].

Based on the derivation of the electron temperature with the particle balance, a power balance was subsequently used to estimate the maximum plasma density ($n_{e_{max}} = n_{i_{max}}$) as described in [94, 99, 100] and determine the thrust from the electron pressure n_eT_e

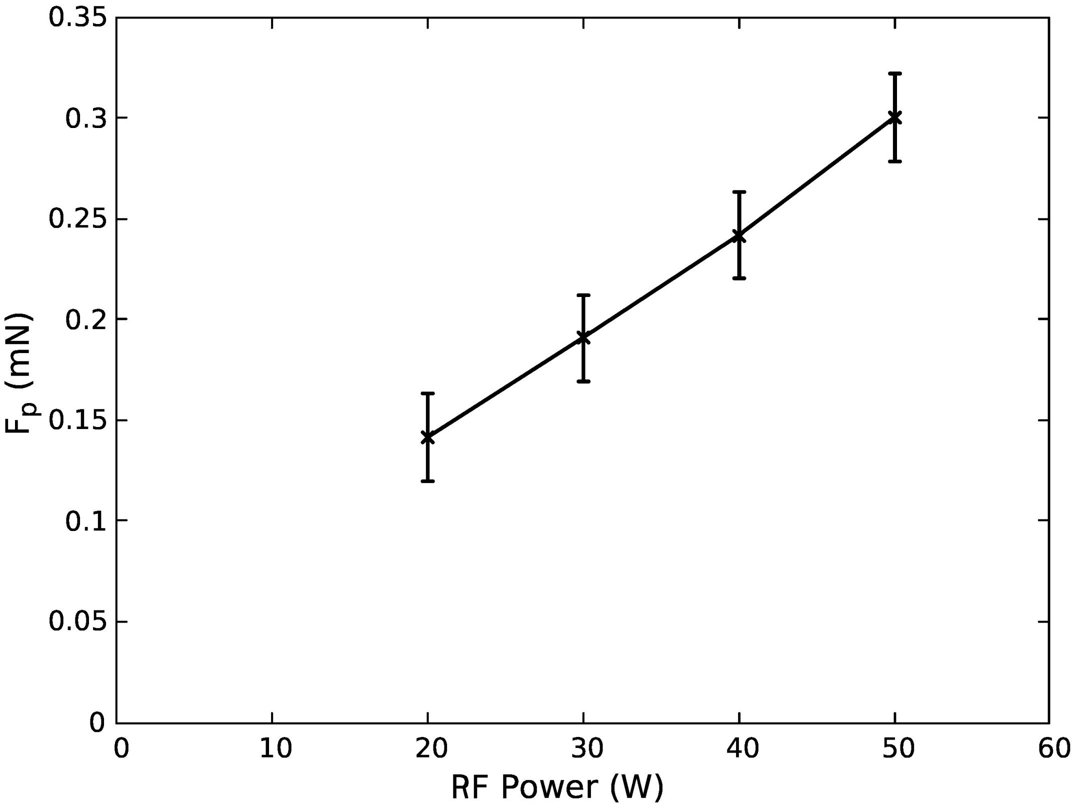

Figure 4.11: Plasma thrust F_p versus absorbed RF power for fixed 100 SCCM argon flow (solid line, crosses). The reported thrust in this plot does not include the cold gas F_{cg} component which is ~0.8 mN, as seen in figure 4.9.

(which is converted into axial ion momentum as previously detailed in [100] and [102], here a thrust factor of 0.6 is used for the radially averaged plasma density, i.e. $n_e = 0.6 n_{e_{max}}$). An approximate power input reduction factor of 0.9 was used to account for the electrical power transfer inefficiency of the matching circuit. This model yields a thrust from ions of 25 µN at 20 W to 63 µN at 50 W of RF power which is between 18% (at 20 W) and 21% (at 50 W) of the measured values. These values are significantly lower than the respective measured thrust values shown in figure 4.11 (140 µN and 300 µN for 20 W and 50 W, respectively). This is an indication that like its predecessor the capacitive PR, the inductive PR behaves like an electrothermal thruster (thrust gain from heated neutrals) rather than a ‘plasma or ion’ thruster when operated in the configuration of geometry, power and gas flow rate described in this chapter.

Having confirmed that the main thrust generation mechanism is neutral gas heating (rapid increase reported in figure 4.11 due to the volumetric gas heating directly by the RF power), followed by a slower increase due to the ceramic wall heating up via ion

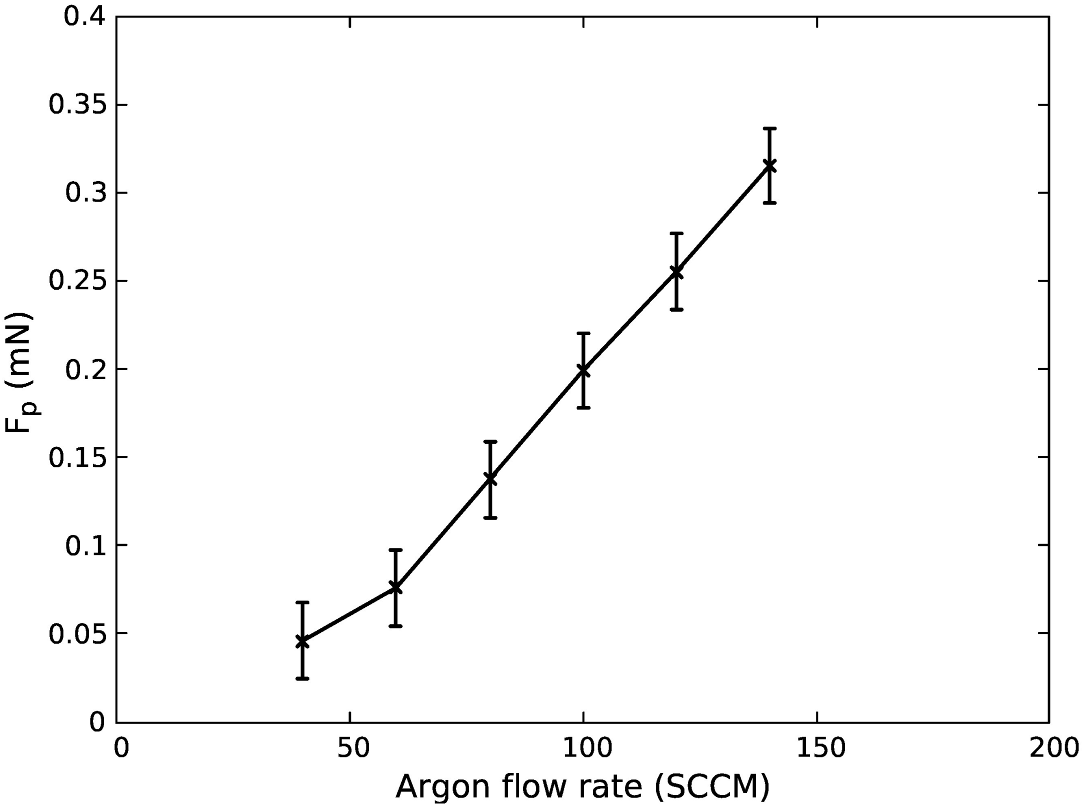

Figure 4.12: Plasma thrust F_p versus flow rate for fixed 30 W RF power. The reported thrust in this plot is the thrust due to the RF and does not include the cold gas component.

bombardment and shown in figure 4.10, the variation in thrust from the ions was investigated as a function of the gas temperature since we initially assumed a gas temperature of 300 K. Assuming a gas temperature increase of a factor of 2 from 300 K to 600 K for 20 W power input gives an electron temperature of 2.3 eV and an ion thrust of 19 µN (down from 25 µN). This simple estimate shows the interplay between thrust generation from heating neutrals and accelerated ions. Global models provide no spatial information and should be complemented by future dedicated computer simulations for further investigation.

Figure 4.12 shows the effect in F_p of flow rate change when keeping the RF power constant. The knee point seen at about 60 SCCM in this plot is likely to be related to the physical dimensions of the tube and will be the topic of future work. In summary, the comparison between F_p at ignition for this unoptimised thruster and F_{cg} shows a total thrust increase of up to 40%.

The thrust reported so far does not include the slow increase of thrust over time shown in figure 4.10 which is attributed to the ceramic wall heating. This increase however has

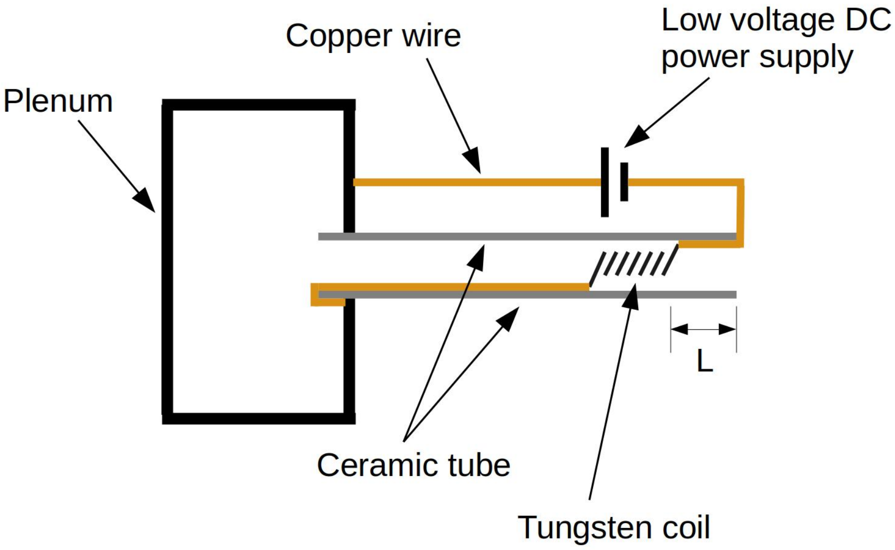

Figure 4.13: Diagram of the resistojet experiment. The tungsten heating element (formed as a coil) is moved inside the ceramic tube by a distance L, as discussed in the text. The aluminum body of the plenum serves at a path to close the DC current loop.

an important role in the overall performance of the system. To understand better this effect, a simple resistojet experiment was performed using a constant 100 SCCM argon flow into a same dimensions plenum and ceramic tube system. In this experiment, the RF antenna was replaced by a tungsten wire which is placed inside the tube and was heated up to glowing temperatures by 20 W of DC power. The heating element had a diameter of 2 mm and length of ∼1 cm and was placed at a distance L from the exhaust end of the tube. This is depicted diagrammatically in figure 4.13. Thrust measurements were made on the Wombat balance by setting up a constant 100 SCCM flow, then turning on the heating element for 20 s and recording the thrust at the end of that period. At $L =$0 mm, the thrust gain over the cold gas thrust, F_T/F_{cg}, was 1.99 dropping to 1.65 at $L =$5 mm, 1.34 at $L =$10 mm, 1.22 at $L =$15 mm and 1.08 at $L =$20 mm. This is shown in a plot in figure 4.14.

The gradual decrease in thrust can be attributed to the cooling down of the gas while traversing the final length of the tube which did not have enough time to reach a temperature equilibrium. An attempt was made to shift the RF antenna of the inductive pocket rocket closer to the exhaust end of the tube to confirm this observation with an RF plasma but the RF matching was affected possibly due to the pressure change near the exhaust end preventing acquisition of reliable data. This observation is going to be

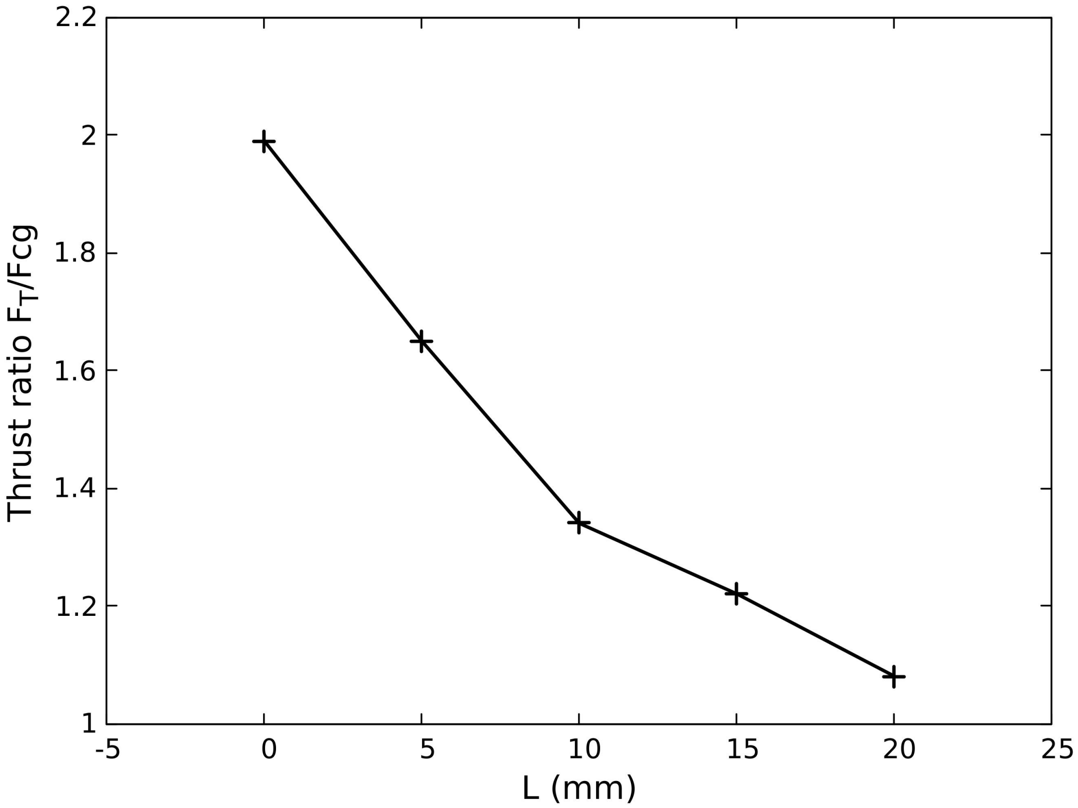

Figure 4.14: Thrust ratio (F_T/F_{cg}) versus distance L of heating element from the exhaust end of the ceramic tube showing the decrease of the resistojet benefit as the source of heat moves further away from the exit.

an important focus on future optimisations of this thruster.

Another point of interest to future optimisations is the formation of parasitic plasma outside the ceramic tube. This is due to the pressure in the vacuum chamber increasing from 10^{-6} Torr to $\sim 10^{-3}$ Torr when the thruster is operational which resulted in enough gas density to ignite and sustain a weak plasma outside the ceramic tube. The effect of this is that a percentage of the injected power is lost to that parasitic plasma which contributes to the lower performance of the thruster. In space, this is less likely to be a problem however it is possible to mitigate its impact by increasing the vacuum pumping speed and protecting the area directly over the antenna by the use of some inert material as padding, to inhibit the formation of plasma.

4.4 Summary

This chapter has described the development of the inductive Pocket Rocket. Based on the previous implementation, the capacitive Pocket Rocket, the IPR has demonstrated thrust gain at plasma ignition, operating as an electrothermal plasma thruster. A small foot print impedance matching network operating at 40.68 MHz and mounted directly onto the plasma cavity allows reliable measurements of direct thrust with inductive PR immersed in vacuum and attached to an optimised thrust balance. The custom made magnetic damper facilitates the measurement procedure by limiting thermal effects during plasma burns which allows reliable and repeatable measurements. The direct thrust measurements of the inductive PR have confirmed the production of thrust and have highlighted a couple of areas of improvement which will be considered in future work. Based on the reported results, future studies are justified and are expected to incrementally improve the performance of the presented proof of concept. These could include the operation of the RF amplifier in pulse mode.

Chapter 5

A class-E RF source for cubesat plasma propulsion

5.1 Motivation

In the previous chapter, the IPR electrothermal plasma thruster was presented, using RF as the source of energy to produce the plasma. Onboard a satellite with limited power resources, the RF energy needed by the plasma thruster is necessary to be produced with the highest possible efficiency. The challenges include not only the availability of adequate electrical power but also dealing with the waste heat generated by the process of converting DC power from the battery to RF power, suitable for the operation of the thruster.

One option to address both of these challenges is to use a class-E RF amplifier, briefly discussed in chapter 2. The development and measurement of such an amplifier in realistic space conditions is the topic of this chapter. The design of this amplifier is the product of the collaboration between Stanford University's Power Electronics Research Laboratory (SUPER-lab)[1] and the Australian National University's Space Plasma Power and Propulsion (SP3) group. The SUPER-lab team led the development of the electronics while the integration, vacuum test and performance verification took place at the ANU, as part of the work for this thesis.

It is worth noting that the design presented here participated in a competition organised by the power transistor manufacturer (NXP) which resulted in being awarded 3rd place[2].

---

[1] `https://superlab.stanford.edu/`

[2] `https://community.nxp.com/t5/NXP-Designs-Knowledge-Base/Homebrew-RF-Design-Challenge-Winners/ta-p/1110677`

5.2 Design

The design of an RF source system always begins with a set of specifications. In this case, the frequency of operation is determined by the load (RF plasma thruster) and is 40.68 MHz. The reason for this choice is explained in chapter 2 and will not be repeated here. Another important parameter is the output RF power required. For this design, this is set to approximately 40 W delivered to a 50 Ω load. The parameter of bandwidth is of less importance to a fixed frequency amplifier. Power supply on a small satellite is commonly available from the various power rails, with 12 V being common. In order to accommodate this, a separate DC/DC converter was designed which can be configured to increase the low satellite rail voltage to a higher voltage which is favoured by the RF transistor characteristics. The DC/DC converter can also be used to control the output RF power by adjusting its output voltage with the power output of the amplifier being proportional to the square of the input DC voltage. The RF transistor selected is the MRF101 produced by NXP and is a 100 W class, laterally-diffused metal-oxide semiconductor (LDMOS), field effect transistor (FET). It was decided to drive the amplifier with an external signal generator in the prototype version, however in the final design, this would be achieved by a suitable square wave oscillator located on the same printed circuit board. The final design schematic is presented in figure 5.1. The design was initially verified by performing a simulation using LT-SPICE[3], a circuit simulation software made by Linear Technology corporation (currently part of Analog Devices), based on the original SPICE code. A model for the MRF101 transistor was developed from the published manufacturer's data and was used in the simulation.

5.2.1 Input circuit description

The principle of operation in class-E amplification is based on using the active device as a switch, alternating between the *fully ON* and *fully OFF* (cut off) states, transitioning through the linear section as fast as possible. The ideal input waveform presented to the active device (in this case, a FET) is a square wave with fast rise and fall times. This is commonly achieved with specialised integrated circuits known as FET drivers which are designed to charge and discharge the input capacitance (C_{iss}) of FETs fast, by being able

---

[3] `https://www.analog.com/en/design-center/design-tools-and-calculators/ltspice-simulator.html`

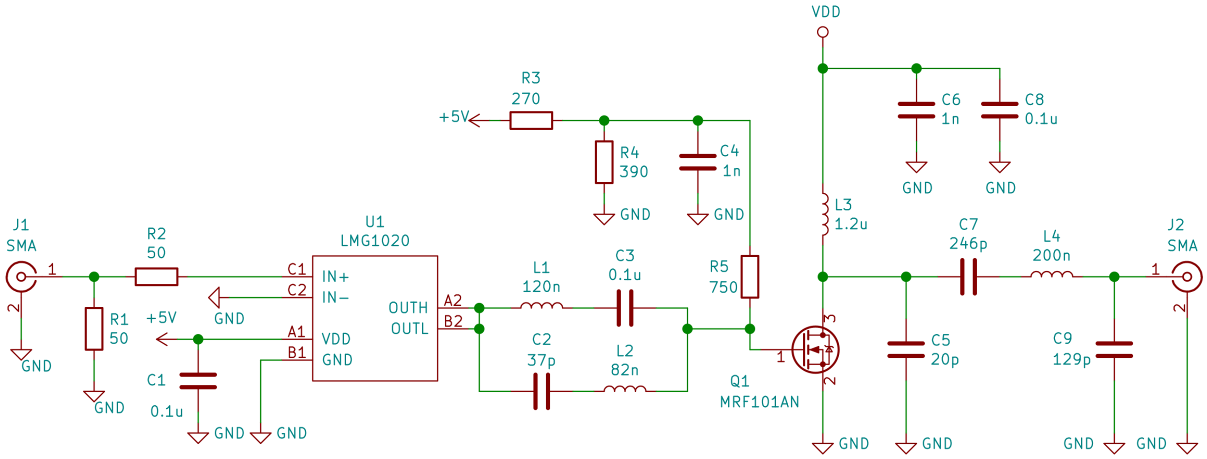

Figure 5.1: A simplified schematic of the 40.68 MHz class-E design.

to source and sink high currents. The FET driver used in this design is LMG1020 (U1 in figure 5.1). This device has a fast rise and fall time of typically 400 ps and can sink and source over 5 A of current. It has a high input impedance but in order to be able to use an external signal generator as the frequency source, the input is terminated with a 50 Ω resistance, to match the characteristic impedance of the standard coaxial cables used in the lab. The FET driver operates at 5 V and produces an output waveform of the same maximum voltage. This is not enough to drive the FET to saturation. To increase the voltage at the gate, two series LC resonant networks (L1 and L2-C2) are placed in series with the output. C3 is used for AC coupling. This multi-resonant network is resonant at the fundamental and third harmonic frequency as described in [109]. The result is a higher voltage, approximate square wave which is further shifted up in voltage by the resistive voltage divider formed by R3 and R4.

5.2.2 Output circuit description

The purpose of the output network in an RF amplifier is to convert the output impedance to the industry standard of 50 Ω while performing bandwidth restrictions and filtering, if that is necessary for the application. The output network of the class-E amplifier consists of L3, C5, C7 and part of L4, as seen in figure 5.1. The values are calculated by using the formulas in [44]. The remaining part of L4 and C9 form an impedance transformation network from the low output impedance of the class-E amplifier to the required 50 Ω. It also acts as a low pass filter, restricting the harmonics of the amplifier. C6 and C8

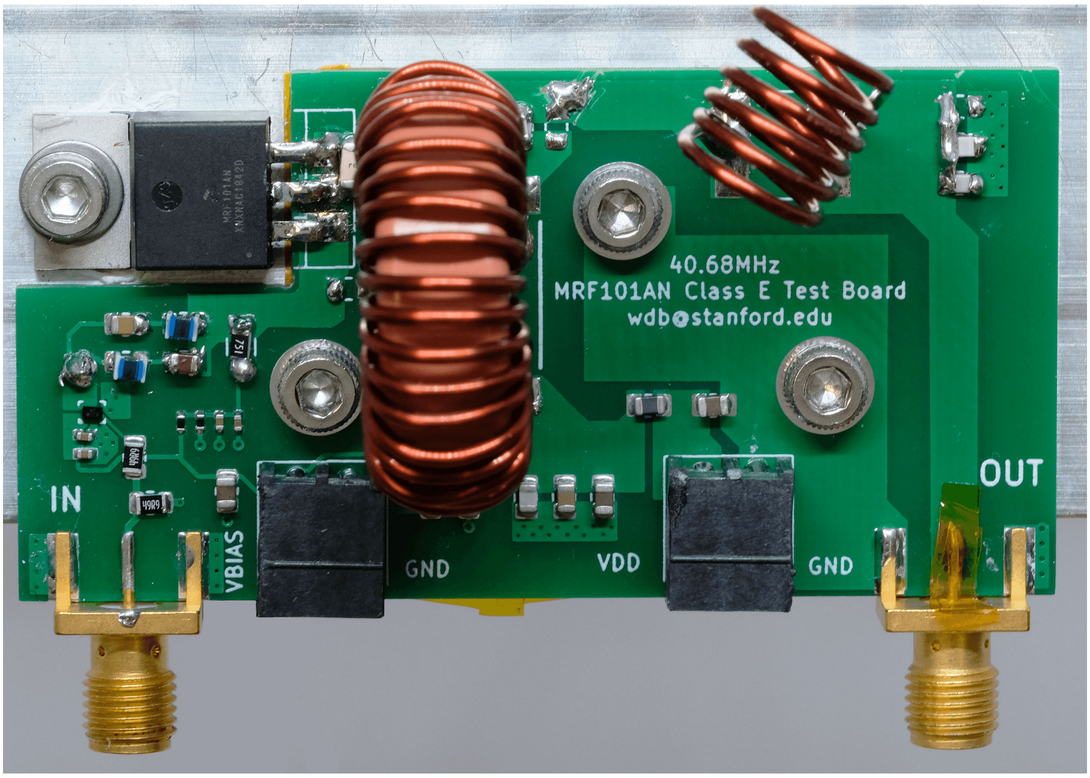

Figure 5.2: Photo of class-E amplifier as assembled. The amplifier PCB is shown here attached to a heat sink which was required for benchtop testing. During vacuum testing, the heat sink was removed and the PCB was attached to the frame of the cubesat which was used as a heat storage.

provide a low path to ground for RF that escaped the choke L3 in order to protect the power supply providing the operating voltage, V_{DD}, to the FET.

5.2.3 Performance measurement

In order to get an understanding of the benefit of the class-E design described in this section, a comparison was performed between the class-E amplifier and a reference design for 40.68 MHz presented in the datasheet of the MRF101 FET. The results of this comparison are presented in table 5.1. The reference design operated in class-AB which is typically used for linear amplification. It can be seen in the table that the efficiency increase by using the class-E technique is over 10 % for both 30 W and 40 W output power. The drain efficiency η is calculated in both cases as $\eta = \frac{P_{out}}{V_{DD} \times I_D}$ where P_{out} is the output RF power as measured on a $50\,\Omega$ load, V_{DD} is the drain DC input voltage and I_D is the drain current.

	Supply (V)	Output (W)	Drive (W)	Drain efficiency (%)
Class-E	32.8	30.1	0.65	91.3
Class-E	37.5	40.0	0.65	91.1
Class-AB	23.8	30.1	0.5	80.3
Class-AB	27.6	40.0	0.5	80.7

Table 5.1: Efficiency comparison between the class-E amplifier using the MRF101 FET and the reference design (class-AB) provided by the manufacturer.

5.2.4 DC/DC converter

The DC/DC converter was designed by the Stanford SUPER-lab to match the class-E RF amplifier described earlier. It is required to boost the 12 V power rail on the satellite to the high voltage required by the amplifier. The DC/DC converter accepts an input voltage of 12 V to 16 V. Control of the output voltage is achieved by a AD5245BRJZ10-RL7 I^2C digital potentiometer. This allows the satellite on-board computer to adjust the voltage and therefore the RF output power as needed, by using the industry standard I^2C serial communication bus. It can be addressed by the I^2C pins on the connector and can be bypassed, if fixed voltage operation is desired, by using a built in resistor voltage divider. By changing two resistor values the voltage range can be altered. The upper voltage limit is approximately 36 V and the lower voltage limit is approximately 24 V. The heart of the DC/DC converter is the LTC7818 high performance buck/boost converter chip. It is configured for a switching speed of approximately 750 kHz. The efficiency of the DC/DC converter was found to be approximately 95 %, dropping slightly as as the load power decreases.

5.3 Integration with the IPR

In order to test the RF amplifier in realistic space conditions, the IPR was installed on an aluminium cubesat frame, as seen in figure 5.3. The IPR is installed externally to the cubesat frame. Gas is provided through a nylon hose which is routed via a gas feedthrough on a flange on a port on the vacuum chamber to an external Alicat gas flow controller. The controlled is connected to a cylinder containing xenon gas which sits besides the Wombat chamber. All electrical and gas lines are routed outside the cubesat frame via a center hole which is at the bottom facing side, when the thruster is mounted onto the thrust balance. A small diameter RG-316 coaxial cable is used to carry the 40.68 MHz

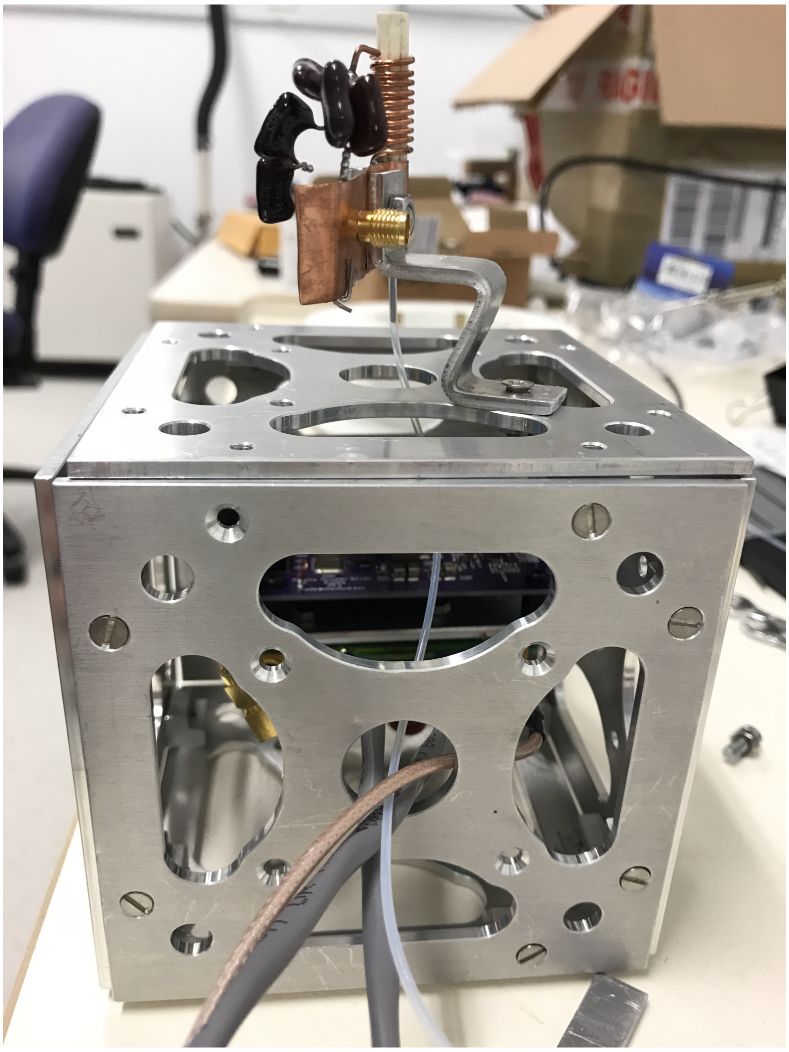

Figure 5.3: The integrated IPR and RF source in a cubesat frame, sitting on the workshop table. The class-E amplifier and DC/DC converter are installed installed inside the cubesat frame while the IPR is installed on the top side as seen in the photo.

square wave signal needed to drive the amplifier. This signal is produced by an external signal generator. Finally, the two gray cables seen in figure 5.3 provide the DC power needed to power the electronics. The aluminium frame of the cubesat is approximately 0.4 kg and used as a heat storage mass for the heat produced by the class-E amplifier and DC/DC converter.

5.3.1 Waste heat calculations

The waste heat, P_h, for the production of RF power, P_{rf}, of 30 W by the DC/DC converter and the class-E amplifier combination, assuming efficiencies for the production of the RF

$\eta_{rf} = 0.90$ and the DC/DC converter $\eta_{dc} = 0.95$ is going to be

$$P_h = \frac{P_{rf}}{\eta_{rf} \times \eta_{dc}} - P_{rf} \tag{5.1}$$

Most of the heat will be produced on the MOSFET in the RF amplifier which is thermally connected directly to the cubesat frame. For 30 W of RF delivered to the plasma, the waste heat is calculated to be approximately 5 W. The specific heat capacity c_p of aluminium is approximately $0.9\,\mathrm{J\,g^{-1}\,K^{-1}}$ which, for the 400 g aluminium frame used in this experiment, results in a temperature increase rate of $0.83\,\mathrm{K\,min^{-1}}$. This implies that the thruster can run for several minutes at a time without resulting in its temperature rising to potentially catastrophic levels. If a burn of several minutes is required, the limitation is likely to be in the capacity of the batteries to provide the energy needed rather than overheating.

In this calculation, only the waste heat produced by the electronics was assumed to be stored in the cubesat frame. In reality, the plasma cavity will also heat up when the plasma is ignited. The cavity is made with heat proof ceramic material (alumina) that can survive temperatures over 1000 °C. The combination of relatively low thermal conductivity of the ceramic material and more efficient radiation of that energy as the temperature increases (Stefan-Boltzmann law) results in small residual contribution of heat from the thruster to the cubesat frame. It is, however, important for this heat transfer to be accounted in the overall heat budget calculations.

5.4 Direct thrust measurements

Once the cubesat is assembled, it is placed in the Wombat space simulation chamber for a direct thrust measurement. The thruster is configured for 30 SCCM ($2.7\,\mathrm{mg\,s^{-1}}$) of xenon and the RF amplifier is set up to produce 30 W. A cold gas measurement is made initially to confirm the thrust produced without the electrothermal plasma thruster switched on. The cold gas thrust was found to be approximately 488 µN, implying a specific impulse I_{sp} of 18.4 s. The RF is then switched on and the thrust jumps by another 280 µN which is an increase of 57 % and the I_{sp} is now 29 s.

A photo of the thruster operating in the Wombat space simulation chamber can be seen in figure 5.4. In this photo it is possible to see the spherical shaped expansion

Figure 5.4: The class-E amplifier powering the IPR thruster using xenon, photographed operating in the Wombat space simulation chamber.

of the plasma as it exits the ceramic tube. A parasitic plasma can be seen forming a halo in the general area of the matching network (brown capacitors to the bottom of the antenna). This parasitic plasma has a detrimental effect on the matching network components which will need to be protected in the final design. The brightness (and therefore density) of the plasma is highest at the antenna. Figure 5.5 shows a plot of the light density (arbitrary units) along the axis of symmetry. The drop of the light as we move away from the exhaust end of the ceramic tube resembles the density and plasma potential drops reported in [110, 111].

5.5 Summary

The objective of this chapter was to provide evidence that this proof of concept consisting of the IPR powered by a high efficiency class-E RF amplifier, is a viable proposal for cube-sat propulsion. This was done by performing measurements to show the high efficiency achieved by this design which results in little heat being generated by the electronics

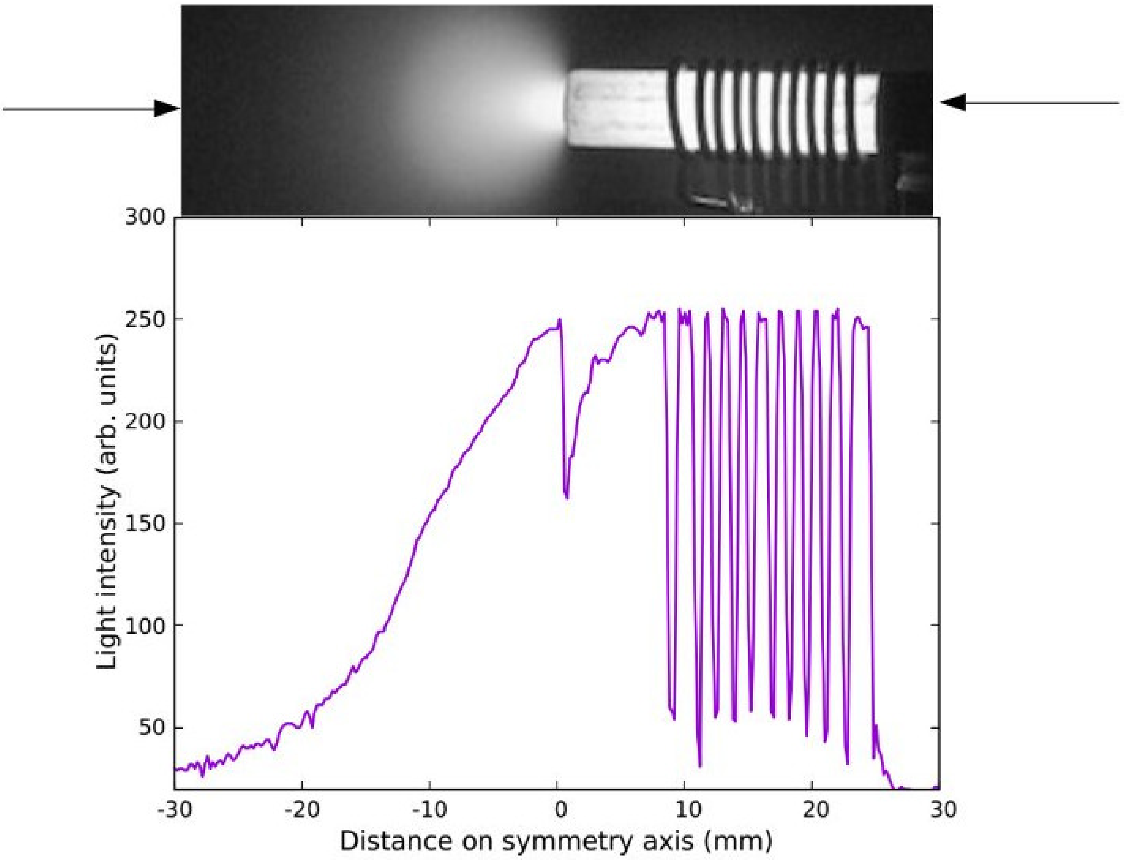

Figure 5.5: Plot of the light captured by the camera along the axis highlighted by the two arrows.

which can easily be accommodated by dumping it on the cubesat frame.

To further support this claim, the combination of the RF source, power supply and IPR was placed in the Wombat space simulation chamber and a thrust measurement was made. The measurement showed an increase in the thrust by the operation of the system, as expected by a prior, more detailed measurement campaign presented in chapter 4.

Chapter 6

Naphthalene as a nano-satellite propellant

6.1 Motivation

In chapter 1, the very high tank pressure in the propellant reservoir of thrusters that use a noble gas such as argon, krypton and xenon, was identified as an engineering challenge. This is due to the difficulty in eliminating propellant leaks due to the very high storage pressure but also the difficulty in designing pressure regulation and control mechanisms that reduce the thousands of PSI in the tank to a few Torr, a pressure differential of multiple orders of magnitude. This poses difficulties not only in the engineering of the thruster but increases the cost and makes compliance with the safety requirements of the launch vehicle harder to achieve. The storage of propellant in gaseous state also results in lower storage density and therefore the requirement for higher reservoir volume. This chapter discusses the benefits and shortcomings of solid propellants and introduces naphthalene as a candidate for a cubesat cold gas system. A cold gas thruster based on naphthalene is built and characterised via a series of direct thrust measurements performed in the Wombat space simulation chamber.

6.2 Solid propellants for cubesat thrusters

Using a solid propellant has many advantages over one that is stored as liquid or gas. Solid propellants generally have much higher storage density, allowing more propellant to be stored for a given reservoir volume. Liquid propellants may have higher density than gas propellants but suffer from sloshing (uncontrolled movement of the liquid in the reservoir under zero gravity conditions) or phase separation problems. The idea of using a propellant that is stored in the solid state is not new. Out of all proposed candidate thrusters, a few can be scaled down to match the cubesat requirements. One such category includes vacuum arc thrusters (VAT) [112, 113] which typically use metals and alloys [114] or more novel material such as carbon fiber reinforced plastic [115] as the propellant. This technology shows promising results achieving high specific impulse and therefore good fuel efficiency but is limited to pulsed operation and suffers from low electrical efficiency, typically delivering approximately $10\,\mu\mathrm{N\,W^{-1}}$ [116]. The delivered thrust is generally in the micronewtons to tens of micronewtons which, coupled to the low duty cycle pulsed operation, results in thruster suitability for only small magnitude orbital manoeuvres such as orbit maintenance, performed by lower mass spacecraft.

6.2.1 Iodine

Of particular interest to the cubesat propulsion system designer is a category of solid propellants that rely on sublimation to produce a gaseous propellant prior to use. One such propellant that has been proposed [117] and recently tested in space [118, 119] is iodine. Iodine is solid at room temperatures and has a melting point of 113.7 °C and sublimates readily producing a characteristic violet gas. The vapor pressure is approximatelly 7.5 Torr at 68 °C [120–122] which is enough to support a cold gas propulsion system. The main disadvantage of using iodine as a propellant is that it reacts aggressively with materials commonly used in aerospace applications, such as aluminium, stainless steel and various polymers. The repercussions of this chemical incompatibility are many and affect not only the final product but also the ground infrastructure required for the development and measurement of the thruster (vacuum chambers, thrust balances, etc). I2T5 is a cold gas thuster using iodine that was built and successfully tested in space by the company ThrustMe[1] [118]. This thruster has an interesting feature which is the inclusion of an unusual valve combination to control flow [123] before launch and between thruster firings while in orbit. The valve relies on the very low vapor pressure of iodine at room temperature (75 mTorr at 8.8 °C) to ensure that no substantial pressure exists in the tank when the thruster is not in use. A polymeric membrane is used to seal the reservoir before the placement of the satellite into orbit. This membrane is sublimated away prior to the first operation of the thruster using an infrared emitter in the proximity of the seal. A *static* valve is then used as an ON/OFF valve. This valve relies on solidifying

---

[1] `https://www.thrustme.fr`

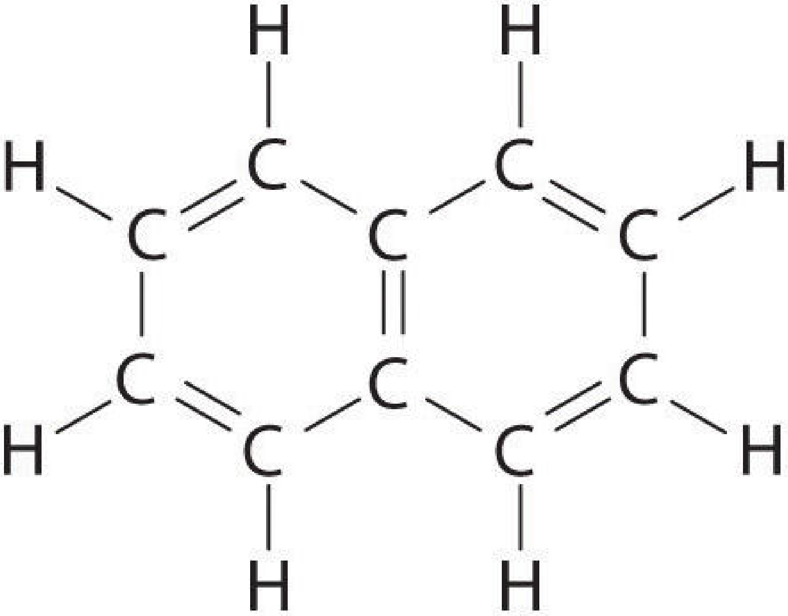

Figure 6.1: Chemical structural formula of naphthalene showing the bonds between the carbon and hydrogen atoms. The two carbon rings (benzene rings) are a central feature of naphthalene which qualify it as the smallest sized polycyclic aromatic hydrocarbon (PAH).

iodine in the passage to the nozzle in order to stop the flow of propellant (OFF state) or fully unblocking that passage through heating (ON state) and as a result, it has a slow reaction time. According to [123], a more conventional solenoid valve that will resist the corrosive effects of iodine is under development. The complexities of the valve design of this thruster highlight the engineering difficulties faced when working with a very reactive propellant such as iodine.

6.3 Naphthalene

6.3.1 Physical properties

In this section the physical properties of naphthalene that are of interest to the thruster designer are discussed. Naphthalene is the simplest polycyclic aromatic hydrocarbon (PAH) consisting of two carbon rings and having a formula of $C_{10}H_8$. The expanded chemical structural formula of naphthalene can be seen in figure 6.1. Its molecular weight is $128.17\,\mathrm{g\,mol^{-1}}$ which is similar to that of xenon ($131.29\,\mathrm{g\,mol^{-1}}$) and approximately half that of molecular iodine (I_2, $253.8\,\mathrm{g\,mol^{-1}}$). At room temperature and 1 atm pressure conditions, naphthalene is a solid in crystalline form and has a melting temperature of

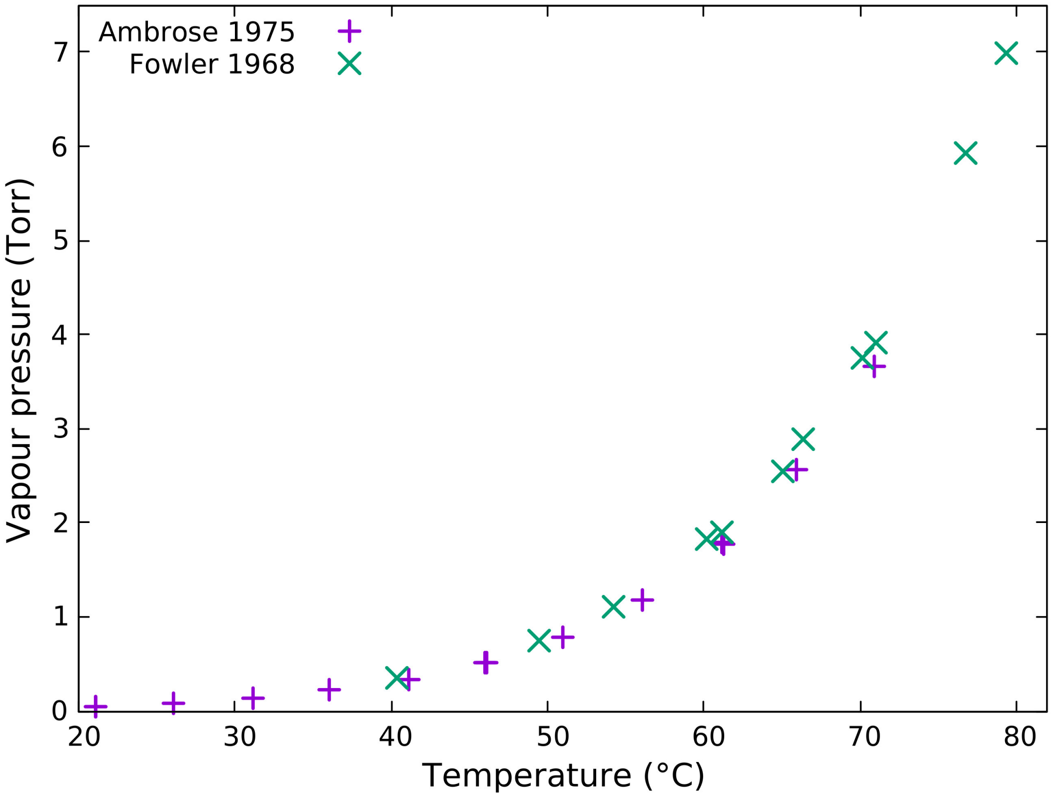

Figure 6.2: Naphthalene vapour pressure versus temperature as reported by Ambrose et al [124] (purple +) and Fowler et al [125] (green **X**).

approximately 80.2 °C and density of 1.16 g cm^{-3}. An important characteristic of naphthalene making it a suitable cubesat thruster propellant candidate is that it sublimates. The sublimation process results in the development of vapour pressure, seen in figure 6.2, using data previously reported in the literature [124, 125]. In this figure the vapour pressure is shown for a temperature range that is in the proposed operational range, just below the melting point of 80.2 °C. It can be seen that for a temperature of about 70 °C, the expected vapour pressure is approximately 3.7 Torr, a value that is comparable to that of other cold gas thrusters operating with argon [52]. It exhibits good compatibility with many materials commonly used in space. Of particular interest is the compatibility with aluminium and stainless steel which can be used in the reservoir and distribution network piping [126]. It is also compatible with polytetrafluoroethylene (PTFE, commonly known by the commercial name Teflon®) and fluoroelastomers such as Viton®, which are materials commonly used for sealing in the form of o-rings and sealing rubber in spring-loaded, ON/OFF valves.

Naphthalene's thruster-friendly properties have inspired some work in evaluating its

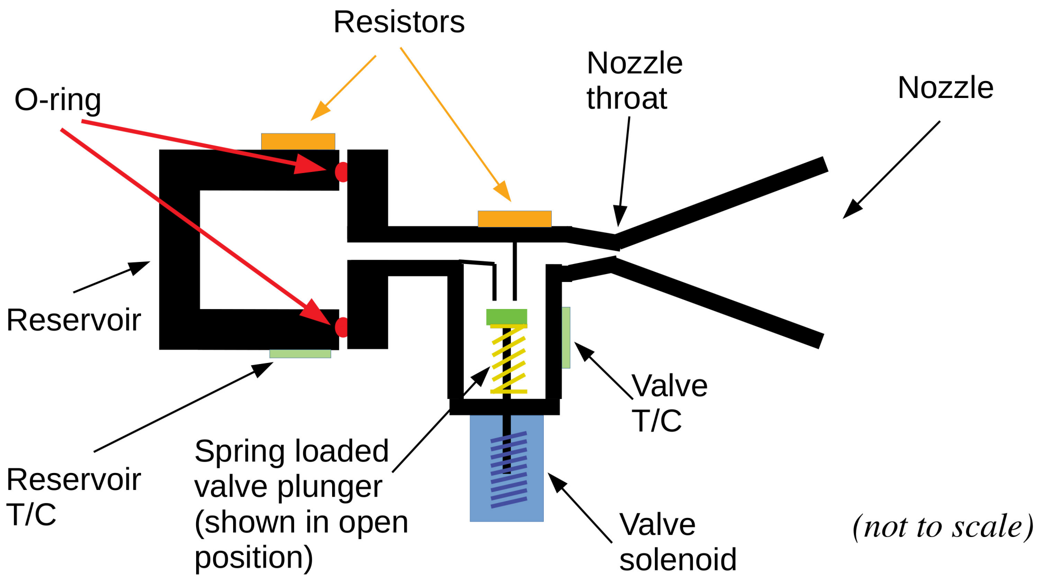

Figure 6.3: Diagram of the naphthalene thruster with its main components highlighted. The reservoir temperature T_r is measured by the reservoir T/C and controlled by the reservoir heater resistor; the valve temperature T_v is measured by the valve T/C and controlled by the valve heater resistor.

merit as a propellant. In 1963, very early in the satellite era, Olds [127] identified naphthalene as a cold gas propellant of interest for large satellites, based on an examination of its physical properties. He predicted that the simplicity of the design and potential reliability can probably make up for the limited performance compared to other propellant options. Yoneshige [128] described a design of a micro-thruster using naphthalene as the propellant but did not include and practical measurements of its performance. Chujo et al. [129] evaluated a concept naphthalene thruster in the laboratory but only included theoretical thrust calculations based on measurements of the reservoir pressure, for relatively low propellant temperatures (below 40 °C).

6.3.2 Sublimation of naphthalene

The process of sublimation can be examined as the result of two competing processes: evaporation and condensation [130, 131]. In a closed system in equilibrium, the rate of evaporation is equal to that of condensation which results in a constant pressure. This pressure is the vapour pressure and is a function of the sublimating material temperature. Before equilibrium is achieved, the sublimation rate will be equal to the difference between the evaporation rate and the condensation rate. The sublimation rate can be expressed mathematically by the following equation initially proposed by Miyamoto [131] and published in this form below by Polzin et al [132]:

$$\frac{dm}{dt} = aA\sqrt{\frac{M}{2\pi RT}}(p_v - p) \tag{6.1}$$

where a is the ratio of condensing to incident molecules and is approximately equal to 1, A is the surface area of the sublimating naphthalene, M is the molecular mass, R is the universal gas constant, T is the temperature, p_v is the expected vapour pressure for temperature T and p is the static pressure in the reservoir (tank) in which the sublimation takes place.

When the reservoir valve is opened, gaseous naphthalene will escape resulting in continuing sublimation occurring as $p < p_v$. The gaseous naphthalene can be routed to the nozzle of the thruster becoming the propellant of a cold gas thruster system with the sublimation rate becoming equal to the thruster mass flow rate, $\dot{m} = \frac{dm}{dt}$.

So far, we have treated the temperature of the naphthalene during sublimation as a constant and equal to the reservoir temperature. This is not accurate as the process of sublimation is an endothermic process. The enthalpy of sublimation, also known as heat of sublimation, is the property that captures this energy requirement. For naphthalene, the enthalpy of sublimation is approximately $72.8\,\mathrm{kJ\,mol^{-1}}$ [133] for the proposed thruster operating temperature range ($50°C$ to $70°C$). For an expected mass flow rate $\dot{m}$ of $1.6\,\mathrm{mg\,s^{-1}}$, this results in a sublimation power requirement P_{sub} of 0.91 W. This power needs to be provided by the reservoir heater system, hence the total electrical power (P_{tot}) required for steady state operation will be:

$$P_{tot} = P_{loss} + P_{sub} \tag{6.2}$$

where P_{loss} is the heat loss due to imperfect heat insulation of the system as well as the power required to keep the valve open, if a non-latching valve is used. P_{loss} in a well engineered system in vacuum can be kept to a couple of watts, which results in P_{tot} of a few watts, a value that is compatible with the power restrictions on a cubesat.

As described earlier, the sublimating naphthalene requires energy in the form of heat and that energy is provided by the electrically heated reservoir through radiation and conduction. The radiated heat flux $j^{\star}$ will be determined by the Stefan-Boltzmann law and is a function of the reservoir's temperature T_r and emissivity ϵ_r, and the propellant's effective emissivity ϵ_n and temperature T_n:

$$j^\star = \sigma(\epsilon_r T_r^4 - \epsilon_n T_n^4) \tag{6.3}$$

where σ is the Stefan-Boltzmann constant ($5.67 \times 10^{-8}\,\mathrm{Wm^{-2}K^{-4}}$).

Conduction of heat will happen mostly through the bulk of the solid naphthalene in the reservoir and that will be determined by naphthalene's heat conductivity resulting in a heat flux of:

$$q = -k\nabla T \tag{6.4}$$

where k is the thermal conductivity of the propellant and ∇T the temperature gradient.

Naphthalene has a low thermal conductivity of approximately $0.1329\,\mathrm{W\,m^{-1}\,K^{-1}}$ at room temperature [134] and this results in a conducted heat flux that is of the same order of magnitude as the radiated heat flux.

The impedance in the prompt conduction of heat from the hot reservoir walls to the sublimating naphthalene can result in a localised temperature drop in the sublimating area, which in return results in a lower p_v, causing a lower mass flow rate and consequentially a lower thrust. The designer of the cold gas naphthalene thruster needs therefore to ensure the heat transfer is maximised via both radiation and conduction modes from the reservoir to the propellant.

6.3.3 Proof of concept naphthalene thruster

A diagram of the proof of concept naphthalene cold gas thruster can be seen in figure 6.3 and a photo of the thruster mounted on the thrust balance can be seen in figure 6.4. The propellant is stored in a reservoir made of aluminium. It has a cylindrical shape of approximately 75 mm diameter and 50 mm length. The maximum volume of propellant it can hold is approximately $95\,\mathrm{cm}^3$ (approximately 100 g when full). The reservoir lid, also made of aluminium, is held in place by four screws and has a gaseous naphthalene extraction line of internal diameter of 3 mm which is attached to a valve. Pressure sealing is achieved by a Viton® o-ring sitting in a groove on the reservoir and compressed by the lid. When fully compressed, the lid provides good thermal transfer contact with the

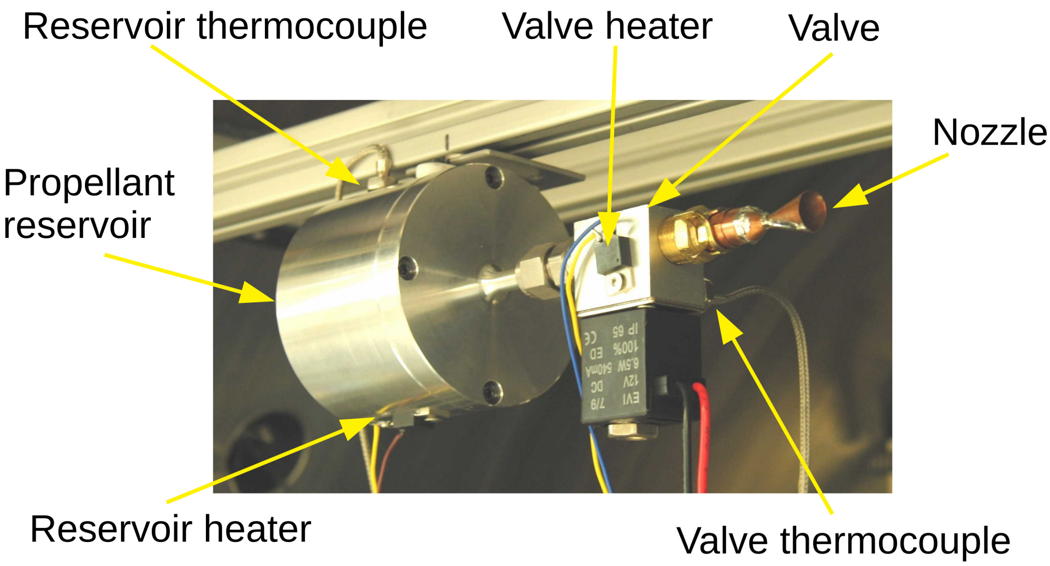

Figure 6.4: Photo of the naphthalene thruster proof of concept (figure 6.3), mounted on the thrust balance within the Wombat space simulation chamber (figure 2.4) with its main components highlighted. The photo is taken without the multi layer insulation for clarity.

heated reservoir, to ensure both are at the same temperature. Aluminium was selected for its excellent thermal conductivity of $237\,\mathrm{W\,m^{-1}\,K^{-1}}$ as well as its compatibility with naphthalene, as mentioned earlier. The valve is a spring-loaded ON/OFF valve which is normally closed. The body of the valve is also made of aluminium and its dimensions are 30 mm by 20 mm by 55 mm, including the solenoid. The valve used in this experiment is commercially available and supports a much higher pressure differential than the $1\ atm$ or less, needed by the thruster. It is therefore envisaged that the final design will have a custom valve based on the same principle, smaller in size and more tightly integrated to the tank, resulting in a thruster occupying 1/3 to 1/2 of a cubesat unit, and having a wet mass (mass of propulsion system plus propellant) of no more than 0.5 kg, inclusive of the associated electronics.

A 12 V solenoid is used to actuate (open) the valve. At the outlet of the valve is attached a de Laval (convergent-divergent) nozzle. The nozzle is made of copper and is not optimised for the operating conditions of the proof of concept system. It is envisaged that the nozzle will be optimised for the selected parameters of operation in future studies.

There are two heating zones which are the reservoir and the valve, as seen in figure 6.3. Each heating zone has its own heating element (TO-220 packaged, 100 Ω resistor), a K-type thermocouple (T/C) and an external thermostat. Each thermostat can be set individually to hold the corresponding zone to a constant temperature. It was found that the temperature could be kept within 1 °C of the set value using this system. During measurements, the valve temperature was maintained at a temperature slightly higher (here chosen to be at least 5 °C) than that of the reservoir to prevent naphthalene condensation in the valve. The gas transfer line between the valve and the reservoir does not have its own heater. It instead relies on heat transfer from the valve and reservoir via conduction. Similarly, the nozzle is heated up through conduction of heat from the valve. In an initial 5.5 h long term thrust measurement experiment, a slow decrease in thrust was observed before the thruster ran out of propellant. It was attributed to a decrease in the flow rate, due to a suspected cold spot in the reservoir-valve transfer line causing slow condensation of naphthalene and restricting the flow of gas. To address this problem, a simple passive insulation system consisting of a few layers of multi layer insulation (MLI) wrapped around suspected cold spots was installed and the experiment was repeated. The outcome of this intervention was an improvement in the stability of the flow rate over time, indicating that the condensation hypothesis was likely the cause of this decrease.

The thrust measurement results of both experiments are presented in section 6.3.7. By using this heating and insulation technique, condensation of naphthalene in that zone was limited and no blockage was ever observed over tens of hours of laboratory operation of the thruster. The thruster was mounted to the thrust balance frame via a MACOR® machinable glass ceramic adaptor (not shown in figure 6.4), to reduce the heat loss via conduction to the balance frame. MACOR® has very low thermal conductivity of $1.46\,\mathrm{W\,m^{-1}\,K^{-1}}$. No effort was made to further heat insulate the thruster reservoir and valve to minimise heat loss through radiation. Despite this, the average power required to maintain the thruster at 70 °C was around 4 W, increasing slightly when the valve was open. This loss can be substantially reduced in the future by using heat insulation materials and techniques commonly utilised in spacecraft for heat isolation.

As discussed in section 6.3.2, the designer of the cold gas naphthalene thruster needs to optimise for maximum heat transfer from the hot reservoir walls to the propellant. Such optimisation was not done for this proof of concept but would be important in the design of a flight prototype.

6.3.4 Safety

Naphthalene is a household chemical (mothballs), commonly used to protect stored items from damage from moths. It is a flammable substance and needs to be stored and handled away from sources of ignition. When the thruster is installed in the vacuum chamber, there is no risk of fire. Naphthalene is also toxic to humans and nature, in particular aquatic life. To avoid any exposure, the loading of the tank needs to take place in a well ventilated lab, using appropriate personal protection equipment including gloves. Once in the vacuum chamber, the vapour produced during the operation of the thruster is pumped outside, resulting in no residual smell in the lab. Appropriate signage has been installed to remind the users not to dispose of any naphthalene by tipping it in the lab sink.

6.3.5 Experimental results

6.3.6 Thrust balance set up

The thrust measurements were conducted in the previously described Wombat space simulation chamber [39, 40] using a high sensitivity thrust balance [41], shown in figure 2.4. This balance consists of a four arm pendulum suspended frame. The thruster is mounted on the frame and operation of the thruster results in a displacement from the rest position (figure 2.4). The displacement, which is proportional to the thrust force, is accurately measured by a laser triangulation displacement sensor (ILD7100), with a resolution of 0.1 µm. The balance includes a built-in calibration system consisting of a set of accurately measured weights which are placed on the balance via a pulley and controlled by a stepper motor. The calibration system is used in each measurement to determine the conversion constant from displacement to force. A detailed description of the thrust balance can be found in chapter 3. The thruster is attached on the frame using a MACOR® adaptor to ensure minimal thermal leakage from the warm reservoir to the room temperature frame (figure 2.4). A set of vacuum feedthrough connections on the vacuum chamber was used to enable connection of heater power, valve control and temperature measurements to the power supply, valve control signal source and thermostats, all located outside the chamber.

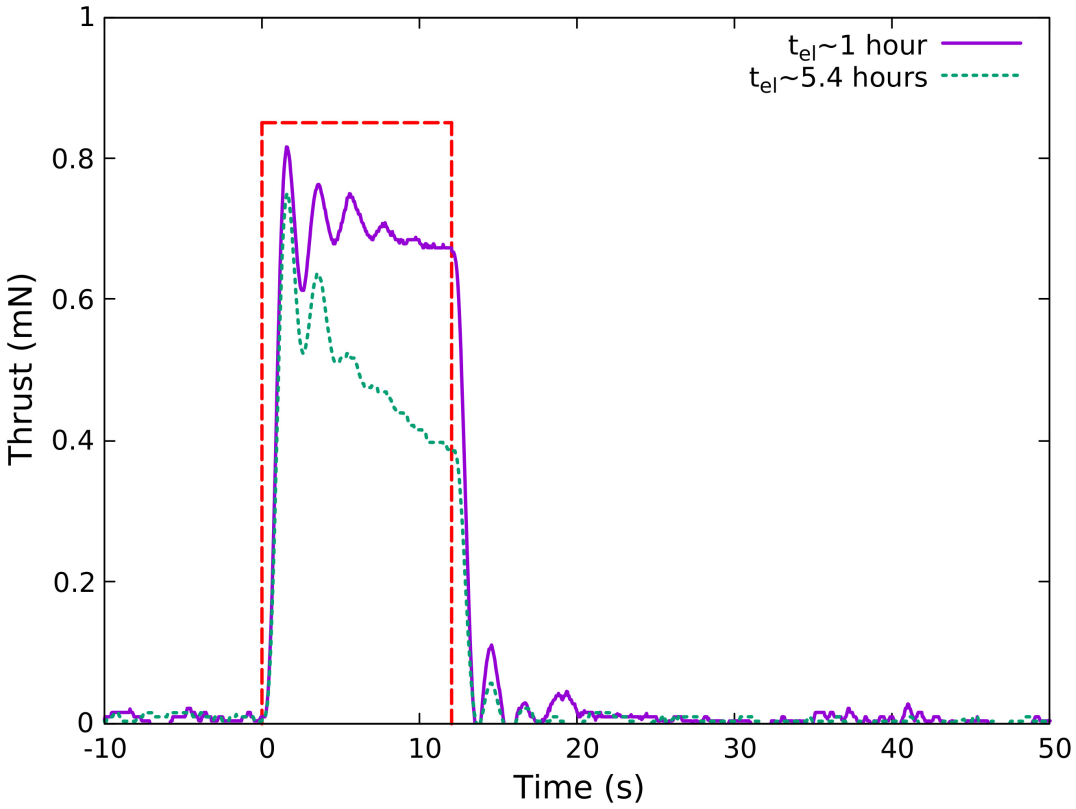

Figure 6.5: Plot of thrust versus time of two 12 s burns taken at 1 h (purple solid line) and 5.4 h (green dotted line) elapsed time (t_{el}). The red dashed line serves as a visual guide representing an *ideal* 12 s burn. At the beginning of the run ($t_{el} = 0$), the reservoir was loaded with 10 g of naphthalene. The duration of the run was approximately 5.5 h and throughout the run, the temperature of the reservoir was maintained at 70 °C. The damped oscillation seen at the beginning and end of each burn is due to the effect of the magnetic damper of the thrust balance and is discussed in section 6.3.6 and chapter 3.

6.3.7 Thrust measurements

An initial thrust measurement experiment was performed to quantify the performance and stability of the thruster. Both short term (within a single burn) and long term (from the beginning of thruster operation to exhaustion of propellant) variations are of interest to the thruster designer and cubesat operator. A small amount of naphthalene (10 g) was placed in the reservoir and the thruster was configured to run continuously until the propellant was fully exhausted. The thruster was set up for 12 s burns and 60 s period resulting in a duty cycle $D = 0.2$. This combination of burn time and period was selected as it provided an opportunity for the thruster reservoir to fully recover ($p = p_v$) between burns, and is a variable that can be altered by the thruster designer to suit the specific propulsion and operating requirements of the space mission. The reservoir temperature

T_r was set to 70 °C and the valve temperature T_v to 75 °C, both held to ± 1 °C by their respective thermostats. T_v needs to be higher than T_r in order to prevent condensation of naphthalene in the valve body, as this could affect the flow rate or in the worst case, completely block the flow of gas.

The value of T_v is not critical as long as it is higher than T_r under all operating conditions. The vacuum chamber pressure measured using an ion gauge with the thruster valve shut was $\sim 5 \times 10^{-5}$ Torr, increasing to $\sim 5 \times 10^{-4}$ Torr upon opening the valve. The measured chamber pressure is at least three orders of magnitude lower compared to the expected pressure in the reservoir due to the naphthalene vapour pressure at the operating temperature range of 50 °C to 70 °C (figure 6.2). This ensures the thruster is operating in choked flow conditions, as described in detail by Ho et al [52].

The experiment took a bit over 5.5 h of elapsed time, t_{el}, (defined as the absolute time from the beginning of the experiment) to complete. During that time, over 330, 12 s burns were performed. Thrust measurements from two individual burns taken near the beginning ($t_{el} \approx 1$ h) and the end ($t_{el} \approx 5.4$ h) of the run are shown in figure 6.5. An *ideal* burn with constant thrust (of arbitrary value for visualisation purpose) during its 12 s duration is also shown in this figure as a red dashed line overlapping with the two measurements. The burn early in the run (purple line) indicated a thrust of ~ 0.67 mN (average thrust over the 12 s burn time) and appears to be deviating very little from the ideal burn. The slow rise and fall times as well as the damped oscillation following the opening and closing of the valve, are a result of the thrust balance damping mechanism and do not relate to the actual thruster performance. A small decline (droop) in the thrust can be seen as the valve is about to close and that can be attributed to the lack of pressure regulation. This decline is less than 10 % at the beginning of the run, increasing to over 40 % just before the depletion of the propellant. The exact magnitude of the droop is a function of the design parameters such as reservoir volume and propellant mass. Lower mass of propellant in the reservoir results in lower sublimating area A and therefore a lower gas production rate, as implied by equation 6.1. Larger reservoir volume results in more gaseous naphthalene available to the thruster. The amount of drooping is also affected by the reservoir temperature. This effect can be seen in figure 6.6. In this figure, three consecutive burns of 12 s duration are shown for 50 °C, 60 °C and 70 °C reservoir temperature. In all three cases, the amount of propellant in the tank is approximately the same. The drooping of the thrust appears to increase as the

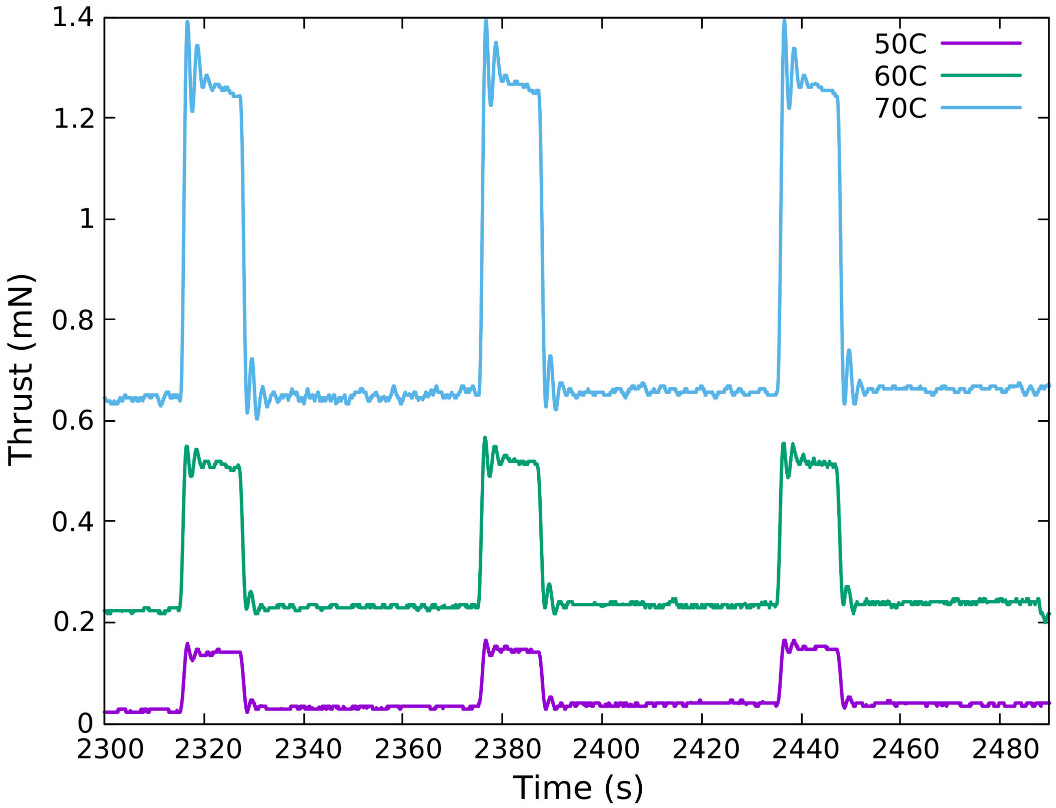

Figure 6.6: Effect of the reservoir temperature on thrust *droop*. In this plot the thrust produced by three consecutive 12 s burns at 50 °C, 60 °C and 70 °C reservoir temperature is shown. This sequence is taken about 38 min after starting the experiment, when the tank is still nearly full. It can be seen that the thrust droop is reduced as the reservoir temperature is decreased. The base level of each curve (zero thrust) has been shifted for clarity.

temperature of the reservoir is increased. This can be explained by the increased mass flow rate at the higher temperature, resulting in an increased sublimation rate. The increased sublimation rate in return, results in quicker cooling of the sublimating area which is assumed to be equal in the data shown in figure 6.6 because of the equal amount of naphthalene in the reservoir at that time. The quicker cooling is due to the enthalpy of sublimation of naphthalene, as described in section 6.3.2. As an extension to this, we can deduce that the shape of the reservoir and the mechanism employed to keep the solid naphthalene secure in zero gravity conditions are also going to have an impact in this decrease.

The effect of this thermal balance process on the thrust generation is more pronounced on the burn closer to the end of the run, shown in figure 6.5 as a green line. In this case, the opening of the valve results in a relatively large thrust as the reservoir pressure had enough time to recover since the previous burn, but the sublimating area A is now much

T_r ($°C$)	T_v ($°C$)	F_T range (mN)	Average $\dot{m}$ (mg/s)	Specific impulse I_{sp} (s)
50	65	0.11 ± 0.03	0.54	20.7
55	70	0.21 ± 0.03	0.95	22.5
60	75	0.29 ± 0.03	1.23	24
65	75	0.41 ± 0.04	1.7	24.6
70	75	0.6 ± 0.07	2.49	24.6

Table 6.1: Measured thrust F_T, and calculated mass flow rate $\dot{m}$ and specific impulse I_{sp} of the naphthalene cold gas thruster for various reservoir and valve temperatures T_r and T_v respectively.

less compared to the beginning of the run and the sublimation rate is not high enough to sustain a high mass flow rate of the expelled propellant resulting in a rapid decline.

To quantify the effect of this thrust decline over time, two runs of 10 g of naphthalene to exhaustion were carried out, with the resulting average burn thrust plotted versus elapsed time shown in figure 6.7. The purple line data was obtained with no insulation in the reservoir-valve transfer line and nozzle. A slow but steady decline can be seen in during the first $\sim 5\,\text{h}$ of operation, followed by a rapid decline as the propellant is about to run out. This decline is mainly due to the reduction of the sublimating area over time discussed earlier, however it was suspected that naphthalene may be depositing in a cold spot somewhere in the reservoir transfer line or valve-nozzle line, resulting in a reduction of flow rate. The second 10 g run measurement (green line in figure 6.7) was conducted, this time having a few layers of multi layer insulation (MLI) covering both the transfer line and nozzle. This resulted in a decrease in the slow decline over time, maintaining a more consistent flow rate and was eventually followed by the rapid decline indicating the exhaustion of the propellant.

The relation between the vapour pressure and temperature shown in figure 6.2, offers a simple solution to mass flow rate control in the absence of a mass flow regulator. To get more insight, a second set of thrust measurements was performed to estimate the thrust and mass flow rate as a function of the reservoir temperature T_r with the results shown on table 6.1. In these experiments, the reservoir was loaded with 10 g of propellant and the thruster was then run at a fixed 20% duty cycle D (60 s period) for an elapsed time t_{el} of $\approx$ two to three hours in order to obtain reliable statistics. This was repeated for reservoir temperatures of 70 °C, 65 °C, 60 °C, 55 °C, and 50 °C. A representative sample of burns covering the duration of each run was examined and an average thrust (F_T) was obtained for each reservoir temperature. The average thrust was 0.6 mN at 70 °C dropping as the

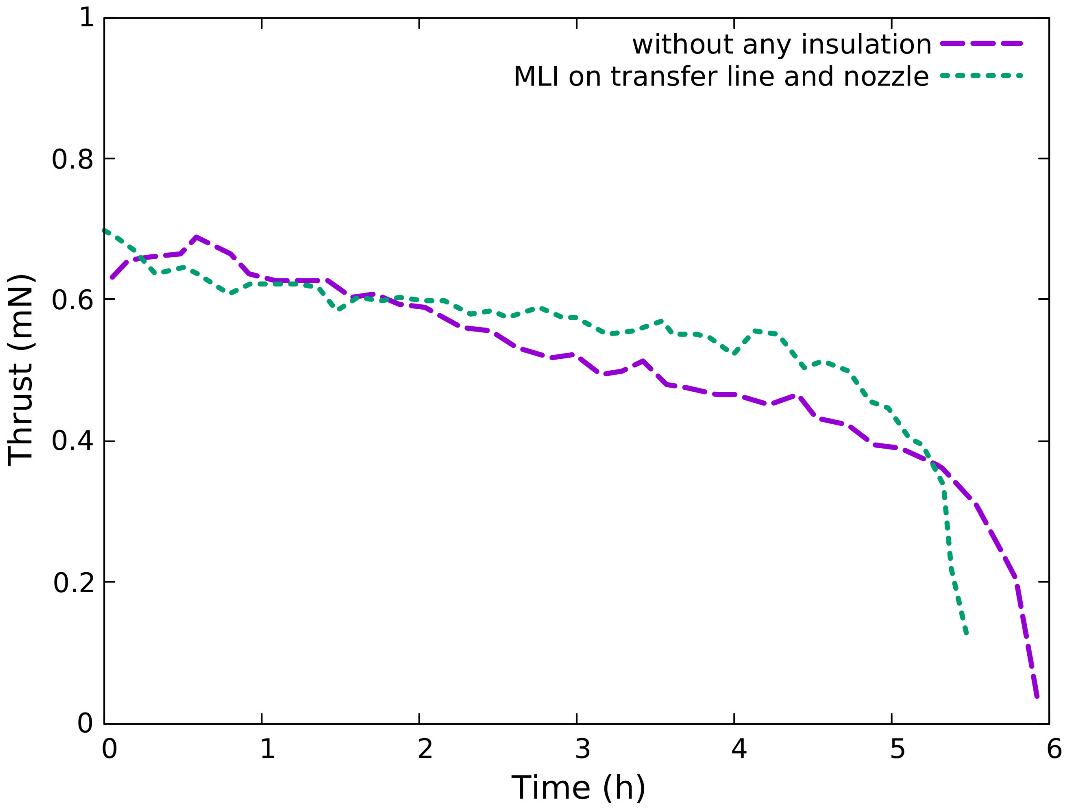

Figure 6.7: Measured thrust versus time. Thruster was configured for 12 s burns every minute, at 70 °C reservoir temperature. The reservoir was loaded with 10 g of naphthalene at the beginning of the run and was operated continuously until the propellant was fully exhausted. The purple dashed line was obtained with no insulation on the transfer line and nozzle and the green dotted line was obtained after insulating the transfer line and nozzle with multi-layer insulation (MLI), as discussed in section 6.3.7.

reservoir temperature is decreased to 0.11 mN at 50 °C. For each measurement, the mass difference Δm was obtained by weighing the thruster reservoir before and after the run, using a lab scale with a precision of 0.1 g. The average mass flow rate $\dot{m}$ for that operating period was then calculated according to the equation:

$$\dot{m} = \frac{\Delta m}{D\ t_{el}} \tag{6.5}$$

The specific impulse I_{sp} was then calculated by using the following equation:

$$I_{sp} = \frac{F_T}{g_0 \dot{m}} \tag{6.6}$$

where g_0 is the standard gravity ($9.81\,\mathrm{m\,s^{-2}}$). The measured thrust and calculated mass flow rate and specific impulse are summarised in table 6.1. They represent the typical performance to be expected during the useful life of the thruster, prior to the rapid deterioration that takes place as the propellant is about to run out. The calculated specific impulse I_{sp} at 60 °C to 70 °C appears to be constant at about 24.6 s, allowing some flexibility to the thruster designer to select a lower mass flow rate without compromising the propellant use efficiency of the system.

6.3.8 Alternative propellants to naphthalene

Alternative solid sublimating propellants to naphthalene can also be tested using the simple, two temperature zoned system presented in this chapter. One such alternative propellant is ferrocene ($Fe(C_5H_5)_2$), an organo-iron compound discovered in 1951 [135]. It consists of two cyclopentadienyl rings connected via a single iron atom. It has higher melting temperature than naphthalene (172.5 °C) [136] and the vapor pressure produced by sublimation is over 100 Torr at a temperature just below its melting point [137]. The high vapor pressure implies a high achievable thrust which is a requirement for fast orbital changes, for example to avoid a collision with space debris. The heat of sublimation is similar to that of naphthalene (about 70 kJ mol^{-1}). It exhibits remarkable stability and will not break down (decompose) at temperatures up to 400 °C [136], making it a suitable candidate for a resistojet thruster. Ferrocene-based compounds show promising signs of being chemically compatible with aluminium alloys [138] however a more detailed examination of its compatibility with material commonly used in space systems is necessary.

6.4 Summary

The study presented in this chapter has investigated the use of naphthalene as a propellant for a cold gas cubesat thruster proof of concept. The thruster concept is based on the sublimation of solid naphthalene which produces a reliable mass flow rate of gaseous naphthalene, used through a nozzle to produce thrust. Being stored in solid state, naphthalene does not have the disadvantages associated with the sloshing of liquid propellants or extremely high pressure associated with gas propellants. The proposed design utilises a two-zone heating system and a conventional solenoid ON/OFF valve to control flow. There was no malfunction observed due to naphthalene solidifying in any part of the gate valve or distribution system during the many tens of hours of operation of this system in the Wombat space simulation chamber. This supports the hypothesis that naphthalene is a propellant with limited engineering challenges to the thruster designer. It was shown that the naphthalene cold gas thruster can produce thrust around 0.6 mN at a specific impulse of 24.6 s and at a propellant temperature of 70 °C. This is achieved within the power limitations of a cubesat. The thrust measurements presented in this chapter indicate that a total impulse of at least 24 N s per 100 g (86.2 cm^3) of propellant can be achieved by a carefully designed, compact naphthalene cold gas thruster. To put this in perspective, 24 N s of total impulse could be used by a typical 2.66 kg 2U cubesat in a low earth orbit (LEO) at 400 km to raise its orbit via a Hohmann transfer to approximately 416 km. This manoeuvre can increase its life in space by approximately a year, depending on solar conditions and the drag coefficient of the cubesat. It can be also used to efficiently assist spacecraft deorbiting. Despite the lack of a pressure regulation valve to control the mass flow rate, the variability in the thrust produced was found to be low and would make this type of thruster a suitable system for station keeping of LEO satellites. Future work will aim to improve the performance by using an optimised nozzle for the operating conditions of this thruster, and improve the thermal control to confirm suitability and reliability of the system for testing in space.

The use of naphthalene as the propellant of a plasma thruster while possible, is likely to be impractical. The complex molecule of naphthalene is likely to break down into smaller compounds once the plasma is ignited. In an experiment to explore this, it was found that the plasma tube walls were covered by what is likely to be carbon, very shortly after plasma ignition. If this is to be pursued further, special care has to be taken in the selection of the operating parameters of the thruster, to ensure all propellant is exhausted from the thruster and there is no deposit which is likely to constrict the flow of gas over time.

Alternative sublimating propellants such as ferrocene can also be tested in the presented, two temperature zoned system.

Chapter 7

Conclusion

7.1 Summary of results

The central theme of this thesis has been the development and measurement of propulsion systems for a class of small satellites known as cubesats. While the general propulsion principles and techniques developed since the beginning of the satellite era apply to cubesats too, the limitations of size and available electrical power make the realisation of cubesat compatible thrusters rather difficult. The work in this thesis has approached this challenge in a multi-disciplinary fashion, combining knowledge from various physics disciplines including classical physics, plasma physics and thermodynamics, to many engineering fields including those of mechanical, electrical/electronic and materials engineering. It has contributed to three aspects of the cubesat thruster development. These are the direct measurement of the thruster performance in the laboratory, the evolution of the existing Pocket Rocket electrothermal RF plasma thruster and its associated RF power supply system, and the development of a simpler cold gas thruster using naphthalene as the propellant.

Verification of the thruster performance has always been an important aspect of the development of a thruster system. This thesis has presented an alternative thrust measurement system for a hanging pendulum thrust stand based on a low cost load cell. Its performance was directly compared to the more typical system of measuring the induced displacement of the pendulum by the thruster using a laser interferometer system. While the laser system still has the advantage of lower noise by roughly a factor of two, the load cell was found to exhibit less zero drift despite not having temperature compensation. It also has a considerably lower cost compared to the interferometer, making it a viable alternative, especially for thrust measurements in the range of hundreds of micro-newtons. Another advantage is that the load cell based stand sensitivity is not as dependent on the suspended mass (weight), unlike the displacement measuring system. Alternative load cells can be utilised to modify the measurement range, if that is required. The load cell system was found to suffer from seemingly random breakouts of noise, however this is not affecting the result of a repeated measurement.

The Pocket Rocket is an electrothermal RF plasma thruster developed by the SP3 laboratory. This thesis has described the development of the next generation of the Pocket Rocket called the Inductive Pocket Rocket (IPR). It is based on the previous implementation of the Pocket Rocket which was a capacitively coupled plasma system. The IPR has demonstrated thrust gain at plasma ignition, operating as an electrothermal plasma thruster. A small foot print impedance matching network operating at 40.68 MHz and mounted directly onto the plasma cavity allows reliable measurements of direct thrust with inductive PR immersed in vacuum and attached to an optimised thrust balance. The custom made magnetic damper facilitates the measurement procedure by limiting thermal effects during plasma burns which allows reliable and repeatable measurements. The direct thrust measurements of the inductive PR have confirmed the production of thrust and have highlighted a couple of areas of improvement which will be considered in future work. Based on the reported results, future studies are justified and are expected to incrementally improve the performance of the presented proof of concept. These could include the operation of the RF amplifier in pulse mode.

Complementing the work on the inductive Pocket Rocket, the thesis presented a novel 40.68 MHz RF source system suitable for driving the IPR. The design is based on a high efficiency class-E RF amplifier, and it was designed to match the powering requirements of the IPR. The efficiency achieved by this design exceeded 91 %. Maximising the efficiency results in little heat being generated by the electronics which can easily be accommodated by dumping it on the cubesat frame. This was shown to be true by operating the IPR - class-E amplifier combo in space conditions in the Wombat chamber. To further support the claim that the combo is a good match for cubesat propulsion, the combination of the RF source, power supply and IPR was placed in the Wombat space simulation chamber and a direct thrust measurement was made. The measurement was conducted using xenon and it showed an increase in the thrust by the operation of the system, as expected by prior, more detailed measurements using argon, presented in an earlier chapter.

Approaching the cubesat thruster from a different angle, this thesis presented a proof of concept cold gas thruster using naphthalene as a propellant. The thruster concept is based on the sublimation of solid naphthalene which produces a reliable mass flow rate of gaseous naphthalene, used through a nozzle to produce thrust. Being stored in solid state, naphthalene does not have the disadvantages associated with the sloshing of liquid propellants or extremely high pressure associated with gas propellants. The proposed design utilises a two-zone heating system and a conventional solenoid ON/OFF valve to control flow. There was no malfunction due to naphthalene solidifying in any part of the gate valve or distribution system during the many tens of hours of operation of this system in the Wombat space simulation chamber. This supports the hypothesis that naphthalene is a propellant with limited engineering challenges to the thruster designer. It was shown that the naphthalene cold gas thruster can produce thrust around 0.6 mN at a specific impulse of 24.6 s and at a propellant temperature of 70 °C. This is achieved within the power limitations of a cubesat. The thrust measurements presented in this chapter indicate that a total impulse of at least 24 N s per 100 g (86.2 cm^3) of propellant can be achieved by a carefully designed, compact naphthalene cold gas thruster. To put this in perspective, 24 N s of total impulse could be used by a typical 2.66 kg 2U cubesat in a low earth orbit (LEO) at 400 km to raise its orbit via a Hohmann transfer to approximately 416 km. This manoeuvre can increase its life in space by approximately a year, depending on solar conditions and the drag coefficient of the cubesat. It can be also used to efficiently assist spacecraft deorbiting. Despite the lack of a pressure regulation valve to control the mass flow rate, the variability in the thrust produced was found to be low and would make this type of thruster a suitable system for station keeping of LEO satellites.

7.2 Future Work

The work presented in this thesis has identified a number of potential future work topics. The following is a list of suggestions of future research that is a natural continuation of this work.

7.2.1 Loadcell on pendulum thrust balance

Given the encouraging results obtained from the low cost load cell on a pendulum thrust balance, further investigation and development of this method is justified in the future. A better quality, temperature compensated load cell could yield improved resolution and less drift related to the heating resulting from the operation of the thruster. A faster ADC could provide better temporal resolution which would enable the testing of fast pulsed thrusters. Better electrical shielding could allow measurements of high power RF or other electrical discharge based thrusters.

7.2.2 Evolution of the naphthalene thruster

The presented work showed that naphthalene can be used as the propellant for a cold gas thruster. Limited preliminary tests have been conducted that indicate it is possible to further heat up the naphthalene before it is expelled through the nozzle in order to improve the performance. This can be done with an electric heating element following the resistojet principle. Care must be given in the design of the resistojet to ensure the naphthalene molecule is not broken up; if that happens, the likely outcome is that carbon will build up on the surfaces that come in contact with it and this deposit may eventually clog the path of the propellant.

While naphthalene is a good fit for such a propulsion system, there may be more substances that may be even more attractive for that task. One such substance identified is ferrocene. Ferrocene also sublimates readily but can produce much higher vapour pressure compared to naphthalene, which can result in a higher thrust. This could be useful in cases where a fast manoeuvre needs to be performed, for example, to avoid a collision with space debris.

7.2.3 Commercialisation and space qualification of the naphthalene thruster

At the time of writing, the concept of the naphthalene cold gas propellant presented in chapter 6 of this thesis, is being developed further by Boswell Technologies[1]. This project, named Bogong after the native Australian moth (*Agrotis infusa*), aims to place a naphthalene thruster in orbit to evaluate the practical aspects of operating this concept thruster in space. An engineering drawing of the Bogong thruster can be seen in figure 7.1.

The thruster is planned to be a payload of opportunity on a Skykraft[2] satellite which

---

[1] `https://boswelltechnologies.com`

[2] `https://skykraft.com.au`

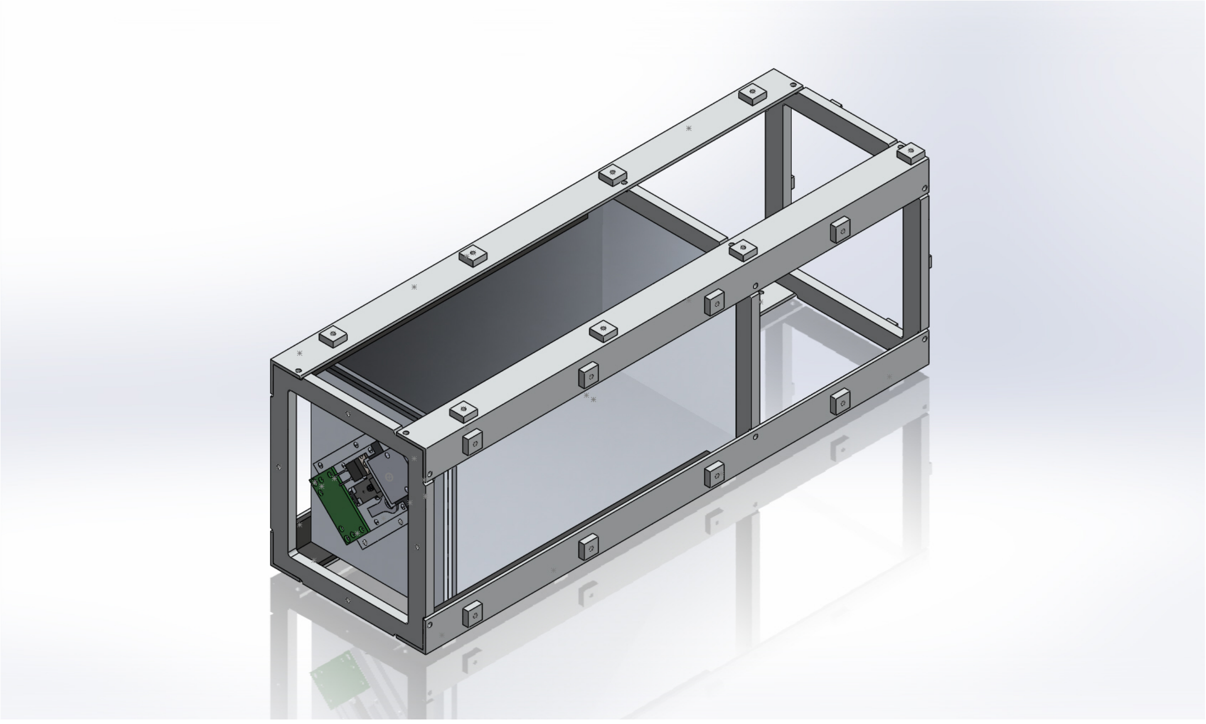

Figure 7.1: Engineering drawing of the *Bogong* naphthalene thruster. On the left side, the sliding ON/OFF valve can be seen. The propellant reservoir take most of the space in the middle of the frame. The empty space seen on the right of the drawing is reserved for the support electronics (not depicted). The frame is designed to fit on a Skykraft satellite. This image is courtesy of Mahdi Davoodianidalik (SP3 group, ANU) and Boswell Technologies.

is scheduled to be placed in orbit in June 2022. While in orbit, the thruster will be used to make small orbital changes which will be then be verified by the analysis of the changes over time in the keplerian elements of the host satellite. The thruster occupies approximately 3-U of space and the design is based on the two temperature zoned design, described in this thesis.

Appendix A

The Blue Wren cubesat ground station

A.1 Motivation

The ANU cubesat ground station (Blue Wren) was designed and built in 2016 in order to support the INSPIRE-2 cubesat [139], which was a part of QB50 mission [140] managed by the von Karman Institute in Belgium. It provided reliable service all the way through the QB50 mission until late 2018. It operates in the satellite segments of the amateur radio bands of 2 metres (144 MHz to 148 MHz) and 70 centimetres (430 MHz to 440 MHz). While INSPIRE-2 is using a UHF frequency for both uplink and downlink, the ground station is designed to be compatible with a wide range of cubesats that operate in either of the two bands, using any of the commonly used digital modulation schemes. Figure A.1 shows a diagram of the ground station hardware and the connections between the various components.

The ground station design and setup described in this appendix has been performed by the author but is only loosely related to the author's thesis work presented in the previous chapters. It is though firmly related to the overall contributions in the field of cubesat engineering which are of interest to the greater cubesat community.

The ground station has been regularly used to monitor newly launched cubesats and other satellites that operate in the supported frequency ranges.

A.2 Ground station hardware

The ground station is built around an Icom IC-9100 transceiver, designed for the Amateur Radio market. This transceiver covers a number of Amateur Radio bands in the MF,

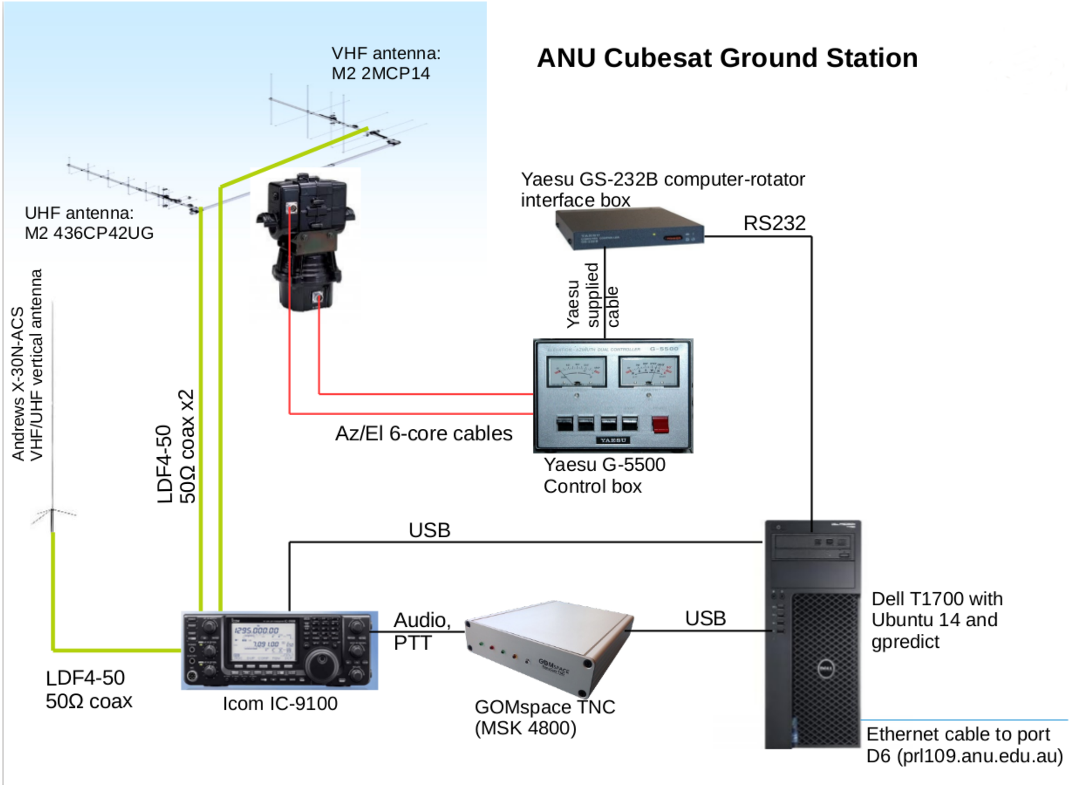

Figure A.1: Diagram of the ANU ground station hardware

HF, VHF and UHF parts of the spectrum, including the two bands of interest. It can be used for both analog communication (voice) and low speed (up to 9600 baud) digital communications. The power output of this radio is 75 W on VHF and 50 W on UHF which offers an acceptable margin for reliable cubesat communications according to the link budget shown earlier in this paper.

There are two dedicated directional antennas: an M2 model 2MCP14 VHF cross polarised yagi with a fixed right hand circular polarisation (RHCP) with a gain of 12.3 dBi, and an M2 model 436CP42UG cross polarised yagi operating in RHCP with a gain of 18.9 dBi. The UHF antenna has a -3 dB beamwidth of 21° which suggests that a pointing accuracy of approximately ±5° is acceptable. The use of circular polarisation by the ground station antennas is common practice when the satellite uses linear polarisation. In this case, the mismatch between circular and linear polarisation results in a constant 3 dB loss which is not dependent on the satellite-ground station geometry. An omnidirectional vertical antenna is also installed in the mast. It is used as a reference antenna and as a backup antenna in case of failure in the main antennas or the rotator. The antennas can be seen in Figure A.2.

Figure A.2: The ANU ground station antennas (mid left) shows in the local environment

The positioning of the antennas is a compromise between easy roof access, available infrastructure, and clear view of the sky. The two primary difficulties are the ANU 14UD heavy ion accelerator tower, seen in figure A.2 directly behind the antennas, and the Telstra communications tower on Black Mountain which is to the NNE of the ground station antennas and is a source of increased interference in the form of intermodulation distortion (IMD) when the antenna is pointing to it.

The antenna system is controlled both in azimuth and elevation via a Yaesu GS-5500 rotator system. All antennas are connected to the radio with Heliax® LDF4-50A half inch coaxial cable which is selected because of the low loss of approximately 1.5 dB on UHF for the 30 m run between the antennas and the transceiver. There is also a MiniKits EME237-70CM preamplifier with a low noise figure (1 dB) on the UHF band.

A GOMspace TNC is used for modulating and demodulating MSK signals to allow communications with INSPIRE-2.

A.3 Ground Station software

The ground station is based on a Linux PC and uses Gpredict for antenna pointing and doppler control of the radio. A modified version (by UNSW) of GOMspace's csp-term is

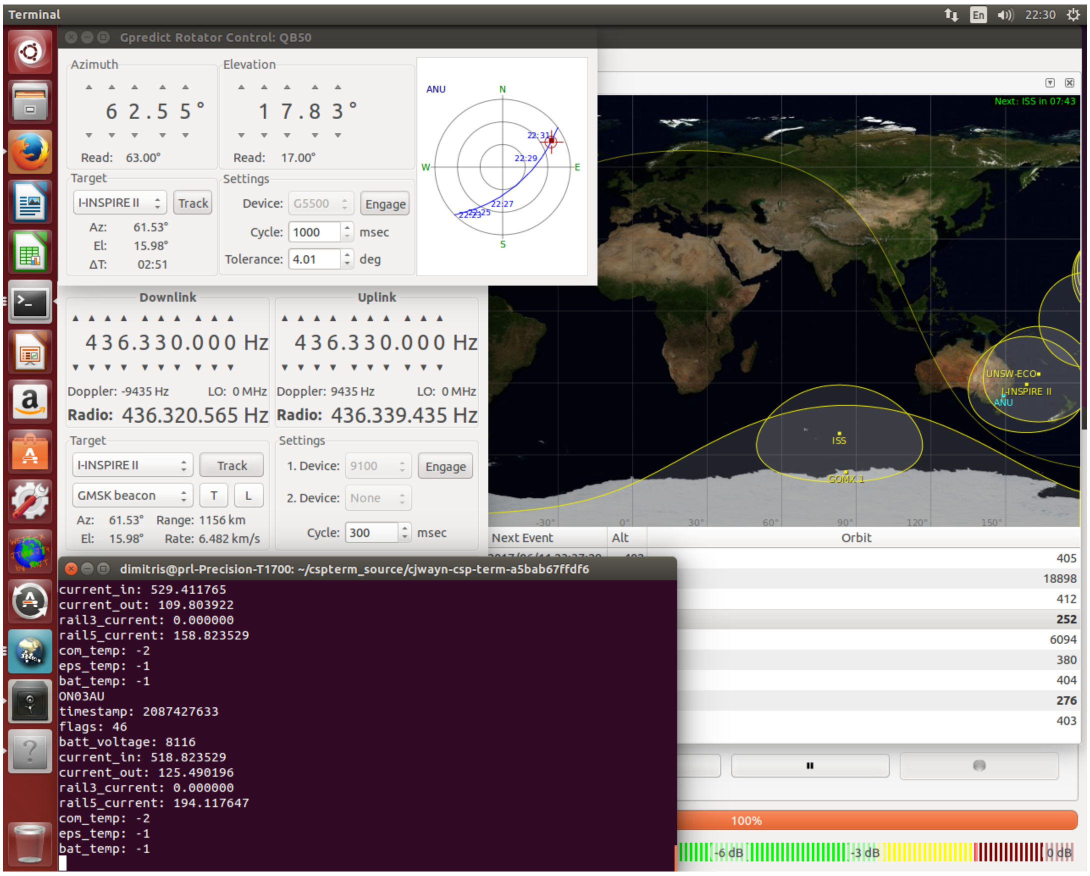

Azimuth: 62.55° Read: 63.00°

Elevation: 17.83° Read: 17.00°

Target: I-INSPIRE II Track
Az: 61.53°
El: 15.98°
ΔT: 02:51

Settings
Device: G5500 Engage
Cycle: 1000 msec
Tolerance: 4.01 deg

Downlink: 436.330.000 Hz
Doppler: -9435 Hz LO: 0 MHz
Radio: 436.320.565 Hz

Uplink: 436.330.000 Hz
Doppler: 9435 Hz LO: 0 MHz
Radio: 436.339.435 Hz

Target: I-INSPIRE II Track
GMSK beacon T L
Az: 61.53° Range: 1156 km
El: 15.98° Rate: 6.482 km/s

Settings
1. Device: 9100 Engage
2. Device: None
Cycle: 300 msec

dimitris@prl-Precision-T1700: ~/cspterm_source/cjwayn-csp-term-a5bab67ffdf6

```
current_in: 529.411765
current_out: 109.803922
rail3_current: 0.000000
rail5_current: 158.823529
com_temp: -2
eps_temp: -1
bat_temp: -1
ON03AU
timestamp: 2087427633
flags: 46
batt_voltage: 8116
current_in: 518.823529
current_out: 125.490196
rail3_current: 0.000000
rail5_current: 194.117647
com_temp: -2
eps_temp: -1
bat_temp: -1
```

Figure A.3: Screen shot of the ANU ground station showing Gpredict and csp-term

used to interface to the GOMspace TNC, as required for INSPIRE-2. For cubesats using different modulation schemes, the ground station uses UZ7HO's soundmodem software (`http://uz7.ho.ua/packetradio.htm`) which is capable of AFSK, GFSK and BPSK modulation and demodulation.

A.4 Operation

Prior to the launch of INSPIRE-2, the ground station was tested using some of the many satellites that carry amateur radio equipment, including the International Space Station APRS digipeater, FO-29, and the QB50 precursor satellites. Some very limited testing was performed with the satellite at the Advanced Instrumentation Technology Centre (AITC) situated on the ANU campus at the top of Mt. Stromlo.

To comply with the Australian regulations governing amateur radio described in the Radiocommunications Licence Conditions (Amateur Licence) Determination, the ground station was initially operated manually by a suitably qualified licence holder. The manual operation in the early stages of establishing communications with a satellite is crucial to allow the fine tuning of the many variables that determine the success of the system. It was found that reliable communication was not possible to achieve with INSPIRE-2 due to reasons discussed in detail in [139].

Blue Wren has provided communication support to other CubeSat missions, including QB50's UCLsat and Phoenix [141]. For the latter, it was configured to operate autonomously to collect the data scheduled for transmission from the satellite when passing over the ANU ground station. In this mode of operation, it has collected tens of megabytes of data in support of that mission.

Bibliography

[1] P. K. Rao, S. J. Holmes, R. K. Anderson, J. Winston, and P. E. Lehr. *Weather Satellites: Systems, Data, and Environmental Applications.* American Meteorological Society, 1990. ISBN 978-1-944970-16-1. doi: 10.1007/978-1-944970-16-1. 1

[2] Pratistha Kansakar and Faisal Hossain. A review of applications of satellite earth observation data for global societal benefit and stewardship of planet earth. *Space Policy*, 2016. ISSN 1879338X. doi: 10.1016/j.spacepol.2016.05.005. 1

[3] C P Lo. Applied remote sensing. *Geocarto International*, 1(4):60, 1986. doi: 10.1080/10106048609354071. URL `https://doi.org/10.1080/10106048609354071`. 1

[4] B. W. Parkinson, T. Stansell, R. Beard, and K. Gromov. A History of Satellite Navigation. *Navigation*, 1995. ISSN 21614296. doi: 10.1002/j.2161-4296.1995.tb02333.x. 1

[5] Norman Bonnor. A brief history of global navigation satellite systems, 2012. ISSN 03734633. 1

[6] R. R. Weber, J. K. Alexander, and R. G. Stone. The Radio Astronomy Explorer Satellite, a LowâĂŘFrequency Observatory. *Radio Science*, 1971. ISSN 1944799X. doi: 10.1029/RS006i012p01085. 1

[7] John K Davies. *Satellite astronomy : the principles and practice of astronomy from space.* Halsted Press, New York, 1988. 1

[8] J. V. Charyk. COMMUNICATIONS SATELLITES. *Journal of Spacecraft and Rockets*, 1977. ISSN 00224650. doi: 10.2514/3.57214. 1

[9] Christopher F. Hoeber and David J. Kim. Continued evolution of communication satellites. *Acta Astronautica*, 2000. ISSN 00945765. doi: 10.1016/S0094-5765(00)00046-1. 1

[10] Pravin C. Jain. Architectural Trends in Military Satellite Communications Systems. *Proceedings of the IEEE*, 1990. ISSN 15582256. doi: 10.1109/5.56931. 1

[11] Cubesat Design Specification Rev. 13, 2014. URL `http://www.cubesat.org/s/cds{_}rev13{_}final2.pdf`. 2, 6, 8, 34, 51

[12] L. J. Kamm. Magnetorquer-a Satellite Orientation Device. *ARS Journal*, 1961. doi: 10.2514/8.5645. 2

[13] S. Rajaram and P. S. Goel. MAGNETIC ATTITUDE CONTROL OF NEAR EARTH SPINNING SATELLITES. *J Br Interplanet Soc*, 1978. 2

[14] P. S. Goel and S. Rajaram. Magnetic attitude control of a momentum-biased satellite in near-equatorial orbit. *Journal of Guidance, Control, and Dynamics*, 1979. ISSN 07315090. doi: 10.2514/3.55884. 2

[15] Alison Olechowski, Steven D. Eppinger, and Nitin Joglekar. Technology readiness levels at 40: A study of state-of-the-art use, challenges, and opportunities. *Portland International Conference on Management of Engineering and Technology*, 2015-Septe:2084–2094, 2015. doi: 10.1109/PICMET.2015.7273196. 6

[16] Erik Kulu. Nanosat database, 2019. URL `https://www.nanosats.eu`. 6, 34, 35, 51

[17] Mengu Cho and Naomi Kurahara. International network operations of five CubeSats constellation [A]. *29th Annual AIAA/USU Conference on Small Satellites*, pages SSC16–XIII–8, 2016. 6

[18] Kiran Pradhan, Faure Pauline, George Maeda, Sangkyun Kim, Hirokazu Masui, and Mengu Cho. {BIRDS-2}: Multi-Nation {Cubesat} Constellation Project for Learning and Capacity Building. *Proc. 32nd Annual AIAA/USU Conf. on Small Satellites*, 2018. 6

[19] Faraaz Shamutally, Ziyaad Soreefan, Arjoon Suddhoo, and Jean Marc Mompié. Practical 'Low Cost' LEO Receiving Ground Station. *2018 IEEE Radio and Antenna Days of the Indian Ocean, RADIO 2018*, pages 2–3, 2018. doi: 10.23919/RADIO.2018.8572330. 6

[20] Sreeja Nag, Joseph L. Rios, David Gerhardt, and Camvu Pham. CubeSat constellation design for air traffic monitoring. *Acta Astronautica*, 128:180–193, 2016. ISSN 00945765. doi: 10.1016/j.actaastro.2016.07.010. 7

[21] Marco Gomez Jenkins, David Krejci, and Paulo Lozano. CubeSat constellation management using Ionic Liquid Electrospray Propulsion. *Acta Astronautica*, 151(June):243–252, oct 2018. ISSN 00945765. doi: 10.1016/j.actaastro.2018.06.007. URL `https://doi.org/10.1016/j.actaastro.2018.06.007https://linkinghub.elsevier.com/retrieve/pii/S0094576517312511`.

[22] Pardhasai Chadalavada and Atri Dutta. Regional CubeSat Constellation Design to Monitor Hurricanes. *IEEE Transactions on Geoscience and Remote Sensing*, pages 1–1, 2021. ISSN 0196-2892. doi: 10.1109/TGRS.2021.3124473. URL `https://ieeexplore.ieee.org/document/9600833/`.

[23] Shufan Wu, Wen Chen, Caixia Cao, Chuanxin Zhang, and Zhongcheng Mu. A multiple-CubeSat constellation for integrated earth observation and marine/air traffic monitoring. *Advances in Space Research*, 67(11): 3712–3724, jun 2021. ISSN 02731177. doi: 10.1016/j.asr.2020.04.025. URL `https://doi.org/10.1016/j.asr.2020.04.025https://linkinghub.elsevier.com/retrieve/pii/S0273117720302635`. 7, 9

[24] Robert K Masse, Christian B Carpenter, Derek T Schmuland, Jonathan Overly, and May Y Allen. *CubeSat High-impulse Adaptable Modular Propulsion System (CHAMPS) Product Line Development Status and Mission Applications.* American Institute of Aeronautics and Astronautics, Reston, Virginia, jul 2013. ISBN 978-1-62410-222-6. doi: 10.2514/6.2013-3760. URL `https://arc.aiaa.org/doi/abs/10.2514/6.2013-3760https://arc.aiaa.org/doi/10.2514/6.2013-3760`. 7

[25] Lawrence D Roberts. Addressing the Problem of Orbital Space Debris: Combining International Regulatory and Liability Regimes. *BC Int'l & Comp. L. Rev.*, 15:51, 1992. 7

[26] H. G. Lewis, J. Radtke, A. Rossi, J. Beck, M. Oswald, P. Anderson, B. Bastida Virgili, and H. Krag. Sensitivity of the space debris environment to large constellations and small satellites. *JBIS - Journal of the British Interplanetary Society*, 70(2-4):105–117, 2017. ISSN 0007084X. 7

[27] Jonas Radtke, Enrico Stoll, Hugh Lewis, and Benjamin Bastida Virgili. The Impact of the Increase in Small Satellite Launch Traffic on the Long-Term Evolution of the Space Debris Environment. *European Conference on Space Debris*, (April):18–21, 2017. 7

[28] V Schöneich, F Grabi, H Seiler, A Behnke, J.-P Baumann, M Ehresmann, J Franz, D Galla, B Gäßler, F Hessinger, R Hießl, M Koller, G Kuhn, N Müller, R Müller, A Papanikolaou, J Rieser, M Siedorf, V Starlinger, A Stier, A Tabelander, R Tietz, F Vardar, S Wizemann, A S Pagan, G Herdrich, and R Laufer. A Service and Deorbit Module for CubeSat Applications. *10th IAA Symposium on Small Satellites for Earth Observation*, (April), 2015. 7, 13

[29] Jeffery T. King, Jonathan Kolbeck, Jin S. Kang, Michael Sanders, and Michael Keidar. Performance analysis of nano-sat scale μCAT electric propulsion for 3U CubeSat attitude control. *Acta Astronautica*, 178(June 2020):722–732, jan 2021. ISSN 00945765. doi: 10.1016/j.actaastro.2020.10.006. URL `https://doi.org/10.1016/j.actaastro.2020.10.006https://linkinghub.elsevier.com/retrieve/pii/S0094576520306020`. 8, 13

[30] G. Robert Jahn. *Physics of Electric Propulsion*. McGraw-Hill, New York, 1968. ISBN 0-486-45040-6. 11, 12

[31] D.M. Goebel and I. Katz. *Fundamentals of Electric Propulsion: Ion and Hall Thrusters*. NASA, 2008. 11, 13, 51

[32] J. L. Cronin. Modern Dispenser Cathodes., 1981. ISSN 01437100. 12

[33] L. Habl, T. Lafleur, D. Rafalskyi, and P. Chabert. Plasma plume expansion with pulsed electron neutralization. *Plasma Sources Science and Technology*, 30(4), 2021. ISSN 13616595. doi: 10.1088/1361-6595/abf1d5. 12

[34] Michael Keidar, Taisen Zhuang, Alexey Shashurin, George Teel, Dereck Chiu, Joseph Lukas, Samudra Haque, and Lubos Brieda. Electric propulsion for small satellites. *Plasma Physics and Controlled Fusion*, 57:014005, 2015. ISSN 13616587. doi: 10.1088/0741-3335/57/1/014005. 13, 52

[35] David Krejci, Alexander Reissner, and Dennis Weihrauch. IFM Nano Thruster electric space propulsion: from first Cubesat demonstration to the first 100 thrusters

produced. *33nd Annual AIAA/USU Conference on Small Satellites*, pages 1–6, 2019. 14

[36] David Krejci, Lou Grimaud, Tony Schönherr, Valentin Hugonnaud, Alexander Reissner, and Bernhard Seifert. *ENPULSION NANO and MICRO propulsion systems: development and testing.* American Institute of Aeronautics and Astronautics, Reston, Virginia, aug 2021. ISBN 978-1-62410-611-8. doi: 10.2514/6.2021-3420. URL `https://arc.aiaa.org/doi/abs/10.2514/6.2021-3420https://arc.aiaa.org/doi/10.2514/6.2021-3420`. 14

[37] Alexander Kramer, Philip Bangert, and Klaus Schilling. UWE-4: First Electric Propulsion on a 1U CubeSatâĂŤIn-Orbit Experiments and Characterization. *Aerospace*, 2020. ISSN 2226-4310. doi: 10.3390/aerospace7070098. 14, 35

[38] Christine Charles and Rod Boswell. Current-free double-layer formation in a high-density helicon discharge. *Applied Physics Letters*, 82(9):1356–1358, 2003. ISSN 00036951. doi: 10.1063/1.1557319. 19

[39] C. Charles, R. W. Boswell, and A. Bish. Variable frequency matching to a radiofrequency source immersed in vacuum. *Journal of Physics D: Applied Physics*, 46(36): 365203, 2013. ISSN 00223727. doi: 10.1088/0022-3727/46/36/365203. 22, 38, 39, 54, 58, 63, 94

[40] Christine Charles, Roderick W Boswell, Andrew Bish, Vadim Khayms, and Edwin F Scholz. Direct Measurement of Axial Momentum Imparted by an Electrothermal Radiofrequency Plasma Micro-Thruster. *Frontiers in Physics*, 4:19, 2016. ISSN 2296-424X. doi: 10.3389/fphy.2016.00019. URL `https://www.frontiersin.org/article/10.3389/fphy.2016.00019`. 35, 38, 39, 53, 58, 59, 60, 94

[41] Dimitrios Tsifakis, Christine Charles, and Rod Boswell. An Inductively-Coupled Plasma Electrothermal Radiofrequency Thruster. *Frontiers in Physics*, 8, 2020. ISSN 2296424X. doi: 10.3389/fphy.2020.00034. 22, 39, 40, 45, 94

[42] H. Conrads and M. Schmidt. Plasma generation and plasma sources. *Plasma Sources Science and Technology*, 9(4):441–454, 2000. ISSN 09630252. doi: 10.1088/0963-0252/9/4/301. 22

[43] M. Chaker, M. Moisan, and Z. Zakrzewski. Microwave and RF surface wave sustained discharges as plasma sources for plasma chemistry and plasma processing. *Plasma Chemistry and Plasma Processing*, 6(1):79–96, 1986. ISSN 02724324. doi: 10.1007/BF00573823. 22

[44] Nathan O. Sokal and Alan D. Sokal. Class E-A New Class of High-Efficiency Tuned Single-Ended Switching Power Amplifiers. *IEEE Journal of Solid-State Circuits*, 1975. ISSN 1558173X. doi: 10.1109/JSSC.1975.1050582. 25, 62, 77

[45] W. Chen, R. A. Chinga, S. Yoshida, J. Lin, C. Chen, and W. Lo. A 25.6 W 13.56 MHz wireless power transfer system with a 94% efficiency GaN Class-E power amplifier. In *IEEE MTT-S International Microwave Symposium Digest*, 2012. ISBN 9781467310871. doi: 10.1109/MWSYM.2012.6258349. 25, 62

[46] Anita Gupta, Yogesh Arondekar, S. V.G. Ravindranath, H. Krishnaswamy, and B. N. Jagatap. A 13.56 MHz high power and high efficiency RF source. In *IEEE MTT-S International Microwave Symposium Digest*, 2013. ISBN 9781467361767. doi: 10.1109/MWSYM.2013.6697329.

[47] Marc Franco and Allen Katz. Class-E silicon carbide VHF power amplifier. In *IEEE MTT-S International Microwave Symposium Digest*, 2007. ISBN 1424406889. doi: 10.1109/MWSYM.2007.380207.

[48] Wei Liang, Christine Charles, Luke Raymond, Alex Stuchbery, Kawin Surakitbovorn, Lei Gu, Rod Boswell, and Juan Rivas-Davila. An Integrated RF Power Delivery and Plasma Micro-Thruster System for Nano-Satellites. *Frontiers in Physics*, 6:115, 2018. doi: 10.3389/fphy.2018.00115. 25

[49] Fe Terman. Radio engineer's handbook, 1943. ISSN 0040-5175. 26

[50] F. Caspers. RF engineering basic concepts: the Smith chart. *CAS 2010 - CERN Accelerator School: RF for Accelerators, Proceedings*, (May):95–116, 2011. 29

[51] M. S. Ivanov, G. N. Markelov, A. D. Ketsdever, and D. C. Wadsworth. Numerical study of cold gas micronozzle flows. In *37th Aerospace Sciences Meeting and Exhibit*, Reston, Virginia, jan 1999. American Institute of Aeronautics and Astronautics. doi: 10.2514/6.1999-166. 33

[52] Teck Seng Ho, Christine Charles, and Roderick W. Boswell. A Comprehensive Cold Gas Performance Study of the Pocket Rocket Radiofrequency Electrothermal Microthruster. *Frontiers in Physics*, 2017. ISSN 2296-424X. doi: 10.3389/fphy.2016.00055. 33, 38, 40, 45, 55, 57, 66, 88, 96

[53] F. Taccogna, R. Schneider, S. Longo, and M. Capitelli. Kinetic simulations of a plasma thruster. *Plasma Sources Science and Technology*, 17(2), 2008. ISSN 09630252. doi: 10.1088/0963-0252/17/2/024003. 33

[54] Teck Seng Ho, Christine Charles, and Rod Boswell. Performance modelling of plasma microthruster nozzles in vacuum. *Journal of Applied Physics*, 2018. ISSN 10897550. doi: 10.1063/1.5012765. 33, 53, 57, 69

[55] Grant Bonin, Niels Roth, Scott Armitage, Josh Newman, Ben Risi, and Robert E. Zee. CanX-4 and CanX-5 Precision Formation Flight: Mission Accomplished! In *Proceedings of the 29th Annual AIAA/USU Conference on Small Satellites*, Logan, Utah, 2015. doi: 10.1039/c3tc30232f. 35

[56] Andrea R. Wong, Alexandra Toftul, Kurt A. Polzin, and J. Boise Pearson. Non-contact thrust stand calibration method for repetitively pulsed electric thrusters. *Review of Scientific Instruments*, 2012. ISSN 00346748. doi: 10.1063/1.3680557. 35

[57] T. W. Haag. Thrust stand for high-power electric propulsion devices. *Review of Scientific Instruments*, 1991. ISSN 00346748. doi: 10.1063/1.1141998. 35

[58] Ugur Kokal and Murat Celik. Development of a mili-Newton level thrust stand for thrust measurements of electric propulsion systems. In *Proceedings of 8th International Conference on Recent Advances in Space Technologies, RAST 2017*, 2017. ISBN 9781538616031. doi: 10.1109/RAST.2017.8002970.

[59] J. Asakawa, K. Nishii, Y. Nakagawa, H. Koizumi, and K. Komurasaki. Direct measurement of 1-mN-class thrust and 100-s-class specific impulse for a CubeSat propulsion system. *Review of Scientific Instruments*, 2020. ISSN 10897623. doi: 10.1063/1.5121411. 35

[60] John K Ziemer. Performance Measurements Using a Sub-Micronewton Resolution Thrust Stand. *27th International Electric Propulsion Con- ference*, 2001. 35

[61] Wei Jing Zhou, Yan Ji Hong, and Hao Chang. A microNewton thrust stand for average thrust measurement of pulsed microthruster. In *Review of Scientific Instruments*, 2013. doi: 10.1063/1.4850637.

[62] J. Soni and S. Roy. Design and characterization of a nano-Newton resolution thrust stand. *Review of Scientific Instruments*, 2013. ISSN 00346748. doi: 10.1063/1.4819252.

[63] Bryan Little and Manish Jugroot. Development of a microthrust balance and ion beam measurement system: Characterizing a dual-mode thruster for spacecraft. *Vacuum*, 2019. ISSN 0042207X. doi: 10.1016/j.vacuum.2019.01.031.

[64] Haibin Tang, Chenbo Shi, Xin'ai Zhang, Zun Zhang, and Jiao Cheng. Pulsed thrust measurements using electromagnetic calibration techniques. *Review of Scientific Instruments*, 82(3):035118, mar 2011. ISSN 0034-6748. doi: 10.1063/1.3567803. URL `http://aip.scitation.org/doi/10.1063/1.3567803`.

[65] Zhe Zhang, Junxue Ren, Haibin Tang, William Yeong Liang Ling, and Thomas M. York. An ablative pulsed plasma thruster with a segmented anode. *Plasma Sources Science and Technology*, 27(1):015004, dec 2017. ISSN 1361-6595. doi: 10.1088/1361-6595/aa9e6b. URL `https://iopscience.iop.org/article/10.1088/1361-6595/aa9e6b`. 35

[66] James E. Polk, Anthony Pancotti, Thomas Haag, Scott King, Mitchell Walker, Joseph Blakely, and John Ziemer. Recommended practice for thrust measurement in electric propulsion testing. *Journal of Propulsion and Power*, 2017. ISSN 15333876. doi: 10.2514/1.B35564. 36

[67] Trevor Moeller and Kurt A. Polzin. Thrust stand for vertically oriented electric propulsion performance evaluation. *Review of Scientific Instruments*, 2010. ISSN 00346748. doi: 10.1063/1.3502463. 35

[68] Kurt A. Polzin, Thomas E. Markusic, Boris J. Stanojev, Amado Dehoyos, and Benjamin Spaun. Thrust stand for electric propulsion performance evaluation. *Review of Scientific Instruments*, 77(10):1–10, 2006. ISSN 00346748. doi: 10.1063/1.2357315. 35

[69] S. Rocca, C. Menon, and D. Nicolini. FEEP micro-thrust balance characterization and testing. *Measurement Science and Technology*, 17(4):711–718, 2006. ISSN 13616501. doi: 10.1088/0957-0233/17/4/016. 36

[70] Donald G. Chavers and Franklin R. Chang-Díaz. Momentum flux measuring instrument for neutral and charged particle flows. *Review of Scientific Instruments*, 2002. ISSN 00346748. doi: 10.1063/1.1505107. 37

[71] Michael D. West, Christine Charles, and Rod W. Boswell. A high sensitivity momentum flux measuring instrument for plasma thruster exhausts and diffusive plasmas. *Review of Scientific Instruments*, 2009. ISSN 00346748. doi: 10.1063/1.3142477.

[72] Kazunori Takahashi, Atsushi Komuro, and Akira Ando. Measurement of plasma momentum exerted on target by a small helicon plasma thruster and comparison with direct thrust measurement. *Review of Scientific Instruments*, 2015. ISSN 10897623. doi: 10.1063/1.4907797. 37

[73] L. Conde, M. D. Lahoz, J. Grabulosa, R. Hernández, J. González, M. Delgado, and J. Damba. Thrust stand based on a single point load cell for impulse measurements from plasma thrusters. *Review of Scientific Instruments*, 2020. ISSN 10897623. doi: 10.1063/1.5127189. 37

[74] Burak Karadag, Shinatora Cho, and Ikkoh Funaki. Note: Precision balance for sub-miliNewton resolution direct thrust measurement. *Review of Scientific Instruments*, 2018. ISSN 10897623. doi: 10.1063/1.5045855. 37

[75] T. Frieler and R. Groll. A torsional sub-milli-Newton thrust balance based on a spring leaf strain gauge sensor. *Review of Scientific Instruments*, 2018. ISSN 10897623. doi: 10.1063/1.4996419. 38

[76] R. John Stephen, K. Rajanna, Vivek Dhar, K. G.Kalyan Kumar, and S. Nagabushanam. Strain gauge based thrust measurement system for a stationary plasma thruster. *Measurement Science and Technology*, 2001. ISSN 09570233. doi: 10.1088/0957-0233/12/9/324. 38

[77] Sabrina Pottinger, Vaios Lappas, Christine Charles, and Rod Boswell. Performance characterization of a helicon double layer thruster using direct thrust measurements. *Journal of Physics D: Applied Physics*, 2011. ISSN 00223727. doi: 10.1088/0022-3727/44/23/235201. 39

[78] K. Takahashi, T. Lafleur, C. Charles, P. Alexander, R. W. Boswell, M. Perren, R. Laine, S. Pottinger, V. Lappas, T. Harle, and D. Lamprou. Direct thrust measurement of a permanent magnet helicon double layer thruster. *Applied Physics Letters*, 2011. ISSN 00036951. doi: 10.1063/1.3577608. 39, 69

[79] C. Charles and R. W. Boswell. Measurement and modelling of a radiofrequency micro-thruster. *Plasma Sources Science and Technology*, 21:022002, 2012. ISSN 09630252. doi: 10.1088/0963-0252/21/2/022002. 52, 63, 69

[80] NASA. State of the Art of Small Spacecraft Technology. *State of the Art of Small Spacecraft Technology*, 2018. URL `https://sst-soa.arc.nasa.gov/`. 52

[81] Jose C. Pascoa, Odelma Teixeira, and Gustavo Filipe. A review of propulsion systems for cubesats. In *ASME International Mechanical Engineering Congress and Exposition, Proceedings (IMECE)*, Pittsburgh, 2018. ISBN 9780791852002. doi: 10.1115/IMECE2018-88174.

[82] Kristina Lemmer. Propulsion for CubeSats. *Acta Astronautica*, 2017. ISSN 00945765. doi: 10.1016/j.actaastro.2017.01.048.

[83] J. Mueller, R. Hofer, and J. Ziemer. Survey of Propulsion Technologies Applicable to Cubesats. In *57th JANNAF Propulsion Meeting*, Pasadena, CA, 2010. ISBN 1424405254. doi: 10.2514/3.21030.

[84] Akshay Reddy Tummala and Atri Dutta. An Overview of Cube-Satellite Propulsion Technologies and Trends. *Aerospace*, 4(4), 2017. ISSN 2226-4310. doi: 10.3390/aerospace4040058. URL `http://www.mdpi.com/2226-4310/4/4/58`.

[85] Mirko Leomanni, Andrea Garulli, Antonio Giannitrapani, and Fabrizio Scortecci. Propulsion options for very low Earth orbit microsatellites. *Acta Astronautica*, 133:444–454, 2017. ISSN 00945765. doi: 10.1016/j.actaastro.2016.11.001.

[86] C Scharlemann, M Tajmar, N Buldrini, D Krejci, and B Seifert. Propulsion for Nanosatellites. In *32nd International Electric Propulsion Conference*, 2011. 52

[87] Christine Charles, Teck Seng Ho, Ashley Ellis, Thomas Charoy, Alex Bennet, Alex Stuchbery, Rod Boswell, Wei Liang, Luke Raymond, and Juan Rivas-Davila. The pocket rocket electro-thermal plasma thruster for 'CubeSat' nano-satellites. In *Proceedings of the International Astronautical Congress, IAC*, 2017. ISBN 9781510855373. 52

[88] C. Charles. Plasmas for spacecraft propulsion. *Journal of Physics D: Applied Physics*, 42:163001, 2009. ISSN 00223727. doi: 10.1088/0022-3727/42/16/163001. 52

[89] Amelia Greig, Christine Charles, and Rod Boswell. Plume characteristics of an electrothermal plasma microthruster. *IEEE Transactions on Plasma Science*, 42 (10):2728–2729, 2014. ISSN 00933813. doi: 10.1109/TPS.2014.2321176. 53

[90] A. Greig, C. Charles, N. Paulin, and R. W. Boswell. Volume and surface propellant heating in an electrothermal radio-frequency plasma micro-thruster. *Applied Physics Letters*, 2014. ISSN 00036951. doi: 10.1063/1.4892656. 53, 55, 67

[91] Amelia D. Greig, Christine Charles, and Rod Boswell. Simulations of Electron Heating in a Capacitively Coupled Radio Frequency Micro-Thruster using Computational Fluid Dynamics. In *44th AIAA Plasmadynamics and Lasers Conference*, 2013. doi: 10.2514/6.2013-2626. 53

[92] A. Greig, C. Charles, R. Hawkins, and R. Boswell. Direct measurement of neutral gas heating in a radio-frequency electrothermal plasma micro-thruster. *Applied Physics Letters*, 2013. ISSN 00036951. doi: 10.1063/1.4818657.

[93] Amelia Greig, Christine Charles, and Roderick W. Boswell. Simulation of main plasma parameters of a cylindrical asymmetric capacitively coupled plasma micro-thruster using computational fluid dynamics. *Frontiers in Physics*, 2(January):1–9, 2015. ISSN 2296-424X. doi: 10.3389/fphy.2014.00080. 53

[94] Michael A. Lieberman and Allan J. Lichtenberg. *Principles of Plasma Discharges and Materials Processing: Second Edition.* Wiley, Hoboken, NJ, second edition, 2005. ISBN 0471720011. doi: 10.1002/0471724254. 54, 55, 69

[95] Howard D. Curtis. *Orbital Mechanics for Engineering Students.* Elsevier, 2014. ISBN 9780080977478. doi: 10.1016/C2011-0-69685-1. URL `https://linkinghub.elsevier.com/retrieve/pii/C20110696851`. 54

[96] Teck Seng Ho, Christine Charles, and Rod Boswell. Neutral gas heating and ion transport in a constricted plasma flow. *Physics of Plasmas*, 24:084501, 2017. ISSN 10897674. doi: 10.1063/1.4996014. 54, 57, 69

[97] Scott J. Doyle. *Electron, ion and neutral heating in hollow cathode plasma thrusters.* PhD thesis, University of York, 2019. 54

[98] Teck Seng Ho, Christine Charles, and Rod Boswell. Redefinition of the self-bias voltage in a dielectrically shielded thin sheath RF discharge. *Journal of Applied Physics*, 2018. ISSN 10897550. doi: 10.1063/1.5023076. 54

[99] M. A. Lieberman, C. Charles, and R. W. Boswell. A theory for formation of a low pressure, current-free double layer. *Journal of Physics D: Applied Physics*, 2006. ISSN 00223727. doi: 10.1088/0022-3727/39/15/011. 55, 69

[100] T. Lafleur, K. Takahashi, C. Charles, and R. W. Boswell. Direct thrust measurements and modelling of a radio-frequency expanding plasma thruster. *Physics of Plasmas*, 2011. ISSN 1070664X. doi: 10.1063/1.3610570. 55, 69, 70

[101] Kazunori Takahashi. Helicon-type radiofrequency plasma thrusters and magnetic plasma nozzles. *Reviews of Modern Plasma Physics*, 2019. doi: 10.1007/s41614-019-0024-2. 55

[102] Amnon Fruchtman. Neutral depletion in a collisionless plasma. In *IEEE Transactions on Plasma Science*, 2008. doi: 10.1109/TPS.2008.918777. 55, 69, 70

[103] A. Fruchtman. Neutral gas depletion in low temperature plasma, 2017. ISSN 13616463. 55

[104] C. Charles and R. W. Boswell. Time development of a current-free double-layer. *Physics of Plasmas*, 2004. ISSN 1070664X. doi: 10.1063/1.1764829. 56

[105] Teck Seng Ho. *Supersonic Constricted Plasma Flows.* PhD thesis, Research School of Physics and Engineering, The Australian National University, 2018. 57, 65

[106] Wei Liang, Luke Raymond, Max Praglin, David Biggs, Fabio Righetti, Mark Cappelli, Brian Holman, and Juan Rivas Davila. Low-Mass RF Power Inverter for CubeSat Applications Using 3-D Printed Inductors. *IEEE Journal of Emerging and Selected Topics in Power Electronics*, PP:1, 2016. doi: 10.1109/JESTPE.2016.2644644. 62, 65

[107] Wei Liang, Luke Raymond, Max Praglin, David Biggs, Fabio Righetti, Mark Cappelli, Brian Holman, and Juan Rivas Davila. Low-mass RF power inverter for cubesat applications using 3-D printed inductors. *IEEE Journal of Emerging and Selected Topics in Power Electronics*, 2017. ISSN 21686785. doi: 10.1109/JESTPE.2016.2644644. 63

[108] Amelia D. Greig. *Pocket rocket : an electrothermal plasma micro-thruster.* PhD thesis, ANU, 2015. 69

[109] Lei Gu, Zikang Tong, Wei Liang, and Juan Rivas-Davila. A Multiresonant Gate Driver for High-Frequency Resonant Converters. *IEEE Transactions on Industrial Electronics*, 67(2):1405–1414, 2020. ISSN 15579948. doi: 10.1109/TIE.2019.2899557. 77

[110] C. Charles, R. W. Boswell, A. Bouchoule, C. Laure, and P. Ranson. Plasma diffusion from a low pressure radio frequency source. *Journal of Vacuum Science & Technology A: Vacuum, Surfaces, and Films*, 9(3):661–663, may 1991. ISSN 0734-2101. doi: 10.1116/1.577385. URL `http://avs.scitation.org/doi/10.1116/1.577385`. 82

[111] C. Charles, R. W. Boswell, and R. K. Porteous. Measurement and modeling of ion energy distribution functions in a low pressure argon plasma diffusing from a 13.56 MHz helicon source. *Journal of Vacuum Science & Technology A: Vacuum, Surfaces, and Films*, 10(2):398–403, mar 1992. ISSN 0734-2101. doi: 10.1116/1.578063. URL `http://avs.scitation.org/doi/10.1116/1.578063`. 82

[112] P. R.C. Neumann, M. M.M. Bilek, R. N. Tarrant, and D. R. McKenzie. A pulsed cathodic arc spacecraft propulsion system. *Plasma Sources Science and Technology*, 18(4), 2009. ISSN 09630252. doi: 10.1088/0963-0252/18/4/045005. 86

[113] Igal Kronhaus, Klaus Schilling, Mathias Pietzka, and Jochen Schein. Simple Orbit and Attitude Control Using Vacuum Arc Thrusters for Picosatellites. *Journal*

of Spacecraft and Rockets, 51(6):2008–2015, 2014. doi: 10.2514/1.A32796. URL `https://doi.org/10.2514/1.A32796`. 86

[114] P R C Neumannn, M M M Bilek, and D R McKenzie. Fuel Selection for Pulsed Cathodic Arc Thrusters. *Journal of Propulsion and Power*, 28(1):218–221, 2012. doi: 10.2514/1.B34336. URL `https://doi.org/10.2514/1.B34336`. 86

[115] Kateryna Aheieva, Kazuhiro Toyoda, and Mengu Cho. Vacuum Arc Thruster Development and Testing for Micro and Nano Satellites. *Transactions of the Japan Society for Aeronautical and Space Sciences, Aerospace Technology Japan*, 14(ists30): Pb_91–Pb_97, 2016. ISSN 1884-0485. doi: 10.2322/tastj.14.pb_91. 86

[116] Jonathan Kolbeck, André Anders, Isak I. Beilis, and Michael Keidar. Micropropulsion based on vacuum arcs. *Journal of Applied Physics*, 125(22), 2019. ISSN 10897550. doi: 10.1063/1.5081096. 86

[117] Rainer Dressler, Yu-Hui Chiu, and Dale Levandier. Propellant alternatives for ion and Hall effect thrusters. In *38th Aerospace Sciences Meeting and Exhibit*, page 602, Reston, Virigina, jan 2000. American Institute of Aeronautics and Astronautics. doi: 10.2514/6.2000-602. URL `https://arc.aiaa.org/doi/10.2514/6.2000-602`. 86

[118] Javier Martínez Martínez, Dmytro Rafalskyi, Elena Zorzoli Rossi, and Ane Aanesland. Development, qualification and first flight data of the iodine based cold gas thruster for cubesats. In *5th IAA Conference on University Satellite Missions and Cubesat Workshop*, Rome, Italy, 2020. ISBN 9780877036715. 86

[119] Dmytro Rafalskyi, Javier Martínez Martínez, Lui Habl, Elena Zorzoli Rossi, Plamen Proynov, Antoine Boré, Thomas Baret, Antoine Poyet, Trevor Lafleur, Stanislav Dudin, and Ane Aanesland. In-orbit demonstration of an iodine electric propulsion system. *Nature*, 599(7885):411–415, nov 2021. ISSN 0028-0836. doi: 10.1038/s41586-021-04015-y. URL `https://www.nature.com/articles/s41586-021-04015-y`. 86

[120] Gregory Paul Baxter, Charles Hendee Hickey, and Walter Chapin Holmes. THE VAPOR PRESSURE OF IODINE. *Journal of the American Chemical Society*, 29

(2):127–136, 1907. doi: 10.1021/ja01956a004. URL `https://doi.org/10.1021/ja01956a004`. 86

[121] Gregory Paul Baxter and Merritt Roy Grose. THE VAPOR PRESSURE OF IODINE BETWEEN 50Âř AND 95Âř. *Journal of the American Chemical Society*, 37 (5):1061–1072, 1915. doi: 10.1021/ja02170a007. URL `https://doi.org/10.1021/ja02170a007`.

[122] Louis J Gillespie and Lewis H D Fraser. The Normal Vapor Pressure of Crystalline Iodine. *Journal of the American Chemical Society*, 58(11):2260–2263, 1936. doi: 10.1021/ja01302a050. URL `https://doi.org/10.1021/ja01302a050`. 86

[123] J. Martínez Martínez and D. Rafalskyi. Design and development of iodine flow control systems for miniaturized propulsion systems. *CEAS Space Journal*, (0123456789), 2021. ISSN 18682510. doi: 10.1007/s12567-021-00384-2. URL `https://doi.org/10.1007/s12567-021-00384-2`. 86, 87

[124] D. Ambrose, I. J. Lawrenson, and C. H.S. Sprake. The vapour pressure of naphthalene. *The Journal of Chemical Thermodynamics*, 1975. ISSN 10963626. doi: 10.1016/0021-9614(75)90038-5. 88

[125] Lewis Fowler, Walter N. Trump, and Carl E. Vogler. Vapor Pressure of Naphthalene: New Measurements between 40Âř and 180Âř C. *Journal of Chemical and Engineering Data*, 1968. ISSN 15205134. doi: 10.1021/je60037a020. 88

[126] Christian Vargel. *Corrosion of Aluminium*. 2004. ISBN 9780080444956. doi: 10.1016/B978-0-08-044495-6.X5000-9. 88

[127] Robert H. Olds. Attitude control and station keeping of a communication satellite in a 24-hour orbit. *AIAA Journal*, 1(4):852–858, 1963. ISSN 00011452. doi: 10.2514/3.1653. 89

[128] Lance K. Yoneshige. *Methodology to measure impulses in the micro-newton range for a novel micro-thruster concept.* PhD thesis, University of Hawaii, Manoa, 2007. URL `http://hdl.handle.net/10125/20683{%}0A`. 89

[129] Toshihiro Chujo, Osamu Mori, and Yuki Kubo. Development of solid-gas equilibrium propulsion system for small spacecraft. *Acta Astronautica*, 2017. ISSN 00945765. doi: 10.1016/j.actaastro.2017.07.050. 89

[130] Irving Langmuir. The constitution and fundamental properties of solids and liquids. Part I. Solids. *Journal of the American Chemical Society*, 1916. ISSN 15205126. doi: 10.1021/ja02268a002. 89

[131] Susumu Miyamoto. A theory of the rate of sublimation. *Transactions of the Faraday Society*, 1933. ISSN 00147672. doi: 10.1039/tf9332900794. 89, 90

[132] Kurt A Polzin, Joao F Seixal, Stephanie L Mauro, Adam O Burt, Armando Martinez, and Adam K Martin. The iodine Satellite (iSat) Propellant Feed System - Design and Development. In *35th International Electric Propulsion Conference (IEPC); October 08, 2017 - October 12, 2017; Atlanta, GA; United States*, Atlanta - Georgia, 2017. URL `https://ntrs.nasa.gov/archive/nasa/casi.ntrs.nasa.gov/20170012401.pdf`. 90

[133] James S. Chickosa and William E. Acree. Enthalpies of sublimation of organic and organometallic compounds. 1910-2001. *Journal of Physical and Chemical Reference Data*, 2002. ISSN 00472689. doi: 10.1063/1.1475333. 90

[134] M. Orain, P. Baranger, B. Rossow, and F. Grisch. Fluorescence spectroscopy of naphthalene at high temperatures and pressures: Implications for fuel-concentration measurements. *Applied Physics B: Lasers and Optics*, 2011. ISSN 09462171. doi: 10.1007/s00340-010-4353-7. 91

[135] T. J. KEALY and P. L. PAUSON. A New Type of Organo-Iron Compound. *Nature*, 168(4285):1039–1040, dec 1951. ISSN 0028-0836. doi: 10.1038/1681039b0. URL `http://www.nature.com/articles/1681039b0`. 100

[136] Didier Astruc. Why is Ferrocene so Exceptional? *European Journal of Inorganic Chemistry*, 2017(1):6–29, 2017. ISSN 10990682. doi: 10.1002/ejic.201600983. 100

[137] Michal Fulem, Květoslav RÅŕžička, Ctirad Červinka, Marisa A.A. Rocha, Luís M.N.B.F. Santos, and Robert F. Berg. Recommended vapor pressure and thermophysical data for ferrocene. *Journal of Chemical Thermodynamics*, 57:530–540, 2013. ISSN 00219614. doi: 10.1016/j.jct.2012.07.023. 100

[138] Uzma Nazir, Zareen Akhter, Naveed Kausar Janjua, Muhammad Adeel Asghar, Sehrish Kanwal, Tehmeena Maryum Butt, Asma Sani, Faroha Liaqat, Rizwan Hussain, and Faiz Ullah Shah. Biferrocenyl Schiff bases as efficient corrosion inhibitors for an aluminium alloy in HCl solution: A combined experimental and theoretical study. *RSC Advances*, 10(13):7585–7599, 2020. ISSN 20462069. doi: 10.1039/c9ra10692h. 100

[139] Iver H. Cairns, Christine Charles, Andrew G. Dempster, Jiro Funamoto, Joon Wayn Cheong, Wayne Peacock, John Lam, Barnaby Osborne, Will Andrew, Tom Croston, Ben Southwell, R. W. Boswell, A. G. Monger, Christopher H. Betters, Sergio G. Leon-Saval, Joss Bland-Hawthorn, J. Khachan, X. Wu, S. Manidis, D. Tsifakis, and R. Maj. The INSPIRE-2 CubeSat for the QB50 Project, 2020. ISSN 15729672. 109, 113

[140] Robert Twiggs, Benjamin Malphrus, and Jean Muylaert. SSC10-XII-3 The QB50 Program , the first CubeSat Constellations doing Science. *24th AIAA/USU Conference on Small Satellites*, 12, 2010. URL `http://digitalcommons.usu.edu/smallsat/2010/all2010/72/{%}5Cnhttp://digitalcommons.usu.edu/cgi/viewcontent.cgi?article=1255{&}context=smallsat`. 109

[141] Ming-xian Huang, Ming-yang Hong, and Jyh-ching Juang. Analysis of Tumbling Motions by Combining Telemetry Data and Radio Signal. *Proceedings of the Small Satellite Conference*, (SSC18-WKX-01), 2018. URL `https://digitalcommons.usu.edu/cgi/viewcontent.cgi?article=4290{&}context=smallsat`. 113